AN ABSTRACT OF THE DISSERTATION OF

Brian Johnson for the degree of Doctor of Philosophy in Physics presented on August 4, 2015.

Title: Electronic and Optical Properties of Organic Semiconductors: Experiment and Simulation

Abstract approved: _____

Oksana Ostroverkhova

The continued development of organic semiconductor materials relies on an understanding of the relationship between optoelectronic properties, molecular structure, and molecular interaction. Several detailed studies of electronic properties in functionalized polyacene materials are presented. A computational model which allows the extraction of charge generation and transport properties from experimental data is developed. Ultrafast charge generation is observed, and the dependence of transient photocurrent data on this charge generation is determined. Greater crystallinitity of the donor leads to more efficient ultrafast charge generation, improving device performance. Voltage and incident intensity dependence data is fit using a single parameter set, allowing for the testing of multiple theoretical models against each other. The effect of acceptor addition to the donor material is investigated. Different acceptors allow for the isolation of effects due to packing and electronic structure interactions with the donor.

New sources for organic materials to test are important to the future of the field. One novel source for organic small molecules is the secretions of wood-eating fungi. Optical and electronic characterisation is performed on xylindein, a fungally-derived molecule, as an example of the interesting properties and challenges which this source of material present.

Electronic and Optical Properties of Organic Semiconductors: Experiment and Simulation

by

Brian Johnson

A DISSERTATION

submitted to

Oregon State University

in partial fulfillment of
the requirements for the
degree of

Doctor of Philosophy

Presented August 4, 2015
Commencement June 2016

Doctor of Philosophy dissertation of Brian Johnson presented on August 4, 2015.

APPROVED:

Major Professor, representing Physics

Chair of the Department of Physics

Dean of the Graduate School

I understand that my dissertation will become part of the permanent collection of Oregon State University libraries. My signature below authorizes release of my dissertation to any reader upon request.

Brian Johnson, Author

ACKNOWLEDGEMENTS

I have been the beneficiary of a great support network, filled with awesome people. I'm sure I'll forget someone in here, and to them my sincerest apologies, your help was greatly appreciated. Here are some people I'd like to thank in particular.

My advisor, Prof Oksana Ostroverkhova, for pointing me at good projects, helping me stay on track, and dispensing excellent advice. My wife Cassandra and all my friends, especially Barbara Martin, for putting up with my stress-induced mood swings, believing in me always, and tolerating me as I held forth at great length on my research. You are the best thinking-out-loud listeners. My fellow lab members Rebecca Grollman and Keshab Paudel for help with experiments, theory, and conversation. You made our group an awesome place to work. Genevieve Weber for being the best collaborator on the xylindein project that anyone could ask for. Prof. Matt Graham and his lab members for lab space and fluorimeter help. Jeremy Rath for helping fill out the xylindein story. My fellow grad students, especially Zach Thompson, Eric Krebs, and Matt Oostman, for being friends and providing support. My parents and siblings for always believing in me and providing me with all the opportunities that led me here. My committee members and the all the other faculty in Physics for being supportive, helpful, and knowledgable.

TABLE OF CONTENTS

TABLE OF CONTENTS (Continued)

LIST OF FIGURES

LIST OF FIGURES (Continued)

LIST OF FIGURES (Continued)

LIST OF TABLES

Chapter 1: Introduction

Organic semiconductors are a diverse class of materials with a wide range of uses, including photovoltaics (PVs),[1] LEDs,[2] and thin film transistors (TFTs).[3;4] Organic semiconductors have a variety of advantages, including flexibility, transparency, light weight, and ease of solution processing.[5–7] Additionally, the ability to adjust the solid state and solution properties of the materials via functionalization provides opportunities for continual improvement.[8] There are two classes of organic semiconductor: polymers and "small" molecules. Polymers, which consist of repeating chains of simple molecules (monomers), have been the focus of the majority of research for the last twenty plus years, particularly for OLED and PV applications.[9] Small molecules have long been dominant in TFT applications,[3] and over the last decade have received increasing interest for PV applications,[10] with new molecules slowly eroding polymer dominance in that field.[11]

This work focuses on small molecule organic semiconductors, particularly on the processes of charge photogeneration. It consists of a mixture of experiment and computer simulation. The remainder of this chapter is dedicated to the basic physics underlying the optical and electronic properties of small molecule organic semiconductors and to providing context for the active debates to which this work contributes. Chapter 2 lays the theoretical ground for the computational model used, going into greater detail on charge generation, transport, and trapping. Implementation details for the simulations are included in Ch. 2 and Appendix A. Chapter 3 presents experimental details, experimental results, and simulation results.

Chapter 4 switches gears to the general optical and electronic characterization of a novel semiconductor extracted from the secretions of tropical wood-eating fungi. Chapter 5 draws connections between the proceeding chapters in order to describe a few simple take-aways from this work and discusses directions for future research.

1.1 Basic Principles

The properties of organic small molecule semiconductor devices are largely determined by the physics of isolated molecules and the solid state packing. The isolated molecules consist of covalently bonded atoms, primarily carbon and hydrogen. The covalent bonds that hold the molecules together are a result of the electron orbitals of each atom overlaping with their neighboring atoms' orbitals. Overlapping s orbitals create σ bonds, which in C–C pairs are very tight, with the resulting electron clouds localized very close to the molecule. Overlapping p orbitals create π bonds, forming delocalized orbitals above and below the molecular plane. Both types of bond have two electronic spin states determined by the spin of the individual electrons. Opposite electron spins create the lower energy "bonding" state, while matched electron spins create the higher energy "anti-bonding" state. This is the one of the sources of the electronic energy band gap in these materials.[9;12]

The electronic energy states are split by the vibration of the molecule. In the functionalized acene and acene-thiophene derivatives which are the focus of this work, the most prominent vibrational states are different modes of elastic stretching between neighboring carbon molecules (called C–C stretching). These vibrational modes split the electronic states, with the gap between each state being 0.14–0.19 eV in our molecules, compared to electronic

band gaps of 1.9–2.5 eV.[13]

The two primary molecular backbones used in this work, anthradithiophene (ADT) and pentacene (Pn), are shown in Figure 1.1(A). They are variously functionalized by attaching different groups in the R positions (Figure 1.1(B). These are called "side groups" and primarily affect the molecular packing in the solid state, with little effect on the isolated molecule electronic structure. Some sample side groups used are also shown in figure 1.1. In addition to these, the C_{60} derivative PCBM (Figure 3.2(c)) was used as an acceptor material.

In solid state, these materials form either amorphous or polycrystalline films, with the inter-molecular bonding provided by Van der Waals forces, in contrast to the covalent bonds in inorganic semiconductor crystals.[12] Larger crystals in our films tend to lead to better electronic properies, since charge conduction depends strongly on crystalline order.[14] (See Sec. 1.1.3 and Ch. 2 for more details.) Because of the relatively weak intermolecular interaction, mobilities and electric permittivity in organic semiconductors are much smaller than in the standard inorganic semiconductors. Pristine organic semiconductor films thus often have low charge generation and charge extraction efficiencies.[9]

The crystal packing of organic materials varies greatly even among similar molecules. Two sample packing styles are shown in Figure 1.1, a 2-D "brickwork" style packing with a large overlap in the π orbitals of adjacent molecules, and a 1-D "sandwich herringbone" style with much less π–π overlap. The degree of π–π overlap is a good indicator of the strength of intermolecular coupling in the film.[15]

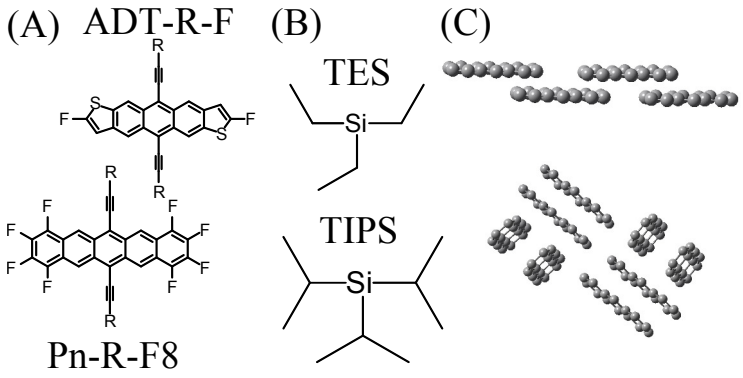

Figure 1.1: (A) Molecular structures of two organic backbones studied in this work. (B) These groups are attached at the R positions of the backbone to modify the solid state properties. (C) The solid state packing of two different ADT-F derivatives. Top: Brickwork packing of ADT-TES-F. Bottom: Sandwitch-herringbone packing of ADT-TSBS-F.

1.1.1 Figures of Merit

The focus of this work is intrinsic material properties in organic thin films. The devices we use are simple coplanar electrodes with an organic film deposited between them. I draw on work done by other groups on organic semiconductors in many different types of devices, most notably solar cells (also called organic photovoltaics or OPVs) and thin film transistors (TFTs). These devices have figures of merit that can give insight into the fundamental material parameters, providing a useful check on my results.

The primary figures of merit for OPVs are the open circuit voltage (V_{oc}), short circuit current (I_{sc}), and fill factor (FF). All three of these are shown in Figure 1.2. The V_{oc} and I_{sc} are the voltage when $I = 0$ and the current when $V_{app} = 0$, respectively. The fill factor is a measure of the power conversion efficiency, and is given by $FF = (IV)_{max}/(I_{sc}V_{oc})$. In addition to these figures of merit, many groups report the internal and/or external quantum

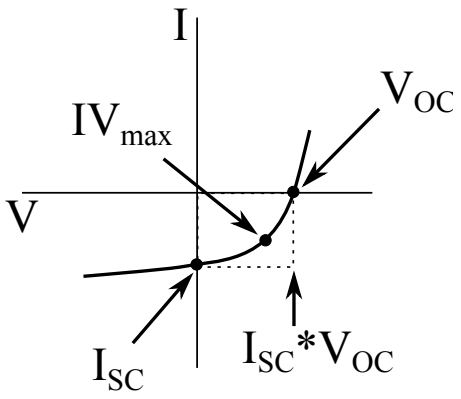

Figure 1.2: A schematic of a solar cell IV curve with important values labeled. The fill factor is a measure of how close a solar cell is to an ideal diode, and is given by the ratio $IV_{max}/I_{sc}V_{oc}$.

efficiency (IQE, EQE). The IQE is a measure of the number of absorbed photons that become free carriers in the film. The EQE is the number of collected charges per absorbed photon. These are sometimes broken down into products of the efficiencies of each step in the process, and in particular, $EQE = IQE * \eta_{collection}$, i.e. the EQE is the IQE multiplied by the efficiency of charge collection, which will be affected by transport, trapping, and electrode contact properties. In some sources, the IQE or EQE are called the "electric quantum yield" or just "quantum yield", but in this work, I prefer to use that term to refer to the ratio of fluorescence to absorbed photons, i.e. the "fluorescence quantum yield" (QY), and will not use the less specific term to refer to IQE and EQE.

A primary figure of merit for TFTs is the field effect (FE) mobility (μ_{FET}), which is an "effective" mobility which includes the effect of traps and the organic-inorganic contacts. μ_{FET} is much easier to measure than intrinsic mobility, and provides a good starting point and control for simulations.

The device properties presented in this work are related to these figures of merit in several ways. We extract "effective medium" electron and hole mobilities, which are the intrinsic mobilities; related to the field effect mobility, but with the effects of trapping disentangled. Generally speaking, a higher effective medium mobility will mean a higher field effect mobility, but because our mobility is extracted on short ($\sim$ 20 ns) time scales, it can differ from the steady-state FE mobility measurement. Measures of charge generation are functionally equivalent to measurements of EQE. Fill Factor and V_{oc} are strongly affected by charge trapping and recombination effects, for which I measure first order rates.

1.1.2 Optical Properties

Photon absorption in organic semiconductors is in some ways fundamentally different than in inorganic semiconductors. In both organic and inorganic semiconductors, the solid state structure of a film or crystal strongly affects the device properties. However, the physics of the isolated molecule contribute to organics much more than inorganics, with an effect on par with, and often difficult to disentangle from, the crystal structure. In addition, much lower dielectric constants in organic semiconductors lead to dynamics dominated by excitonic considerations, rather than the delocalized bands that determine inorganic semiconductor physics.[16]

The molecular energy level structure of organic semiconductors are traditionally defined in terms of the highest occupied molecular orbital (HOMO) and lowest unoccupied molecular orbital (LUMO). The HOMO and LUMO levels do not map nicely onto the single particle electronic levels (usually written as S_n for singlet states and T_n for triplet states), though

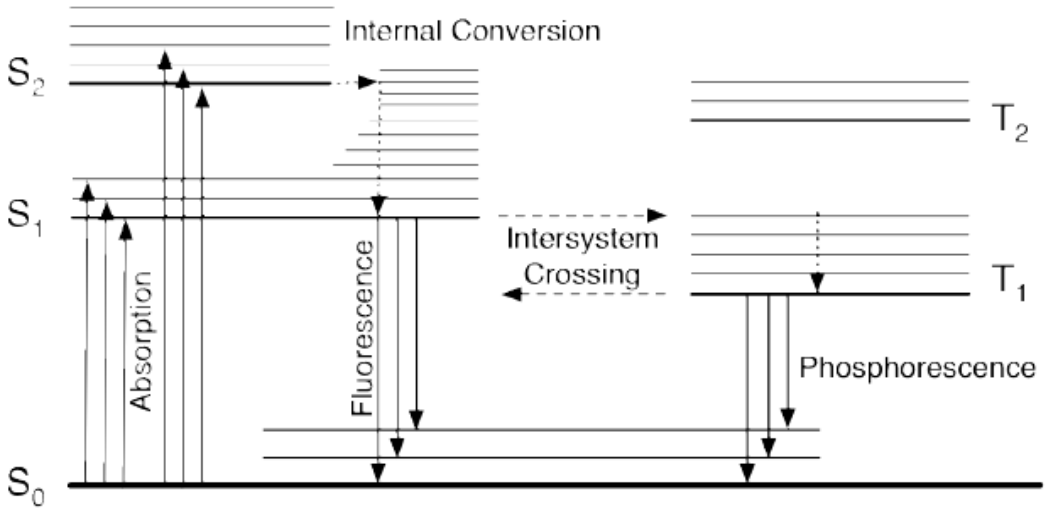

Figure 1.3: Schematic of energy levels and transitions in an isolated organic molecule.

the HOMO-LUMO energy gap is roughly equal to the S_0–S_1 gap plus the exciton binding energy. Figure 1.3 is a schematic of the energy levels and various transitions of an isolated organic molecule.

A photon absorbed by an organic semiconductor promotes an electron from S_0 to S_n (from the HOMO to an excited state) or to one of the vibrational sublevels of S_n. In the vast majority of materials, transitions from S_n to the S_1 (LUMO) state occur much more quickly than transitions from S_1 to S_0.[17] This observation is codified in Kasha's rule, which states the all fluorescence occurs from the lowest excited state.[18] An immediate consequence of this is Vavilov's corrollary, that the quantum yield of a material is independent of wavelength. Energy in excess of E_{gap} dissipates much faster than the $S_1 \rightarrow S_0$ fluorescent transistion. After carriers relax to the S_1 state, usually within 1–2 ps, spontaneous fluorescence occurs between

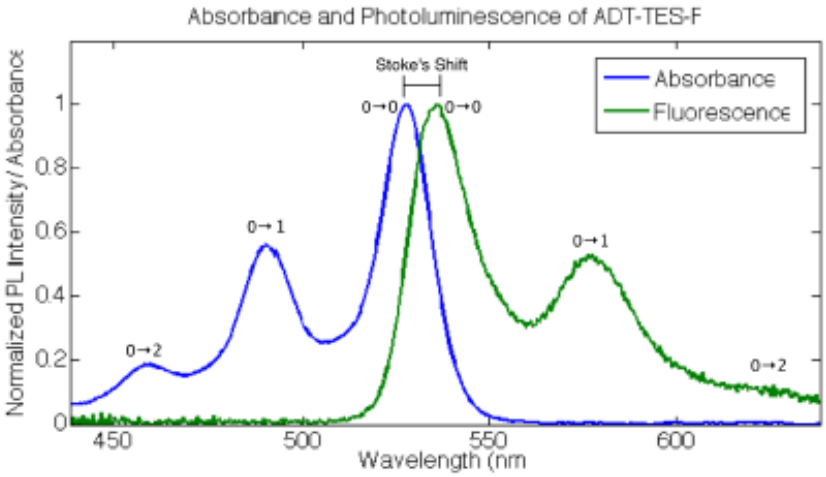

Figure 1.4: Absorption and fluorescence spectra for the donor material ADT-TES-F. The vibronic progression and Stoke's shift are noted.

S_1 and the various vibronic sub-levels of S_0, giving rise to the multi-peak fluorescence shown in Figure 1.4. The lifetime of the S_1 state is usually on the order of 1–10 ns. The energy shift visible in Figure 1.4 between the lowest absorption and highest fluorescence peak is called the "Stokes shift" and is caused by energy losses due to molecular and vibrational relaxation within the S1 state.[19]

The excited electron may still be coulombically bound to the hole it left behind, creating an "exciton". In organics, these excitons are tightly-bound "Frenkel excitons" due to the low dielectric constant. In inorganics, excitons are generally loosely-bound "Wannier-Mott excitons," which only form at very low temperatures. In solid state, the exciton can diffuse through the film, but in solution the exciton is isolated to a single molecule, leading to eventual radiative or non-radiative recombination.[20]

Photon absorption occurs very quickly, on a sub-femtosecond time scale, but spontaneous

photon emission is a slower process, determining the lifetime of the S1 state.[16] If a short laser pulse excites a population N_1 of electrons to the first excited state, then after the laser pulse has passed these electrons will leave the excited state via radiative recombination, non-radiative recombination, or intersystem crossing to the triplet state (see Figure 1.3). Since spin switching is forbidden in the Born approximation, intersystem crossing rates are usually an order of magnitude or more smaller than the recombination rates.[16] Considering just recombination, the change in population of the excited state for an isolated molecule can be described by a simple, analytic differential equation:

$$\frac{dN_1}{dt} = -\left(k_r^s + k_{nr}^s\right) * N_1 \tag{1.1}$$

$$\implies N_1(t) = N_1(0)\, e^{-\frac{t}{\tau_s}} \tag{1.2}$$

$$\tau_s = \frac{1}{k_r^s + k_{nr}^s} \tag{1.3}$$

where k_r^s and k_{nr}^s are the rates of radiative and nonradiative recombination, respectively. The fluorescence intensity is given by the number of electrons which decay radiatively, and is proportional to the excited state lifetime: $I(t) = k_r^s * N_1(0) * e^{-\frac{t}{\tau_s}}$. We can thus fit transient photoluminescence (TPL) data taken in solution to an exponential curve to extract the excited state lifetime of the sample. In solid state, additional relaxation pathways are provided via exciton dissociation, fast diffusion to recombination centers, aggregate formation, etc., leading to multi-exponential TPL graphs. Fitting these more complicated graphs still provides valuable information about the time scales of fluorescence. Combined with photocurrent measurements and simulations, a great deal of insight into the nature of the charge generation process can be gathered.[13;21]

1.1.3 Electronic Properties

1.1.3.1 Photogeneration

Photogeneration of charge carriers in organic semiconductors proceeds much differently than in inorganic semiconductors. The low dielectric constant causes the Coulomb force between a newly created electron and hole pair to be strong relative to the electron screening effect, creating a Frenkel exciton.[20] In order for free charge carriers to be generated, this exciton must dissociate into its component electron and hole. The question of the electric field dependence of exciton dissociation in organic semiconductors arose in the 1960s and 70s, alongside the first demonstration of photocurrent in organic donor-acceptor composite films.[22;23] The process of this generation was, and often still is, visualized as a multi-step process, where an exciton is created in the donor and then diffuses to a donor-accceptor boundary, where the electron transfers to the acceptor, creating a charge-transfer (CT) exciton and then dissociating into a hole on the donor and an electron on the acceptor.[24] The CT exciton dissociation step was the focus of initial theoretical work on electric field dependence. Until the mid 80s, the most used model was from a 1938 paper by Onsager,[25] where he considered the electron field and initial separation dependence of the recombination rate of electron-ion pairs in a dense gas. This model does not admit a simple closed form solution for the dissociation rate k_d, but has a reasonably accurate series expansion:

$$k_d\left(a, E, \theta\right) = exp\left(-2q/a\right)\left[1 + 2\beta q\left(1 + cos\theta\right) + \beta^2 q\left(q - a\right)\left(1 + cos\theta\right)^2 + ...\right] \tag{1.4}$$

where a is the initial pair separation, θ is the orientation of the pair relative to the electric field, $q = e^2/2\epsilon_r\epsilon_0 kT$, $\beta = eE/2kT$, E is the applied electric field, e is the fundamental charge, k is Boltzmann's constant, T is the temperature, ϵ_0 is the permittivity of free space, and ϵ_r is the relative permittivity.

This 1938 Onsager model had some initial success in fitting the electric field dependence of EQE in early organic semiconductors such as anthracene crystals.[23] However, by the mid 1980s it had become apparent that many organic semiconductors, especially polymer films, had electric field and temperature dependence that were not well explained by this 1938 model.[26] Specifically, the initial pair separations required to fit the model to experimental data were unphysically large.[26] In 1984, Braun tackled this problem,[26] revisiting both the base, zero-field exciton dissociation rate and the electric field dependence of the rate. He proposed two different zero-field rates, one based on a solution for Wannier-Mott excitons,[27] the other based on an ion pair model.[28] For the electric field dependence of the dissociation, he reached back to a 1934 Onsager paper,[29] where Onsager had derived the electric field dependence of the dissociation of a weak electrolyte. He also showed that the new model, using the ion pair base rate, was a special case of a more general dissociation model developed in the late 1970s by Noolandi and Hong.[30] This solution for the dissociation rate became known as the "Onsager-Braun" model, and is the exciton dissociation model used in this work. The equation Braun derived is

$$k_d\left(a, E, T\right) = \frac{3\gamma}{4\pi a^2} exp\left(-\frac{\Delta}{kT}\right) \frac{J_1\left(2\sqrt{-2b}\right)}{\sqrt{-2b}} \tag{1.5}$$

where $\gamma = \frac{e(\mu_n+\mu_p)}{\epsilon_r\epsilon_0}$ is the Langevin bimolecular recombination rate, $\Delta = e^2/4\pi\epsilon_r\epsilon_0 a$ is the

Coulombic binding energy, J_1 is the first regular Bessel function, $b = e^3E/8\pi\epsilon_r\epsilon_0k^2T^2$, and $\mu_{p(n)}$ is the hole(electron) mobility.

The Onsager-Braun model has become the new "traditional" exciton dissociation model. One of its chief advantages over other models is its ease of implementation into many types of numerical simulations and curve fitting algorithms. However, the validity of the Onsager-Braun model has been extensively questioned, especially in the last decade or so.[31–33] One of the strongest critiques comes from Tachiya and his cowriters.[33] In a 2009 paper, they derive an exact extension of the Onsager theory, showing that it deviates from the predictions of Braun's extension at high electric fields ($> 10^5$ V/cm). However, they only derive total photogeneration efficiency, not a rate constant for dissociation, making it unsuitable for transient simulation. In addition, for the electric fields used in this work (between $2 * 10^4$ and $8 * 10^4$ V/cm), the Braun model performs well.[33]

Braun's observation that his model is a special case of a more general exciton dissociation model developed in the late 1970s by Noolandi and Hong is an argument in favor of its use.[26] This general model was extended in the 1990s and 2000s by Tachiya and coworkers.[34] The Noolandi-Hong-Tachiya model considers a pair of oppositely charged particles whose diffusion is described by the time-independent Smoluchowski equation, with the boundary conditions of a finite recombination radius r_k and a recombination velocity at that radius of κ.[30]

At zero-field, the limit $r_k \to 0$ and $\kappa \to$ inf recovers Onsager's 1938 result, while the constraint $r_k = a$ recovers the exciton dissociation rate of the Onsager-Braun model (Eq. 1.5), less a factor of three.[26;33] Wojcik and Tachiya, in their 2009 paper,[33] showed that this extra factor of three in the Onsager-Braun model is due to it not properly considering the full recombination surface. In simulation, this extra factor of three will affect primarily

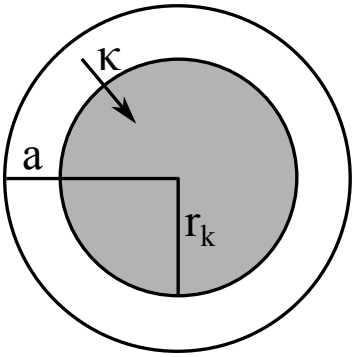

(a) Schematic of Noolandi-Hong-Tachiya model. Initial pair separation is a, and recombination velocity is κ.

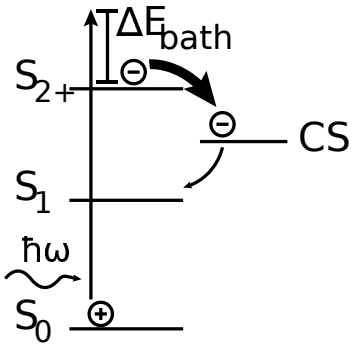

(b) Schematic of hot exciton model. ΔE_{bath} dissipates before the CS $\rightarrow S_1$ transition can occur.

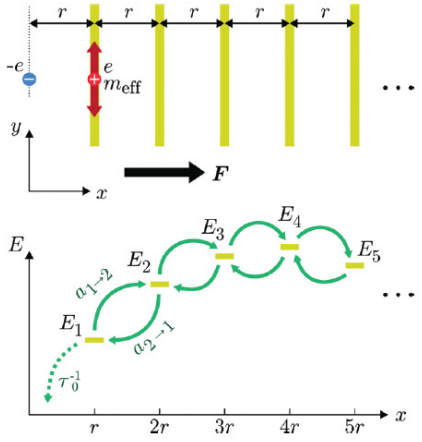

(c) (top) Schematic of delocalization model with a mobile hole. (bot) Energy level schematic of the various hole positions. From Baranovskii et al.[35]

the calculated initial pair separation. The Onsager-Braun model as widely used maintains this factor of three, and so the initial set of simulations have this factor. Later simulations discard this factor of three as indicated by the Noolandi-Hong-Tachiya theory in the hope of improving the accuracy of the initial pair separation value. This change is discussed in more detail in chapter 2.3.1. One direction of future work is to investigate alternate dissociation models, testing the quality of the fits and extracted parameters over multiple samples.

Early investigations into the mechanism of charge generation in organic semiconductors focused on cataloguing the electric field, temperature, and excitation wavelength dependece of the photoinduced current.[22;23;30] Conjugated polymers were an initial focus of several groups,[36;37] as the assumption of free 3-dimensional carrier movement used in the Onsager and Onsager-Braun theories is violated in these systems. The length of the individual conjugated segments in these polymers is often larger than the coulomb capture radius (i.e. r_k),

indicating that diffusion is likely to be highly anisotropic, with movement along the polymer chain easier than movement between polymer chains.[31] By the end of the 20th century, it had been well-established that many conjugated polymers had an excitation wavelength dependent photocurrent and EQE inconsistent with the predictions of the Onsager-Braun model, where increasing wavelength increases initial pair separation, increasing the dissociation rate.[31] The EQE in conjugated materials is often flat below a material-specific temperature, only following the predictions of the Onsager-Braun model at high temperatures. In 1999, Arkhipov, et al. proposed a model premised on "hot excitons" to explain these experimental results. There are several versions of the model,[38;39] but they follow a similar underlying argument.

The hot exciton model relies on incident photons with energies larger than E_{gap} pushing the excited electron and hole into an initial state which has total energy greater than the bandgap. This state decays within the first $\sim$100 fs after excitation, into a ground state exciton ($E = E_{gap}$) and a collection of phonons ($E = \hbar\omega - E_{gap}$). These high-energy phonons create a "thermal bath" which effectively raises the local temperature, assisting the dissociation of the ground state exciton. The initial decay occurs on a time scale much shorter than the molecular relaxation time, but the resulting phonons will decay on about the same time scale as the ground state excition reforms. Thus, excitons which dissociate due to this thermal bath will find the bath has dissipated before they can recombine into an exciton, making the process effectively one-directional. In some versions,[31] excitons which do not dissociate initially will form relaxed Frenkel excitons, and can dissociate on longer time scales. Arkhipov, et al. derived an expression for IQE as a function of electric field, temperature,

and initial excitation energy assuming a constant energy dissipation rate β:

$$IQE\left(F,\langle E_0\rangle\right)=\int_0^1\left(1-exp\left[-\frac{\nu_0}{\beta}\int_0^{\langle E_0\rangle}Bol\left(\frac{E_b}{\langle E\rangle}-\frac{e}{\langle E\rangle}\sqrt{\frac{eFz}{\pi\epsilon_0\epsilon_r}}\right)d\langle E\rangle\right]\right)dz \quad (1.6)$$

where F is electric field, $\langle E\rangle = \langle E_0\rangle - \beta t$ is the excess energy remaining after a time t, $\langle E_0\rangle = \hbar\omega - E_{gap}$ is the excess photon energy, $z = cos\phi$, ϕ is the angle between a specific segment and F, and ν_0 is the "attempt-to-jump" frequency. This solution fits well to the field, temperature, and excitation energy dependence of IQE in pristine MeLPP[31] and several other conjugated polymers.[38] Unfortunately, in many small molecules, including those used in this study, the intrinsic photocurrent has little to no dependence on excitation wavelength above the band gap,[40] making the application of hot exciton models questionable. It cannot be completely ruled out as a mechanism for ultrafast charge generation, however.

Another class of theories competing to replace the Onsager-Braun model fall under the moniker "carrier delocalization." These models rely on an increasing body of evidence, driven by significant improvements in ultrafast experimental techniques over the last $\sim$ 15 years,[1] showing that primary charge generation in many types of organic semiconductor films occurs on an extremely fast time scale. Ultrafast pump-probe absorption measurements with time resolutions as low as 100 fs or even less[24;32;41;42] combined with ultrafast photoconductivity measurements[32] have revealed that in the best performing organic photovoltaic films, the initial creation of free carriers can occur with a time constant of less than 1 ps. In addition, measurements of internal quantum efficiency (IQE) in organic photovoltaic devices are very large.[9] In some materials, an IQE nearing 100% has been obtained, even at exciting wavelengths near the band gap.[43] The Onsager-Braun model requires extremely long exciton

lifetimes to explain these experiments, much longer than experimental exciton lifetimes.[44] This process is also much faster than diffusion, inconsistent with the traditional image of excitons diffusing to donor-acceptor boundaries.

Delocalization models assume that the initial excitation creates an exciton which is delocalized across multiple lattice elements (either molecules or monomers). Unlike with hot exciton models, which differ primarily in small details, there are several very different approaches to modeling this process. Kaake et al. argue[32] that the delocalization can be understood as a simple result of time-energy uncertainty. The excitation will then localize on the order of decoherence, usually under 100 fs. When the electron and hole localize, they can localize to positions far enough from their pair that they are effectively free charge carriers. This can explain both high IQE and sub-1 ps pump-probe measurements.

Other models are more complex. Nenashev et. al,[45] following earlier work,[46] model a donor material as a set of one-dimensional chains parallel to the D/A interface, placed equidistantly (Figure 1.5c). A hole on a donor chain is delocalized along the full length of the chain, while the electron is localized and fixed at the D/A interface. They then solve this model analytically to derive a probability of dissociation, as well as numerical simulations of the electric field dependence of this probability. They were able to qualitatively fit the electric field dependence of experiments, but the actual values were much smaller than those found in experiments, indicating that this model is incomplete.[45]

1.1.3.2 Transport

Carrier transport in crystalline inorganic semiconductors is well understood.[47] Strong electronic coupling between adjacent atoms gives rise to highly delocalized carriers, occupying well defined energy bands. The "Fermi level" is the ground-state energy of the material, with bands under the Fermi level occupied and bands above the Fermi level unoccupied. In most semiconductors, the Fermi level lies within the "bandgap" of the material, an energy range in which there are no or very few allowed states. The highest energy band under the Fermi level is the "valence band" and the lowest energy band above the Fermi level is the "conduction band". Carriers can be promoted from the valence band to the conduction band through photoexcitation, doping, or device structure, allowing current to flow. Carrier "traps" occur at lattice distortions created by impurities or dopants, and trapped carriers are highly localized compared to mobile carriers. This is the "band model" of transport. Band transport can be identified through an inverse temperature dependence and a flat carrier density dependence of mobility, as well as by high mobilities (e.g. $\mu_e \sim 1400\ cm^2/Vs$ in silicon at room temperature).

Organic semiconductors have a very different solid state structure, forming either amorphous films or crystals held together with Van der Waal's forces, much weaker than the covalent bonds in inorganic semiconductors.[12] As a result, the strong inter-molecular coupling which gives rise to delocalized bands in inorganics does not exist. However, if there is strong electron-phonon coupling in the solid state, "polarons" will act as the primary charge carriers. Polarons are quasi-particles consisting of an entangled electron-phonon pair. Most organics satisfy this condition, and polarons are likely the charge carriers in ADT-TES-F

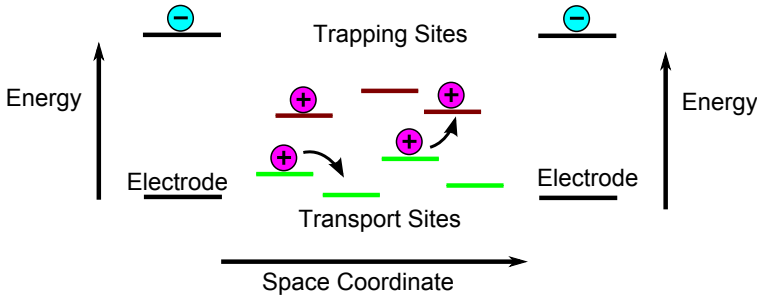

(a) Schematic of hopping transport with traps. Traps are formed by sites with particularly high energies.

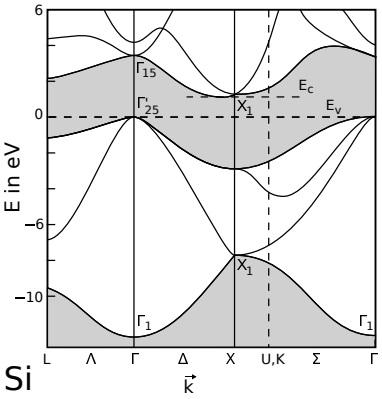

(b) Schematic of the band structure of Si.[49] Shaded areas are the conduction (top) and valence (bot) bands.

and Pn-R-F. If there is a strong long range order in the solid state, then polarons with long wavelength phonon components may delocalize sufficiently to form bands.[48]

The classic model for transport in lower mobility organic semiconductors is the "hopping model".[2] In this model, carriers are localized to the potential wells of individual molecules or monomers, with the film or crystal acting as a periodic lattice of potential wells. The energy of individual potential wells varies and the distribution of these energies is called the "density of states"(DoS). Thermally activated carriers can "hop" from well to well. In zero field situations this motion is random and so gives rise to no net current. An applied electric field biases the random walk in the direction of electric field, generating current. Carrier traps in this model are simply potential wells that are much deeper than the thermal energy $E_{kt} = k_B * T$, causing carriers in those states to have a much lower than average hopping probability.[50] Photocurrent is generated by exciting ground state carriers to a higher energy, making it more likely for them to hop. Hopping transport is characterized by low mobility

($< 10^{-7}$ cm^2/Vs in PPV at room temperature[51]), which decreases at very high carrier densities and as temperature decreases.

The hopping model describes low mobility organic semiconductors very well.[52] High mobility (20 cm^2/Vs in rubrene at room temperature[53]) single crystal organic semiconductors have signatures of band transport, notably an inverse temperature dependence.[54–56] This is often referred to as "band-like" transport. These materials exhibit behavior that lies between hopping and band transport. An iconic example of this is polycrystalline films of oligoacenes (e.g. Pentacene).[57] Measurements of Pn films reveal an increasing mobility with decreasing temperature between 100 and 300 K, as well as a Hall effect magnitude more consistent with band transport than hopping transport.[55] However, direct measurements of carrier localization[58;59] reveal carriers that are localized to single molecules. This seeming contradiction appears in many high-performing organic semiconductor materials, small molecule and polymer alike. Some materials, ADT-TES-F among them, even show a change in these transport characteristics depending on the exact film structure.[14]

This inconsistency led to a search for a better transport model that is still ongoing. One of the earliest models was proposed by Troisi and Orlandi.[60] Their model is semiclassical, with the molecular lattice represented as classical oscillators and the transfer integrals between adjacent states represented using quantum mechanics. The oscillation of the molecular sites represents thermal disorder in the lattice, and they calculated a qualitatively correct temperature and electric field dependence of mobility using their model. Charge carriers are localized primarily by thermal disorder, leading to more localization (and lower mobility) with increased temperature. While the first paper was confined to one dimension, later work showed that this model also performs well quantitatively and qualitiatively when extended

to 2D.[53] The semiclassical treatment of the phonons may be justified due to the modes responsible for dynamic disorder being low energy, with $\hbar\omega << k_B T$ at room temperature.[48]

Troisi's model received much criticism for this classical treatment of phonons.[48] The development of fully quantum approaches following similar logic to the semiclassical model has continued,[61] but a truly satistfactory model has yet to be arrived at. This is largely due to the complexity of the elecron-phonon system in crossover materials. The tight-binding Hamiltonian for a one electron-one phonon system in a crystal lattice contains three terms: the energies of the electron and phonon individually and an interaction matrix describing the electron-phonon coupling. Diagonal elements of the electron-phonon matrix represent local coupling, while the off-diagonal elements represent long distance coupling. If the off-diagonal elements dominate, then a polaronic band-like tranport model results, with carrier delocalization reducing as temperature increases. Conversely, if the diagonal elements are large, hopping of highly localized polarons results. In cross-over materials such as Pn, the diagonal and off-diagonal elements are of comparable magnitude, requiring a full numeric solution of the Hamiltonian, a challenging and unsolved problem.[48]

Several groups have proposed fully quantum mechanical models following the basic logic of Troisi.[61–63] Full discussion of the various models is beyond the scope of this work, especially since active refinement of models and numeric techniques continues in the literature.[61]

1.1.3.3 Trapping

Trapping in organic semiconductors proceeds differently depending on the transport model. For band and band-like transport, traps occur at crystal grain boundaries, impurities, and

other lattice distortions. The highly delocalized charge carriers that encounter a trap localize, falling into a lower energy state. To escape the trap, the carrier must transistion back to a delocalized state through phonon absorption or some other mechanism. Traps in this model are best described in terms of a trap density and single trapping and detrapping rates.

In the hopping model, the depth of each localized potential well varies, with hopping out of "deep" states being much slower than hopping out of "shallow" states.[50] On the nanosecond time scale, the separation betwen shallow states where most carrier movement occurs and deep trapping states which hold onto charge carriers for a relatively long time is significant enough that the exact density of states is not needed. Because of this, DoS measurement will not be considered in this work, though it is an area of active research.[64] The DoS distribution depends on the source of the traps; "shallow" traps with energies near the mobility edge usually follow an exponential distribution, while "deep" traps with energies much lower than the mobility edge will often display a Gaussian distribution.[64;65] In ADT-TES-F, the deep trap lifetime is extremely long, on the order of hours or even days.[40] The traps considered on the simulation time scale are shallow traps, with trapping and detrapping occuring on nanosecond or tens of nanoseconds time scales. These traps likely have an exponential DoS; in Pn films, widths of 35–45 meV for these kind of shallow traps have been found.[65]

In the hopping transport framework, the rate of hopping from site i to site j is given by the Miller-Abraham rate expression:[66]

$$W_{ij} = \begin{cases} \nu_0 \; exp\left[-2\alpha R_{ij} - \beta\left(\epsilon_j - \epsilon_i\right)\right], & \epsilon_j \geq \epsilon_i \\ \nu_0 \; exp\left[-2\alpha R_{ij}\right], & \epsilon_j < \epsilon_i \end{cases} \tag{1.7}$$

where $\beta = 1/k_BT$, ν_0 is an intrinsic "attempt to jump" rate, R_{ij} is the distance between sites i and j, α is the inverse localization length of the carrier wave function, and ϵ_i is the energy of site i. In bulk simulations, these rates are effectively averaged over the density of states of the material, leading to the single trapping and detrapping rates presented in Ch. 3.

Traps arise for several reasons in organic semiconductors.[67] As in inorganic semiconductors, impurities which cause lattice defects create traps.[68] Additionally, there are intrinsic traps created by a distribution of accessable energy levels due to the strong effect local environment has on electronic structure in organics.[67] In polycrystalline films, these traps often form at lattice distortions caused by crystal domain boundaries.[69]

1.1.3.4 Recombination

Recombination is the primary loss mechanism for photogenerated carriers in organic devices. Recombination of charges is traditionally split into two distinct categories: geminate and non-geminate recombination. Geminate recombination occurs when an excited exciton recombines before dissociating into free charge carriers. In efficient materials such as ADT-TES-F, initial charge generation is very efficient, so non-geminate recombination has by far the larger effect on photocurrent in devices. The most important type of non-geminate recombination in organic semiconductors is bimolecular recombination (BR), where an electron and hole encounter each other while moving through the film and recombine. BR has been noted as one of the primary limits on the power conversion efficiency of the current generation of organic solar cell materials.[70]

The traditional model for BR was developed by Langevin in 1903[71], which considers a free electron and free hole that recombine instantly when they reach the coulomb capture radius $R_c = \frac{e^2}{4\pi\epsilon_0\epsilon_r kT}$. Both the electron and hole move with mobilities μ_n and μ_p, respectively; by considering an identical situation where the electron is fixed and the hole moves with mobility $\mu = \mu_n + \mu_p$, he derived the recombination rate $\gamma = \frac{e\mu}{\epsilon_0\epsilon_r}$.[71] This model is the one used in my simulations.

The Langevin model was shown to be reasonable in several crystalline organic semiconductors in the 1960s.[70] As devices became more optimized, however, BR effects were reduced, such that in modern devices the Langevin model significantly overestimates the losses due to BR. Several models have been proposed to replace it, all following the same basic logic as the Langevin model.[70] One notable replacement was proposed by Hilczer and Tachiya in 2010.[72] They attempted to unify the geminate and bimolecular recombination models, proposing that when electrons and holes approach each other, they will not immediately recombine, but rather form an exciton which will then either recombine or re-dissociate.

A weakness in the Langevin theory when applied to organic semiconductors is the absense of trap-assisted recombination. Trap-assisted recombination occurs when a mobile hole or electron enters a trap state which is holding a complementary carrier, causing the trapped charge and free charge to recombine. The traditional model for trap-assisted recombination is Shockley-Read-Hall (SRH) recombination, which has seen much success in inorganic semiconductors.[70] SRH recombination has a monomolecular dependence (i.e. $R_{SRH}\ \alpha\ n$), unlike the clearly bimolecular character of non-geminate recombination in many organic materials. In my simulations, trap-assisted recombination has a bimolecular character, but I make no assumptions about the rate.

Chapter 2: Theory

2.1 Motivation

2.2 Drift-Diffusion Model

The canonical approach to modeling current in metals and high mobility semiconductors is called the Drude-Sommerfeld model. This model treats free electrons in the conduction band (holes in the valence band) as an ideal electron gas. While the individual carriers are delocalized wave packets, the density of the carriers is treated semi-classically in this model. Consistent with the semiconductor literature, I refer to "carriers" and "carrier density" interchangeably. Charge carriers in traditional materials are electrons or holes with an effective mass m*, however, the nature of the charge carriers in organic semiconductors is not settled.[48] In our materials, the electron-phonon coupling is large enough that it is likely that charge is carried by entangled electron/hole–phonon pairs. This entanglement gives rise to a pseudo-particle called a "polaron". The Drude-Sommerfeld model is adapted simply here to polarons which move with a mobility μ, rather than electrons and holes with an effective mass m*. The remainder of this work refers to mobile, large-bandwidth polarons as "free carriers" and to immobile, small-bandwidth polarons as "trapped carriers".

With no electric field applied, charge carriers move primarily under the influence of Brownian motion. This "diffusion" is a random walk, but as in a classical gas, the density of carriers will tend to uniformity. When the carrier density in a material is nonuniform (due

to applied electric field, nonuniform excitation, etc.), this motion gives rise to a diffusion current, which can be written

$$\vec{J}_{\text{diff},p} = eD_p\vec{\nabla}p_f \tag{2.1}$$
$$\vec{J}_{\text{diff},n} = eD_n\vec{\nabla}n_f$$

where e is the fundamental charge, $p_f(n_f)$ is the free hole(electron) density, $D_{p(n)}$ is the hole(electron) diffusion constant, usually assumed to obey the Einstein relation $D_{p(n)} = \frac{k_BT}{e}\mu_{p(n)}$ where k_B is the Boltzmann constant, T is temperature, and $\mu_{p(n)}$ is the hole(electron) mobility.

When an electric field is applied, the carriers will "drift" in a direction determined by that electric field, at a speed determined by the mobility of the carrier in the material. This drift gives rise to a current proportional to electric field which can be represented as

$$\vec{J}_{\text{drift},p} = e\mu_p p_f\vec{E} \tag{2.2}$$
$$\vec{J}_{\text{drift},n} = e\mu_n n_f\vec{E}$$

where E is electric field.

The total carrier density in the device must follow Gauss's law $\vec{\nabla}\cdot\vec{E} = \frac{\rho}{\epsilon_0\epsilon_r}$ where ρ is charge density, ϵ_0 is the permittivity of free space, and ϵ_r is the relative permittivity of the material. Substituting the free (p_f, n_f) and trapped (p_t, n_t) carrier densities for ρ and the

electric potential given by $\vec{\nabla}V = E$ gives us the Poisson equation in a semiconductor

$$\nabla^2 V = \frac{n_f + n_t + p_f + p_t}{\epsilon_0 \epsilon_r} \tag{2.3}$$

Current continuity in the semiconductor is described by Ampère's law with Maxwell's correction $\vec{\nabla} \times \vec{H} = \vec{J} + \epsilon_0 \epsilon_r \frac{\partial \vec{E}}{\partial t}$. Taking the divergence of each side, using Gauss's law to insert the carrier densities, and rearranging, we get the continuity equations

$$\frac{\partial p}{\partial t} = -\frac{1}{e}\vec{\nabla} \cdot \vec{J_p} + (G_p - R_p) \tag{2.4}$$

$$\frac{\partial n}{\partial t} = -\frac{1}{e}\vec{\nabla} \cdot \vec{J_n} + (G_n - R_n) \tag{2.5}$$

where p(n) is the total hole(electron) carrier density, $\vec{J}_{p(n)} = \vec{J}_{diff,p(n)} + \vec{J}_{drift,p(n)}$ is the total hole(electron) current density, $G_{p(n)}$ is a hole(electron) generation term, and $R_{p(n)}$ is a hole(electron) loss term.

The model presented here incorporates generation of free carriers occurs when light is incident on the sample with rate $G_{p(n)}$ and through the detrapping of trapped carriers with rate $B_{p_t(n_t)}$. Free carriers become trapped carriers with rate $B_{p(n)}$, and are lost when they recombine bimolecularly with rate γ and when they experience trap-assisted recombination with rate $B_{p_f n_t(n_f p_t)}$. Trapped charge carriers do contribute to the current, are generated only when free carriers are trapped, are lost through trap-assisted recombination, and become free carriers by "detrapping" with rate $B_{p_t(n_t)}$. There is a finite hole(electron) trap density $N_{p(n)}$, with trapping slowing down as the traps fill.

Solving the full 3-dimensional version of these equations is extremely computationally

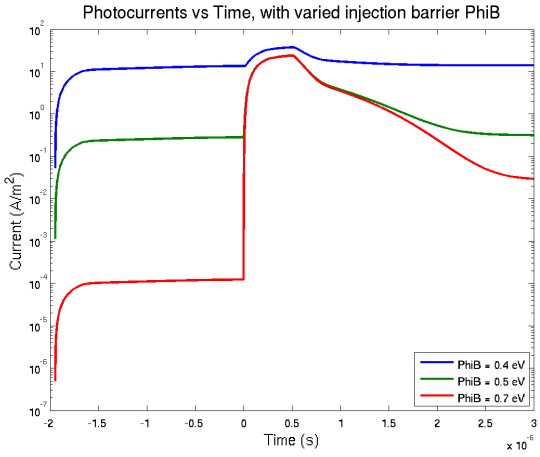

Figure 2.1: A sample of transients simulated using the full Drift-Diffusion model on 1 μm devices, showing the effect of variations in the hole injection barrier.

expensive, so in most cases a one dimensional approximation is applied. In planar or stacked devices where generation and recombination are reasonably uniform across at least two of the space dimensions, we assume the off axis currents are small and randomly distributed, leading to the one dimensional drift-diffusion model with trapping effects

$$\frac{\partial^2 V}{\partial x^2} = \frac{n_f + n_t + p_f + p_t}{\epsilon_0 \epsilon_r} \tag{2.6}$$

$$\frac{\partial p_f}{\partial t} = \frac{1}{e}\frac{\partial J_p}{\partial x} + G_p + B_{p_t} p_t - B_p (N_p - p_t) p_f - B_{p_f n_t} p_f n_t - \gamma n_f p_f \tag{2.7}$$

$$\frac{\partial n_f}{\partial t} = \frac{1}{e}\frac{\partial J_n}{\partial x} + G_n + B_{n_t} n_t - B_n (N_n - n_t) n_f - B_{n_f p_t} n_f p_t - \gamma n_f p_f \tag{2.8}$$

$$\frac{\partial p_t}{\partial t} = B_p (N_p - p_t) p_f - B_{p_t} p_t - B_{p_f n_t} p_f n_t \tag{2.9}$$

$$\frac{\partial n_t}{\partial t} = B_n (N_n - n_t) n_f - B_{n_t} n_t - B_{n_f p_t} n_f p_t \tag{2.10}$$

$$J = eE\left(\mu_p p_f + \mu_n n_f\right) + k_B T \left(\mu_p \frac{\partial p}{\partial x} + \mu_n \frac{\partial n}{\partial x}\right) \tag{2.11}$$

This system of partial differential equations can be solved computationally by discretizing time and space into N_t and N_x segments of size Δt and Δx, respectively. However, in order for the model to give physical results, Δx must be much smaller than the product $\mu * E * \Delta t$, and Δt must be much smaller than the time scale of any transient effects. For solar cells in the literature using nanosecond pulsed excitation,[73] devices are on the order of ∼200 nm thick, and the required (N_t, N_x) are small enough to solve in a few seconds on modern computers. An example of some transients simulated using this method are shown in Figure 2.1. For my experiments, the width of the device is 25 μm and the pulsed excitation is ∼500 ps, requiring several orders of magnitude larger N_t and N_x. After several weeks of algorithm optimization, a single solution with our experimental parameters required several hours. Since fitting simulations to experimental data can be expected to require as many as 10^4 or 10^5 solutions for one fit, this task is computationally impossible. This led to the need to develop a model which would be much faster to solve.

2.3 Drift-only Model

To construct a computationally solvable model, I assumed that the electric field and carrier densities can be averaged to a uniform spatial distribution and that under my experimental conditions drift current dominates over diffusion. The former assumption is supported by my group's previous observation of weak fast photocurrent transient amplitude and dynamics dependence on the position of a localized excitation in the gap between the electrodes.[13] The latter consideration is similar to that applied to modeling cw photocurrent dynamics in, e.g., photorefractive polymer devices[74;75] and to modeling transient photocurrent decays[76]

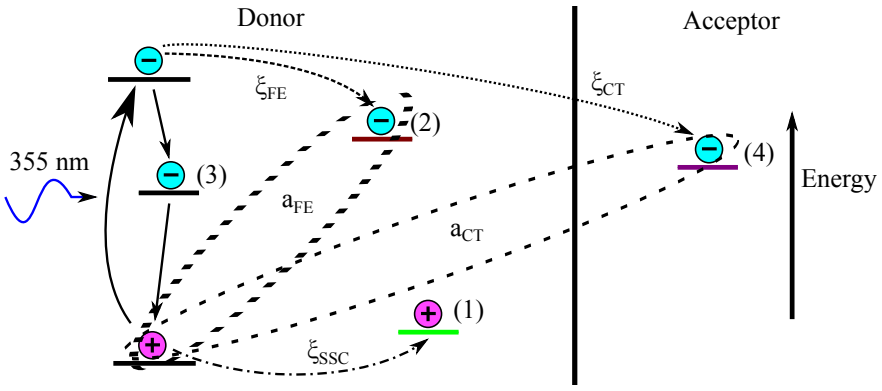

Figure 2.2: Schematic of the different relaxation pathways upon photoexcitation, with pathways 1, 2, and 4 leading to charge generation described by the model of Eqs. 2.15–2.26. (1) Fast formation of spatially separated carriers (SSC); (2) Formation of a Frenkel exciton (FE) in ADT-TES-F, which can dissociate at ns time-scales to free charge carriers; (3) Formation of a relaxed exciton that does not yield free charge carriers at ns time-scales and instead recombines to the ground state either radiatevely or non-radiatively; (4) Charge transfer (CT) exciton in D/A composites that can dissociate to free carriers during its lifetime.

in polymeric devices with channel lengths on the order of tens of microns.

2.3.1 Charge Photogeneration

My group's previous studies of pristine ADT-TES-F films revealed fast charge carrier photogeneration (inferred from sub-30 ps photocurrent rise times under 100 fs pulsed excitation, limited by the time resolution of the DSO detection), high cw photoconductivity, and relatively strong PL,[13;40;77] which indicates the existence of several relaxation pathways following photoexcitation. In particular, fast charge carrier photogeneration observed upon excitation of films with a pulsed light with a photon energy considerably above the ADT-TES-F HOMO-LUMO gap of 2.3 eV (such as with a 3.49 eV light used here) could be due to a direct

band-to-band excitation of charge carriers[32] or due to hot exciton dissociation at ps or sub-ps time scales.[31;78] Regardless of the exact origin of the carriers created on fast (ps or sub-ps) time scales, in further discussion I will refer to such carriers as "spatially separated carriers" (SCC) (charge generation path 1 in Fig. 2.2). Additionally, a large percentage of the inital excitation relaxes into a Frenkel exciton (FE, path 2 in Figure 2.2) which could dissociate under applied electric fields creating charge carriers contributing to the photocurrent at time scales of the exciton lifetime (path 2 in Fig. 2.2). In the D/A composite films, my group's previous work[79–81] suggests the existence of yet additional channel of charge carrier photogeneration due to dissociation of a CT exciton created by a Coulombically bound hole on the donor molecule and electron on the acceptor molecule (path 4 in Fig. 2.2). The efficiency of this channel depends on the properties of the CT state dictated by the offset of LUMO energies of the donor and acceptor and by the D/A separation at the D/A interface.[79] In both pristine ADT-TES-F films and D/A composites, there are also relaxation pathways that do not contribute to charge carrier photogeneration (path 3 in Fig. 2.2), such as tightly bound excitons recombining to the ground state with or without PL emission.

The dissociation rate of both exciton species (FE and CT) is modeled using the Onsager-Braun model discussed in Ch. 1.[26] My initial work used the equation presented in Braun's 1984 paper (Eq. 2.21), but for further research I switched to the form derived from first priniciples by Wojcik and Tachiya in 2009, which differs from Braun's original by a factor of 3 (i.e. $k_{diss,W-T} = k_{diss,O-B}/3$).[33] The extra factor of 3 in the orginal derivation arose because Braun did not properly consider the volume occupied by the electron before dissociation. Wojcik and Tachiya derive their form exactly from first principles, correcting Braun's error.[33] The transition to the corrected model is noted when it occurs in Ch. 3.

The current literature in the field continues to throw doubt on the physicality of the Onsager-Braun model, as discussed in Ch. 1. As a result, extracted values of initial pair separation are unlikely to be meaningful, and where possible the dissociation rate is reported instead of the initial pair separation.

2.3.1.1 Intensity Dependence

One of the current debates[48;53;82] in the organic semiconductor field is the nature of charge transport in organic films. In some models of carrier mobility,[51] an explicit carrier density dependence term is included. This is most common in, though not unique to, hopping transport models. Band-like models tend to predict little to no direct carrier density dependence.[53] Instead, all carrier density dependence of mobility is assumed to result from a combination of bimolecular and geminate recombination. Using my model and fitting experimental data taken with multiple incident laser intensities allows the testing of these different predictions. To accomplish this, I modified Eq. 2.24 to incorporate an explicit carrier density dependence term, and tested two sample models. The resulting equations are

$$\mu_{p(n)} = \mu_{p(n)}\left(T, E\right) * h_m\left(p(n), T\right) \tag{2.12}$$

$$h_1\left(p(n)\right) = 1 \tag{2.13}$$

$$h_2\left(p(n)\right) = exp\left(u_{p(n)}\left(\frac{2p(n)}{N_t}\right)^{\nu_{p(n)}}\right) \tag{2.14}$$

where $h_m\left(p(n)_f, T\right)$ is a carrier density dependence function which can also depend on temperature. The function h_1 (Eq. 2.13) assumes no carrier density dependence of mobility,

predicted in band-like models for the case of carrier concentrations of $10^{-4} - 10^{-6}$ carriers/site, similar to ours.[56] Therefore, the light intensity-dependent TPC dynamics simulated using h_1 would be due to carrier density-dependent recombination only. The function h_2 (Eq. 2.14) is a parametrization of numerical hopping conduction results derived by Coehoorn et al.,[51] which assumes a Gaussian DOS with width $\sigma_{p(n)}$ for hole(electron) conduction. N_t is the number of possible hopping sites (taken to be $10^{20} cm^{-3}$), $u_{p(n)} = (1/2)(\hat{s}^2_{p(n)} - \hat{s}_{p(n)})$, $\nu_{p(n)} = \left(\frac{2}{\hat{s}^2_{p(n)}}\right)\left(ln\left(\hat{s}^2_{p(n)} - \hat{s}_{p(n)}\right) - ln\left(ln\left(4\right)\right)\right)$, and $\hat{s}_{p(n)} = \sigma_{p(n)}/k_B T$. In this approach, charge carrier mobility is an increasing function of carrier concentration, which in our experiments is light intensity-dependent. Therefore, in this case the TPC incorporates intensity-dependent contributions of mobility and of the various mobility-dependent rates. The results of these simulations are reported in section 3.3.2.

2.3.2 Charge transport

The concentration of acceptor molecules in our D/A composites is sufficiently low for the acceptor domain formation to be neglected, so that an effective medium approach can be used, with charge carrier mobilities μ_n and μ_p representing the transport of electrons and holes, respectively, through the ADT-TES-F donor. The mobilities are modified by the presence of acceptor molecules. In keeping with my group's previous studies of temperature dependent photocurrents in ADT-TES-F films and their D/A composites, we consider a Poole-Frenkel electric field dependence for these mobilities.[81] Charge carrier trapping effects are incorporated in the model via trapping parameters B_p (B_n) for holes (electrons) and total available hole (electron) trap densities of N_p (N_n). In ADT-TES-F films, holes are the majority carrier

and are likely to encounter shallower traps than electrons. Thus, in modeling photocurrent dynamics at ns time scales, we only include a charge detrapping effect for holes. To describe charge trapping and detrapping processes, we use the Miller-Abrahams model,[83] giving the detrapping rate $B_{p_t} = \nu_0 \times exp[-\Delta/k_B T]$, where ν is the attempt-to-jump frequency, Δ is an average trap depth, T is the temperature (taken to be $300K$), and k_B is Boltzmann's constant. We further assume that for the trapping process considered in the Miller-Abrahams model, ν_0 is approximately equal to the product of the hole trapping parameter B_p and the hole trap density N_p. Also included in the model are bimolecular recombination with the Langevin rate γ and recombination of a free hole (electron) with a trapped electron (hole) with a rate $B_{p_f n_t}$ ($B_{n_f p_t}$).

2.3.3 Model

Given the considerations above, the resultant equations are as follows:

$$\frac{dn_f}{dt} = \xi_{SSC}(E)\,G(t) + k_{diss,FE}X_{FE} - \gamma n_f p_f - B_n(N_n - n_t)n_f - B_{n_f p_t} n_f p_t \quad (2.15)$$

$$[+k_{diss,CT}X_{CT}]$$

$$\frac{dn_t}{dt} = B_n(N_n - n_t)n_f - B_{p_f n_t} n_t p_f \quad (2.16)$$

$$\frac{dp_f}{dt} = \xi_{SSC}(E)\,G(t) + k_{diss,FE}X_{FE} + B_{p_t}p_t - \gamma n_f p_f - B_p(N_p - p_t)p_f - B_{p_f n_t} n_t p_f \quad (2.17)$$

$$[+k_{diss,CT}X_{CT}]$$

$$\frac{dp_t}{dt} = B_p(N_p - p_t)p_f - B_{n_f p_t} n_f p_t - B_{p_t} p_t \quad (2.18)$$

$$\frac{dX_{FE(CT)}}{dt} = \xi_{FE(CT)}(E)\,G(t) - k_{diss,FE(CT)}X_{FE(CT)} - k_{r,FE(CT)}X_{FE(CT)} \quad (2.19)$$

$$\gamma = e\left(\mu_n + \mu_p\right) / \left(\epsilon_0 \epsilon_r\right) \quad (2.20)$$

$$k_{diss,FE(CT)}(E,T) = \frac{3\gamma J_1\left(2\sqrt{-2b}\right)}{4\pi a^3_{FE(CT)}\sqrt{-2b}} exp\left(-\frac{E_{B,FE(CT)}}{k_B T}\right) \quad (2.21)$$

$$b = \left(e^3|E|\right) / \left(8\pi\epsilon_0\epsilon_r\left(k_B T\right)^2\right) \quad (2.22)$$

$$J = eE\left(\mu_n(E)\,n_f + \mu_p(E)\,p_f\right) \quad (2.23)$$

$$\mu_{n(p)}(E) = \mu_{n0(p0)} exp\left(\gamma_{n(p)}\sqrt{E}\right) h_m\left(p(n)_f, T\right) \quad (2.24)$$

Here, t is the time, e is the fundamental charge, ϵ_0 is the permittivity of free space, ϵ_r is the relative permittivity of the film (taken to be 3). Variables $p(n)_f$ correspond to the free hole (electron) density, $p(n)_t$ is the trapped hole (electron) density, and X_{FE} (X_{CT}) is the exciton density for the FE (CT exciton). J is the total current density, E is applied electric field, G is the photoexcitation rate described below in Eq. 2.26, and ξ_{SSC}, ξ_{FE}, and ξ_{CT} are fractions of the photoexcitation that result in charge photogeneration via the SSC pathway and via FE and CT exciton dissociation (pathways 1, 2, and 4, respectively, in Fig. 2.2). $k_{diss,FE}$ ($k_{diss,CT}$) are dissociation rates for the FE (CT exciton), and $k_{r,FE}$ ($k_{r,CT}$) are recombination rates for the FE (CT exciton). $E_{B,FE}$ ($E_{B,CT}$) is the binding energy of the FE (CT exciton) given by $E_{B,FE(CT)} = e^2/(4\pi\epsilon_0\epsilon_r a_{FE(CT)})$, where a_{FE} (a_{CT}) is the initial separation between charge carriers for the FE (CT exciton). Equations 2.15 and 2.17 are the coupled drift equations for hole and electron densities, with multiple charge generation paths as described above and bimolecular recombination of free carriers to the ground state with Langevin rate constant of Eq. 2.20. Following Hilczer & Tachiya and others,[72;84] bimolecular recombination leading to formation of the FE or CT exciton was also considered, but produced a negligible effect on the photocurrent dynamics and so was omitted. Equations 2.16 and 2.18 describe the trapping, trap assisted recombination, and hole detrapping of carriers, governed by their respective rates. Equation 2.19 describes the dynamics of the dissociation and recombination of FE and, in D/A composites, CT excitons. The dissociation rate of both FE and CT excitons is given by Eq. 2.21, following the Onsager-Braun formalism as discussed in Ch. 1.[26] $\mu_{p0}(\mu_{n0})$ and $\gamma_p(\gamma_n)$ are Poole-Frenkel model parameters characterizing zero-field mobility and electric field dependence of mobility for holes (electrons).

Commonly used models of exciton dissociation, including the Onsager-Braun model, con-

sider the rate of dissociation k_{diss} electric field dependent, whereas the primary yield of geminate pair formation (ξ_{FE}) is typically assumed to be electric field independent; this assumption has been challenged in several studies.[20;34;85] I found that our data is more consistent with an electric field-dependent competition among charge carrier photogeneration pathways 1, 2 and, in composites, 4, which suggests that ξ_{SSC}, ξ_{FE}, and ξ_{CT} are field dependent. Since the analytical function describing such competition is not known, in order to extract quantitative information about relative contributions of these different charge generation pathways to the photocurrent at various applied electric fields, I used the simplest possible linear model for the electric field dependence of these parameters, specifically

$$\xi_{SSC(FE)(CT)} = \xi^{(0)}_{SSC(FE)(CT)} + \gamma_{SSC(FE)(CT)} E \tag{2.25}$$

where the parameters $\xi^{(0)}_{SSC(FE)(CT)}$ and $\gamma_{SSC(FE)(CT)}$ were taken to be constant over our range of electric fields. I found that this assumption worked well for pristine ADT-TES-F and ADT-TES-F/Pn-TIPS-F8 films up to electric fields of at least 80 kV/cm; however, in ADT-TES-F/PCBM films, the assumption started to break down at about 60 kV/cm (see Section 3.4).

The illumination profile of my films on interdigitated electrodes is taken to be uniform over the device. I calculated the generation rate $G(t)$ by first assuming a perfect Gaussian laser pulse with a full width at half maximum (FWHM) of $\tau = 500\ ps$, representative of the laser pulse used in our experiments, and then multiplying it by the density of absorbed photons N_{ph}, which in my experiments varies between 2.9×10^{15} and $4.2 \times 10^{16}\ cm^{-3}$. In

particular,

$$G(t) = N_{ph}\frac{2\sqrt{ln2}}{\tau\sqrt{\pi}} * exp\left(-4\,ln2\frac{(t - t_{FWTM}/2)^2}{\tau^2}\right) \tag{2.26}$$

where t_{FWTM} is the full width at a tenth of the maximum of the Gaussian pulse and $G(t = 0) = 0.1G_{max}$, where G_{max} is the photon density at the laser pulse maximum. The constants ensure that the pulse is normalized such that $\int_{-\infty}^{\infty} G(t)\,dt = N_{ph}$. For computational purposes, the infinite integration limits were replaced by those that correspond to the duration of the simulated transient photocurrent, 0 to 20 ns.

Based on non-negligible dark currents in our films, due mostly to efficient hole injection from the Au electrodes,[13;77] there exists an initial density of free and trapped charge carriers that cannot be neglected.[86] To find an estimate for this initial density, I looked to the boundary conditions at the metal-organic interface I had used in drift-diffusion modeling. I use a solution of boundary conditions assuming thermionic injection with image charges originally developed by Scott and Malliaras[87] and extended by Lacic, et al.[88]. For $E > 0$, I can write the cathode and anode currents as[88]

$$J_n^{cathode} = B\mu_n\left(N_0 e^{-\phi_B^n/k_BT-\sqrt{F}} - n_c\left(\frac{1}{\Psi^2} - F\right)/4\right) \tag{2.27}$$

$$J_p^{cathode} = B\mu_p\left(P_0 e^{\left(-\phi_B^p + e|E|r_c/4\right)/k_BT} + p_c\right) \tag{2.28}$$

$$J_n^{anode} = B\mu_n\left(N_0 e^{\left(-\phi_B^n + e|E|r_c/4\right)/k_BT} + n_a\right) \tag{2.29}$$

$$J_p^{anode} = B\mu_n\left(P_0 e^{-\phi_B^p/k_BT-\sqrt{F}} - p_a\left(\frac{1}{\Psi^2} - F\right)/4\right) \tag{2.30}$$

where $J_{p(n)}$ is the hole (electron) current, $P_0(N_0)$ is the density of chargeable sites for

holes(electrons), $\phi_B^{p(n)}$ is the injection barrier for holes(electrons), $F = \frac{eEr_c}{k_BT}$ is the reduced electric field, r_c is the Coulomb capture radius given by $r_c = e^2/(4\pi\epsilon_0\epsilon k_BT)$, $p(n)_c$ and $p(n)_a$ are the hole(electron) densities at the cathode and anode, respectively, and $\psi = F^{-1} + F^{-1/2} - F^{-1}\sqrt{1+2\sqrt{F}}$.

At steady state in the dark, detailed balance requires that $J_{cathode} = J_{anode}$. This enables solving Eqs. 2.27–2.30 for N_0 and P_0, giving for N_0

$$N_0 exp\left(-\frac{\phi_B^n}{k_BT} + \sqrt{F}\right) - n_c\left(\psi^{-2} - F\right)/4 - n_a = -N_0 exp\left(-\frac{\phi_B^n}{k_BT} - |F|/4\right)$$
$$\Rightarrow N_0\left[exp\left(-\frac{\phi_B^n}{k_BT} + \sqrt{F}\right) + exp\left(-\frac{\phi_B^n}{k_BT} - |F|/4\right)\right] = n_a + n_c\left(\psi^{-2} - F\right)/4$$

with the P_0 equation similar. Next, assuming that $n_a \approx 0$ and $p_c \approx 0$,[89] and solving for $n_c \equiv n_f^0$ and $p_a \equiv p_f^0$, I obtain

$$n_f^0 = N_0\, exp\left(-\frac{\phi_B^n}{k_BT}\right)\frac{B}{A} \tag{2.31}$$

$$p_f^0 = P_0\, exp\left(-\frac{\phi_B^p}{k_BT}\right)\frac{B}{A} \tag{2.32}$$

where B and A are constants that depend only on F and ψ. I now assume that the density of chargeable sites for electrons and holes is identical, giving $N_0 = P_0 \equiv N$.[90] Plugging these results into Eq. 2.23 with $J = J_{Dark}$, the measured dark current density at the applied

electric field E, we have

$$\begin{aligned}
J_{Dark} =& eE\left(\mu_n n_f^0 + \mu_p p_f^0\right) \\
\Rightarrow J_{Dark} =& eEN\frac{B}{A}\left(\mu_n e^{-\frac{\phi_B^n}{k_B T}} + \mu_p e^{-\frac{\phi_B^p}{k_B T}}\right) \\
\Rightarrow N =& \frac{J_{Dark}}{eE}\frac{A}{B}\left(\mu_n e^{-\frac{\phi_B^n}{k_B T}} + \mu_p e^{-\frac{\phi_B^p}{k_B T}}\right)^{-1} \\
\Rightarrow \frac{A}{B} n_f^0\ exp\left(\frac{\phi_B^n}{k_B T}\right) =& \frac{J_{Dark}}{eE}\frac{A}{B}\left(\mu_n e^{-\frac{\phi_B^n}{k_B T}} + \mu_p e^{-\frac{\phi_B^p}{k_B T}}\right)^{-1} \\
\Rightarrow n_f^0 =& \frac{J_{Dark}}{eE}\frac{e^{-\frac{\phi_B^n}{k_B T}}}{\mu_n e^{-\frac{\phi_B^n}{k_B T}} + \mu_p e^{-\frac{\phi_B^p}{k_B T}}} \\
p_f^0 =& \frac{J_{Dark}}{eE}\frac{e^{-\frac{\phi_B^p}{k_B T}}}{\mu_n e^{-\frac{\phi_B^n}{k_B T}} + \mu_p e^{-\frac{\phi_B^p}{k_B T}}}
\end{aligned}$$

Note that the same expressions are obtained for any relationship $n_c = f(n_a)$, so long as the symmetry $p_a = f(p_c)$ also holds. The remainder of the initial densities can be calculated from the rate equations 2.16 & 2.18 above by setting dn_t/dt and dp_t/dt to 0. Our initial conditions are thus

$$n_f^0 = \frac{J_{Dark}(E)}{eE}\frac{e^{-\frac{\phi_B^n}{k_B T}}}{\mu_n e^{-\frac{\phi_b^n}{k_B T}} + \mu_p e^{-\frac{\phi_B^p}{k_B T}}} \tag{2.33}$$

$$p_f^0 = \frac{J_{Dark}(E)}{eE}\frac{e^{-\frac{\phi_B^p}{k_B T}}}{\mu_n e^{-\frac{\phi_b^n}{k_B T}} + \mu_p e^{-\frac{\phi_B^p}{k_B T}}} \tag{2.34}$$

$$n_t^0 = \left(B_n N_n n_f^0\right) / \left(B_n n_f^0 + B_{p_f n_t} p_f^0\right) \tag{2.35}$$

$$p_t^0 = \left(B_p N_p p_f^0\right) / \left(B_p p_f^0 + B_{n_f p_t} n_f^0 + B_{p_t}\right) \tag{2.36}$$

Parameter (u)	ADT-TES-F	2% Pn-TIPS-F8	2% PCBM
$\mu_{n,0}\ \left(cm^2\,(Vs)^{-1}\right)\ (\pm.07)$	0.093	0.016	0.025
$\mu_{p,0}\ \left(cm^2\,(Vs)^{-1}\right)\ (\pm.05)$	0.60	0.51	0.36
$\gamma_n\ (cm/V)^{1/2}\ (\pm 0.5\times10^{-4})$	1.8×10^{-3}	2.0×10^{-3}	3.8×10^{-3}
$\gamma_p\ (cm/V)^{1/2}\ (\pm 0.5\times10^{-4})$	3.1×10^{-4}	6.0×10^{-4}	9.1×10^{-4}
$\Delta\ (meV)\ (\pm3)$	29	41	39
$N_n\ (cm^{-3})\ (\pm 0.5\times10^{18})$	7.1×10^{18}	7.4×10^{18}	8.7×10^{19}
$N_p\ (cm^{-3})\ (\pm 0.5\times10^{18})$	2.8×10^{18}	2.2×10^{18}	3.8×10^{18}
$B_nN_n\ (s^{-1})\ (\pm 1\times10^{11})$	5.1×10^{11}	8.9×10^{11}	7.8×10^{11}
$B_pN_p\ (s^{-1})\ (\pm 3\times10^{10})$	3.9×10^{10}	6.9×10^{10}	2.1×10^{11}
$B_{n_fp_t}\ (cm^3s^{-1})\ (\pm 5\times10^{-4})$	1.4×10^{-3}	5.0×10^{-3}	4.0×10^{-3}
$B_{p_fn_t}\ (cm^3s^{-1})\ (\pm 3\times10^{-7})$	2.1×10^{-5}	2.7×10^{-5}	8.2×10^{-7}
$a_{FE}\ (nm)\ (\pm.02)$	1.18	1.18	1.18
$a_{CT}\ (nm)\ (\pm.02)$	-	1.22	1.77

Table 2.1: Parameter values extracted from experimental data for pristine ADT-TES-F drop cast films and ADT-TES-F-based D/A drop cast composite films with Pn-TIPS-F8 and PCBM acceptors using simulation of the system Eqs. 2.15–2.26. Parameter descriptions are given in the text. Listed uncertainties indicate the range of values found in different individual devices.

The injection barriers for holes(ϕ_B^p) and electrons(ϕ_B^n) were taken to be 0.25 eV and 2.05 eV, respectively, calculated from the HOMO and LUMO levels of ADT-TES-F and the work function of Au (5.1 eV).

The system of Eqs. 2.15–2.26 with initial conditions given by Eqs. 2.33–2.36 was solved numerically in MATLAB using the built in ode15s function to generate a simulated transient photocurrent measurement. A full code sample is available in Appendix A.2 & A.3.

2.3.4 Nonlinear Optimization

The simulated transients were then fit to the data using the non-linear optimization package NLOPT.[91] The NLOPT package minimizes an arbitrary objective (or "cost") function using a user-selected algorithm. The two objective functions used in this work are

$$f_1(\vec{x}) = \sum_n \left(J_{Data}(t_n) - J_{Sim}(t_n, \vec{x})\right)^2 \tag{2.37}$$

$$f_2(\vec{x}) = \sum_m (1 - r_m^2) \tag{2.38}$$

where $\vec{x}$ is the vector input to the simulation function that incorporates all parameters varied in the model, t_n is the nth discrete time value, $J_{Data}(t_n)$ is the experimentally measured total current at t_n, $J_{Sim}(t_n, \vec{x})$ is the simulated total current at t_n, and $r_m^2 = 1 - \frac{\sum_i \left(J_{Data} - J_{Data,Avg}\right)^2}{\sum_i (J_{Sim} - J_{Data})^2}$ is the coefficient of determination of the simulated fit for the mth transient. Eq 2.37 was used for fitting single transients, Eq. 2.38 for fitting multiple transients at once. The coefficient of determination provides a good, normalized measure of error, allowing the comparison of multiple transients without weighting towards higher valued transients. Two algorithms were used for the fitting. The ISRES[92] algorithm was used for gross global fitting across a large initial parameter space, and the COBYLA[93] algorithm was used to perform fine local minimization. Using these objective functions, we obtained sets of parameters that describe the experimentally measured photocurrent transients at all applied electric fields in the studied range.

In order to ensure that the fit results are physically reasonable, we need appropriate constraints. The NLOPT package allows for the inclusion not only of upper and lower bounds

on each input parameter ("linear bounds"), but also of bounds which relate multiple input parameters ("non-linear bounds"). Some parameters have been well studied, and bounds can be chosen based on a range of reported values. Other parameters required more iteration and broader ranges. In addition to the bound constraints, several nonlinear constraint functions were used. The bounds reported here are the largest bounds used; part of the iteration process was to adjust the bound constraints to improve running time and accuracy.

The highest reported hole mobility for ADT-TES-F was 6 $cm^2/(Vs)$ in crystals[94] and around 1.5 $cm^2/(Vs)$ in thin-film transistors on PFBT-treated electrodes.[4] In drop cast films on untreated Au electrodes, mobilities are lower,[13] which prompted us to set an upper limit for hole mobility of 1 $cm^2/(Vs)$ and use initial bounds of [0.1, 1] $cm^2/(Vs)$. For films spun cast on PFBT treated electrodes, the upper limit for hole mobility was set at 1.5 $cm^2/(Vs)$, leading to bounds of [0.5, 1.5]. For single crystals, I chose an upper limit of 4 $cm^2/(VS)$, with bounds of [1, 4]. Electron mobility in these materials is not known; based on the theoretical estimates,[95] we set electron mobility bounds to [0.01, 0.3] $cm^2/(Vs)$ for drop cast samples and [0.1, 0.6] $cm^2/(Vs)$ for spin cast and single crystal samples.

For trapping, detrapping, and trap-assisted recombination rates, initial values were taken from Soci, et al.[76] The trapping rates B_p and B_n were constrained in [10^{-5}, 10^{-9}] cm^3s^{-1}. Detrapping rate was fit by varying Δ, bounded by [10, 100] meV. Trap assisted recombination rates $B_{p_f n_t}$ and $B_{n_f p_t}$ were bound by [5×10^{-3}, 1×10^{-7}] cm^3s^{-1}. Initial values for the trap density bounds were taken from studies performed on pentacene and ADT transistors.[65] Initial bounds were [10^{16}, 10^{21}] cm^{-3}, but repeated testing indicated that better bounds were [10^{16},10^{19}] cm^{-3}.

The charge generation term bounds initially used were [0, 0.3] for $\xi_{SSC,0}$, [0.1, 0.8] for

$\xi_{FE,0}$, and [0.1, 0.8] for $\xi_{CT,0}$. Results of the single electric field fitting resulted in shifting the range of $\xi_{SSC,0}$ to [-0.03, 0.1] for the drop cast pristine ADT-TES-F film only. The electric field dependence terms $\gamma_{SSC(FE)(CT)}$, when used, were constrained in $[25 \times 10^{-6}, 125 \times 10^{-4}]$ cm/kV. Initial pair separation was based on previous work with organic Frenkel excitons,[73] and constrained by [0.5, 2] nm for both the FE and CT exciton. The recombination rate was kept in the bounds of $[5 \times 10^5, 5 \times 10^9]$ s^{-1}.

I used nonlinear bounds to ensure that the optimal input array would not be clearly nonphysical. Trapping times described by $(N_n \times B_n)^{-1}$ and $(N_p \times B_p)^{-1}$ were constrained between [1, 200] ns. Photoexcitation distribution was constrained by $\xi_{SSC} + \xi_{FE} + \xi_{CT} < 1$. We required $\mu_n < \mu_p$, and fits which had very close values of μ_n and μ_p were discarded and rerun. Fits with excessively small values (<0.01) of η_{FE} or η_{CT} were also sometimes discarded and rerun, depending on the sample being tested. CT exciton lifetimes, calculated by $\tau_{CT} = (k_{d,CT} * k_{R,CT})^{-1}$, were required to be in [1, 5] ns for samples with no known exciplex lifetime. In samples with known exciplex lifetimes, τ_{CT} was also constrained to be within 2 ns of the exciplex lifetime, with a hard lower bound of 1 ns.

2.3.5 Computation Development

I will now describe several landmarks in the development of my codebase. My first efforts were targeted at solving the full space-dependent drift-diffusion model, which required building a PDE solver. I implemented an algorithm for solving of this type of PDE derived by Scharfetter and Gummel.[96] Initial densities and carrier generation were set to 0, then the model was run until the current output stabilized, at which point the generation term was applied.

This ensured that the initial densities were realistic. I set my input and device parameters to that reported in a paper from Hwang, et. al.[73] in order to verify the model was working properly. My completed, functional model produced transients which closely matched those reported in my comparison paper, and simulations would take a few seconds to complete. When I scaled up the device parameters from Hwang's $\sim$ 200 nm devices to our 25 μm devices, I found that the running time increased significantly as well, with a single simulation taking anywhere from 2 to 4 hours to complete. Given that the goal of the project was to fit simulated transients to data, I knew that this process took much too long to work. I determined through algorithmic analysis that the time the project was taking was inherent to the number of loops required to perform the simulation, meaning that tweaking the algorithm would not significantly reduce the running time.

At this point I turned to implementing the much simpler spatially averaged drift-only model, using the work I had already done and Matlab's built in ode solvers to create the simulation. One consideration in the accuracy of the final model was the size of the values used in the model. Matlab's built in float data type was not accurate enough to handle the very small densities and time steps used in my program. As a result, I needed to scale the variables, rewriting the system in units which would provide numbers large enough that rounding/truncation error would not negatively affect the results of the program. I used the

following scaling references and derived terms:[97]

$$(m^{-3})\ N_0 = J_{Dark}/\left(e * E * (mu_N + mu_P * exp\left(\frac{\phi_B^p - \phi_B^n}{k_B T}\right)\right) \tag{2.39}$$

$$(V)\ V_{kt} = \frac{k_B * T}{e} \tag{2.40}$$

$$(cm^2/Vs)\ D_s = 1e-4 \tag{2.41}$$

where N_0 is the initial hole density (m^3), V_{kt} is the thermal voltage (V), and D_s is a diffusion constant (m^2/Vs). These were used to derive the following scaling terms

$$(m)\ L_d = \sqrt{\frac{\epsilon_0 \epsilon_R k_B T}{e^2 N_0}} \tag{2.42}$$

$$(A/m)\ J_0 = \frac{e D_s N_0}{L_d} \tag{2.43}$$

$$(V/m)\ E_s = \frac{V_{kt}}{L_d} \tag{2.44}$$

$$(s)\ t_0 = \frac{L_d^2}{D_s} \tag{2.45}$$

$$(m^{-3}/s)\ U_0 = \frac{D_s N_0}{L_d^2} \tag{2.46}$$

The various input parameters into Eqs. 2.15–2.26 & 2.33–2.36 are then scaled to be unitless. There is a complication with this scheme in the calculation of the Langevin recombination rate (Eq. 2.20). When used in Eqs. 2.15 & 2.17, γ needs to be multiplied by the scaling constant $N_0 t_0$, but when used in Eq. 2.21, it should have a scaling constant of $(L_d D_s)^{-1}$. As a result, γ has two different scaled forms in the code.

With this scaling implemented, the model was ready to be fit to transients. To do this, I turned my script into a function which took an input array and output a cost function value.

Doing this allowed that function to be passed to NLOPT, which could find an optimum input array given a starting array and a set of linear and nonlinear bounds.

Chapter 3: Photocurrent Transient Simulations

This chapter presents the results of the central work of this thesis, starting with how the computational model was validated.

3.1 Validation Testing

With such a complicated model and so many input parameters, it was important to assess the effect of each parameter on the resulting simulated transients. It is also important to the iterative fitting process to be able to test parameter bounds easily. To perform these tests, I wrote a variation of the transient function which iterates through each input parameter, running a set of simulations holding all inputs except one constant. It also allows for testing experimentally determined parameters such as laser power and injection barrier. The specific multiples which are tested can be set by the user, as can the specific set of input parameters tested in each run. Some sample graphs output by this script can be found in Figure 3.1.

The graphs of the charge generation and mobility terms show that the initial rise of the photocurrent is determined almost entirely by the hole mobility and the SSC generation term. The initial fall is strongly affected by the trapping terms and the FE and CT generation terms, while the level of the final slow decay is largely determined by trap assisted recombination, detrapping, and mobility. The transition between the fast and slow current decay (i.e. the "elbow") is the most complicated piece of the transient, with most parame-

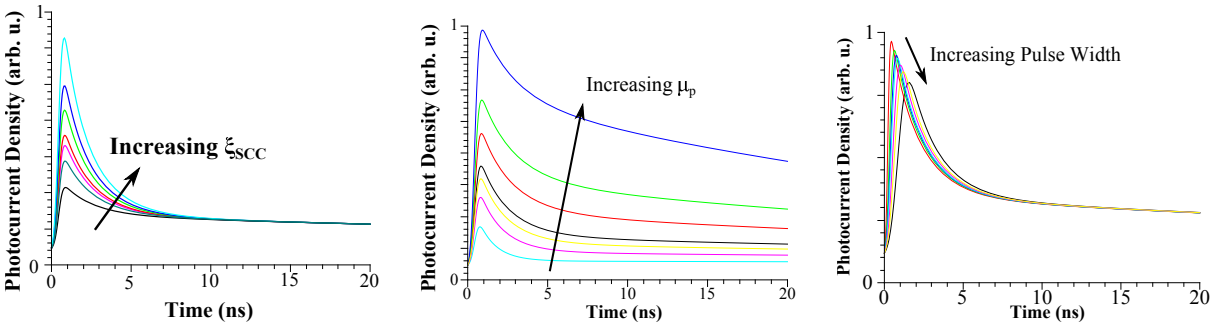

(a) SSC generation efficiency (b) Hole mobility (c) Excitation pulse width

Figure 3.1: Effects of varying select input parameters on resulting simulations

ters contributing to its exact shape. The terms that relate directly to electrons tend to cause smaller (but still important) variation than the hole terms, due to the hole carrier densities being several orders of magnitude higher than the electron carrier densities. As the incident laser intensity increases, the initial peak becomes sharper due to an increase in the effect of bimolecular recombination, a second order effect based on both the hole and the electron free carrier densities. Modifying the width of the excitation pulse shifts the initial rise and peak photocurrent later in time. Changing the injection barriers affects the initial hole and electron densities, changing the magnitude of the photocurrent and the height of the initial peak in a similar manner to the dependence shown in Figure 2.1.

3.2 Experimental Details

3.2.1 Materials & Sample Preparation

Measurements were performed on donor-only, acceptor-only, and donor-acceptor(D/A) bulk heterojuction (BHJ) films and crystals. A summary of the materials used and a sample of

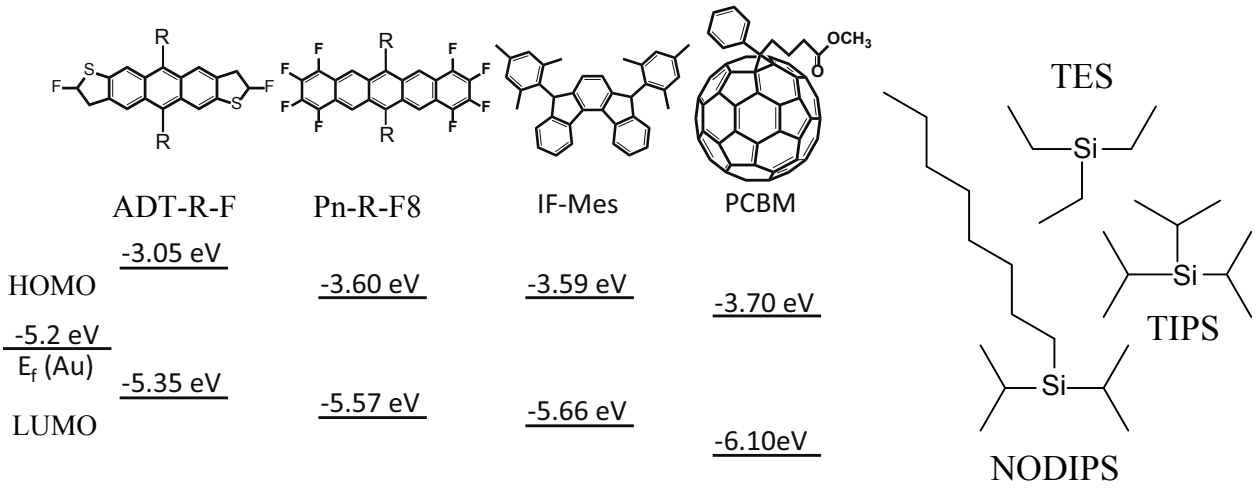

Figure 3.2: Examples of the materials used in this study with their HOMO and LUMO levels. On the right are samples of the R groups studied.

their HOMO and LUMO levels can be found in Figure 3.2. The primary donor material was the fluorinated anthradithiophene derivative ADT-TES-F. A wide variety of acceptors were used, falling into a few categories: A) Fluorinated pentacene derivates (Pn-R-F8), B) the C_{60} buckyball derivative PCBM (Phenyl-C_{61}-butyric acid methyl ester), and C) an indenofluorine derivate IF-MES. Molecular structures of several of the R groups used with the ADT and Pn backbones are also shown in Figure 3.2. The primary electronic structure of a material is determined by the backbone, leading to nearly identical solution fluorescence and absorption spectra. The solid state packing, on the other hand, is largely determined by the specific choice of R group. This allows us to isolate the effects of packing and electronic structure on acceptor performance.

Three types of samples: drop cast films, spin cast films, and single crystals. For optical measurements, samples were deposited on standard glass cover slips. For electronic measurements, samples were deposited on glass substrates patterned with interdigitated Cr/Au (5

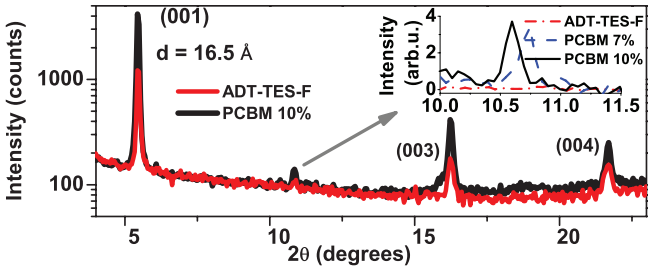

Figure 3.3: XRD results for out-of-plane structures in pristine ADT-TES-F and ADT-TES-F/PCBM 10 wt% spin cast films. Inset shows a magnified view of the peak due to PCBM crystallization in D/A films with 7 wt% and 10 wt% of PCBM. Data from a pristine ADT-TES-F film in the same 2θ region are also included.
.

nm/ 50 nm) electrode pairs with a $L = 25\ \mu m$ gap between the electrodes.[79] Each electrode set consisted of 10 pairs of 1 mm long and 25 μm wide fingers. For drop cast films, substrates were placed on a hot plate set to $\sim 65°C$ and drops of $\sim 10\mu L$ were slowly dispensed using a micropipette. Films were spin cast at between 1000 and 3000 rpm for 30 seconds from 30 mM solutions in chlorobenzene onto substrates that had been treated with pentafluorobenzenethiol (PFBT). The PFBT treatment consisted of soaking substrates in a 30 mM ethanol solution for 30 minutes, followed by a 5 minute sonication and rinse in ethanol. This process creates a single molecular layer of PFBT, which has been shown to improve film crystallinity and enhance hole mobility in ADT-TES-F TFTs.[98;99] Single crystals were grown from a 30 mM chlorobenzene solution onto substrates treated with PFBT as described above.

Both film deposition methods produced polycrystaline films, confirmed by XRD (Figure 3.3).[79] Spin cast films displayed larger crystals and more prominent XRD peaks than drop cast films.[15] Crystalization was also strongly affected by the acceptor molecule and concentration in D/A blends.[15]

3.2.2 Optical Measurements

The laser sources used in this study were numerous and are listed here along with the terms used to reference them in the rest of this work: a 532 nm (2.33 eV), continuous wave, frequency-doubled $Nd:YVO_4$ from Coherent, Inc (Verdi), a 633 nm (1.96 eV), continuous wave, He:Ne gas laser from Melles Griot (He:Ne), a Ti:Saph oscillator pumped with the Verdi, which can output $\sim$ 100 fs pulses with a $\sim$ 90 MHz rep rate at 800nm (1.55 eV) which can be frequency doubled using a BBO crystal to 400 nm (3.10 eV) (Ti:Saph), a 355 nm (3.49 eV), 0.18 $\mu J/cm^2$, 500 ps, 44.6 kHz pulsed, cavity Q-switched, frequency-tripled, Nd:YAG laser, from Nanolase, Inc (Nd:YAG), and a 532 nm, 470 ps, 50 kHz pulsed solid state laser from Altechna with a maximum fluence of $10\mu J/cm^2$ (Altechna). Optical fluorescence and absorption spectra were taken using an Ocean Optics USB4000 or USB2000FLG spectrometer. Absoption spectra used an Ocean Optics LS-1 tungsten halogen lamp, while photoluminescence (PL) was excited using one of the previously described lasers.

Fluorescence lifetimes presented in this work were derived from transient photoluminescence (TPL) curves measured using a technique known as "time correlated single photon counting" or TCSPC. An electronic timer (in our case, a PicoQuant TimeHarp 200 board) is connected to a pulsed laser trigger. The laser then illuminates the sample with a very short pulse of light, and the resulting fluorescence is collected and sent into an avalanche photodetector (APD) capable of detecting single photons. When the APD detects a photon, it sends a signal to the TCSPC board, which starts a highly accurate timer. The timer is stopped when the next laser trigger pulse is detected, and the resulting time is processed to produce the time elapsed since the laser pulse excited the sample. This technique allows for

accurate measurement of the fluorescence lifetime even with very low fluorescence intensities and very high laser repetition rates. All three of the pulsed lasers (Ti:Saph, Nd:YAG, and Altechna) were used in TPL measurements.

3.2.3 Electronic Measurements

Voltage was applied to the samples and dark current was measured as a function of voltage using a Keithley 237 source-measure unit. The average applied electric field E was calculated as $E = V/L$, and the studied range of electric fields was $20 - 80\ kV/cm$. A schematic of the transient photocurrent (TPC) measurements is shown in Figure 3.4. The samples were excited with either the Nd:YAG or the Altechna laser. The TPC was measured using a 50 GHz digital sampling oscilloscope (CSA8200/Tek80E01) from Tektronics, sometimes with a broadband amplifier (Centellax UAOL65VM). The time resolution of the system was about 0.6 ns, limited by the laser pulse width and jitter. For comparison with simulated currents, both dark current and transient photocurrent values were converted to volume current densities, assuming an active transport channel depth of $d = 1\ \mu m$ for drop cast films, $d = 200$ nm for spin cast films, and $d = 500$ nm for single crysals, based on the average thicknesses of our films and crystals.

3.3 Pristine ADT-TES-F films

To fit TPC in pristine ADT-TES-F films, we first considered a model which included only the fast SSC generation, pathway 1 in Figure 2.2 (i.e. $\xi_{FE} = 0$). An example of the best fit result

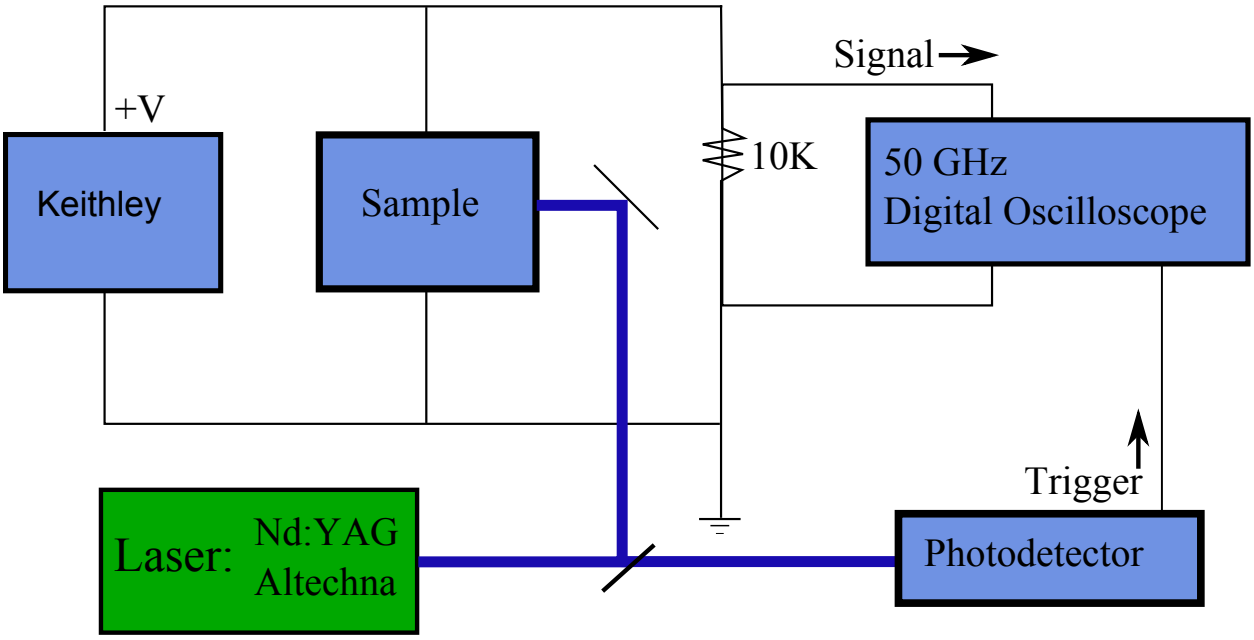

Figure 3.4: A schematic of the transient photocurrent experiment.

for the data taken at an applied electric field of 60 kV/cm is shown as the dashed line in the inset of Figure 3.11A. The simulated transient exhibited a fast rise followed by a considerably faster initial decay than the experimental data, with no additional slow decay component. Although this model could reproduce the fast rise and initial decay at higher applied electric fields (above $60kV/cm$), it was unable to attain good fits for the data obtained at lower applied electric fields or at times longer than $\sim$ 10 ns.

The next model examined was a model that only included the charge generation pathway via FE dissociation, pathway 2 in Figure 2.2 ($\xi_{SSC} = 0$ in Eqs. 2.15 and 2.17). A sample of the best fit attained in this case for the data taken at an applied electric field of 60 kV/cm is shown in the inset to Figure 3.11A as the dash-dotted line. The fits revealed that the FE dissociation-only model showed a much slower photocurrent rise than the data and did

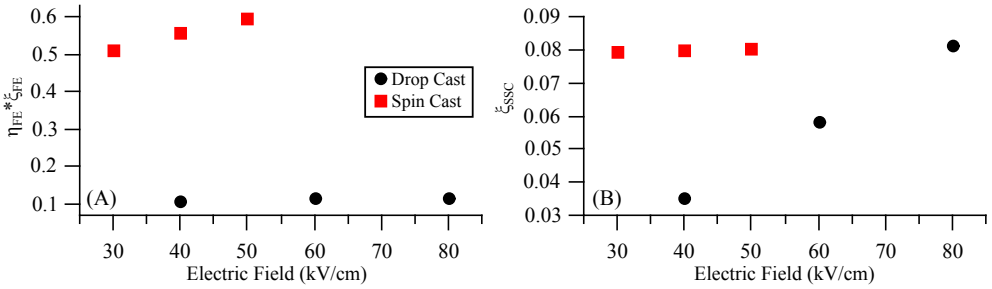

Figure 3.5: A comparison of the (A) FE charge generation pathway efficiency and (B) SSC charge generation pathway efficiency in spin cast and drop cast ADT-TES-F films.

not reproduce well the transition between the fast initial decay and slow decay component occurring at about 2-3 ns. This model was capable of generating better fits at lower electric fields, but the goodness-of-fit (r^2) values of such fits were still relatively low, below 0.8.

Next, I combined the fast SSC generation (pathway 1) and charge generation via FE dissociation (pathway 2) into one model. The results are presented in Figure 3.11A, with the short time-scale dynamics shown in more detail in the inset. The combined model displays the best aspects of SSC-only and FE dissociation-only models, with a fast photocurrent rise, a moderately fast initial decay, and a slow decay component. This model provided consistent results for the data across the entire range of applied electric fields and attained goodness-of-fit values r^2 of 0.89-0.97 depending on the electric field.

3.3.1 Voltage Dependence

Having found a model that could fit data at any single value of the applied electric field well, I generalized the fitting algorithm to fit data taken at all values of applied electric field simultaneously. In order to weight data for all of the different applied electric fields

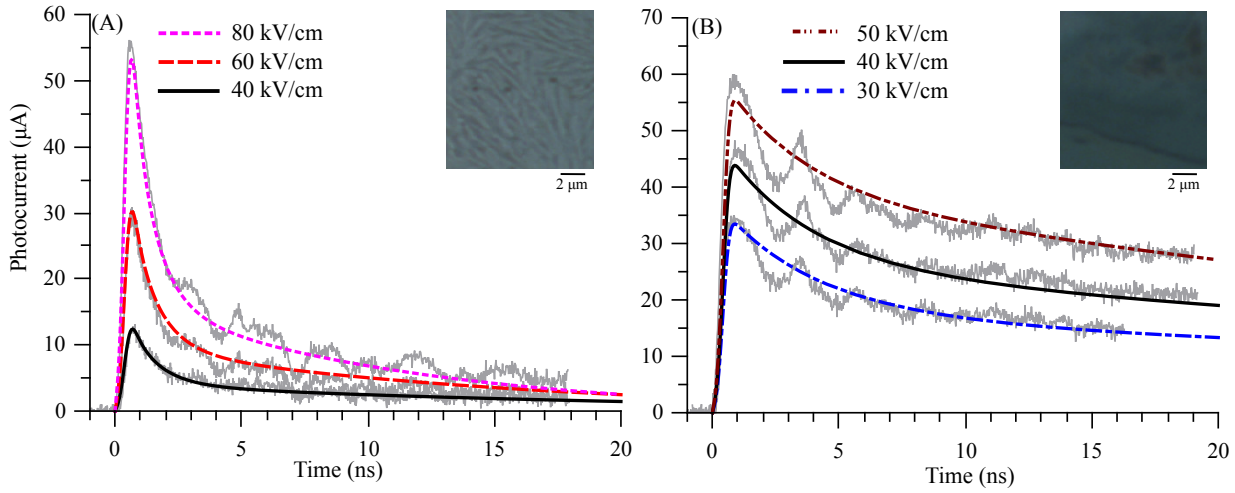

Figure 3.6: Experimental and simulated photocurrents from (A) drop cast and (B) spin cast ADT-TES-F films at varied electric fields. Insets show optical images of drop cast and spin cast films used in our experiments at 50x magnification.

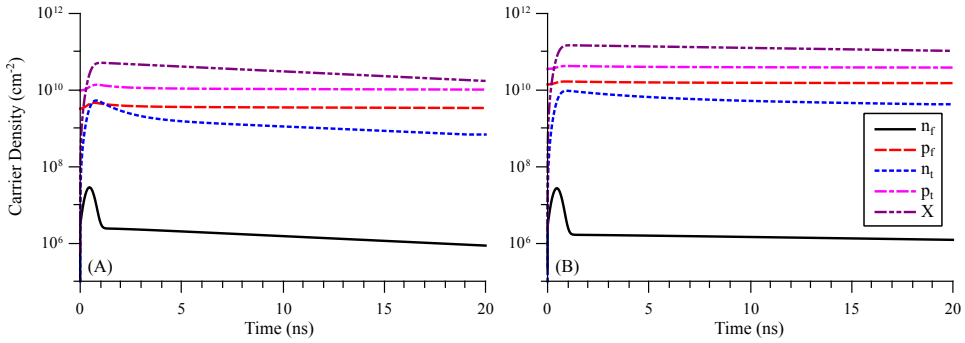

Figure 3.7: Simulated time evolution of densities of Frenkel exciton (X), free (p_f) and trapped (p_t) holes, and free (n_f) and trapped (n_t) electrons for a drop cast film (A) and a spin cast film (B) at 40 kV/cm.

identically, I used Eq.2.38 as the objective function. I simulated both drop cast and spin cast pristine films, to explore the differences in parameters which determine the optoelectronic properties.

First, I present the results of the drop cast film simulation. The fractions of absorbed photon density that resulted in the SSC (ξ_{SSC}) and in the formation of the FE state (ξ_{FE}), as revealed by simulations (Figure 3.6), are shown in Figure 3.5, at various applied electric fields. As the electric field increased from 40 kV/cm to 80 kV/cm, ξ_{SSC} increased from 0.035 to 0.081, whereas ξ_{FE} decreased from $\sim$ 0.2 to 0.15. Good fits were obtained by applying the constraint $\gamma_{SSC} = -\gamma_{FE}$ to Eq. 2.25, suggesting that the pathways 1 and 2 are in direct competition with each other, originating from the same photoexcited state. Possibilities for the nature of this state were explored in Ch. 1. The FE dissociates with the electric field-dependent dissociation rate $k_{diss,FE}$ (Figure 3.12E) during its lifetime given by $1/(k_{diss,FE} + k_{r,FE})$ (Figures 3.12D). The efficiency of the exciton dissociation occurring over time scales of the exciton lifetime is given by

$$\eta_{FE(CT)} = \frac{k_{diss,FE(CT)}}{k_{diss,FE(CT)} + k_{r,FE(CT)}}. \tag{3.1}$$

For the FE in pristine drop cast ADT-TES-F films, η_{FE} varies between 0.56 and 0.77 in the studied range of electric fields. This yields the fraction of absorbed photon density which contributes to the photocurrent via the FE dissociation, $\xi_{FE}\eta_{FE}$, of $\sim 0.11 - 0.12$, approximately same for all electric fields. The total efficiency of charge photogeneration, combined

from pathways 1 and 2, on the time scales of the simulated transients of $\sim 20\ ns$, is

$$\eta_{tot} = \xi_{SSC} + \xi_{FE}\eta_{FE}. \tag{3.2}$$

It increases from 0.14 to 0.20 upon an increase in the electric field from 40 kV/cm to 80 kV/cm, as shown in Figure 3.12C. The rest of the photoexcitation, given by $1 - \eta_{tot}$, which amounts to about $80-86\%$ of the absorbed photon density, depending on the applied electric field, does not contribute to charge carrier photogeneration in the time domain studied.

Table 3.1 lists values obtained from fits to experimental data for other parameters of Eqs. 2.15–2.26. Hole mobility, exhibiting a zero-field value of $\sim 0.6\ cm^2/(Vs)$, is consistent with TFT and space-charge-limited current mobilities in similar films.[13;99] Hole trapping and detrapping properties seem to be well described by the Miller-Abrahams model, with the attempt-to-jump rate ν of $3.9 \times 10^{10}\ s^{-1}$, comparable to that in pentacene films,[65] and the average trap depth of 29 meV similar to that of 25 meV obtained from Arrhenius fits of experimentally measured temperature dependence of the transient photocurrent in ADT-TES-F films in a previous paper[81] from my group. The zero-field electron mobility was lower than the hole mobility[95] by a factor of ~ 6, whereas the average electron trap density was higher than the hole trap density by a factor of ~ 2.5 (Table 2.1). Both hole and electron trap densities were on the order of $10^{18}\ cm^{-3}$, similar to values reported by other groups[90] for small-molecule organic semiconductor films.

With the multi-voltage process tested on drop cast films, I now turned to a spin cast film. The simulated photocurrents obtained for the drop and spin cast samples using the parameter values reported in Table 3.1 are presented in Figure 3.6. Time evolution of exciton

Parameter (u)	Drop cast	Spin cast	Single Crystal
$\mu_{n,0}\ \left(cm^2\,(Vs)^{-1}\right)\ (\pm.07)$	0.093	0.12	0.7
$\mu_{p,0}\ \left(cm^2\,(Vs)^{-1}\right)\ (\pm.05)$	0.60	1.2	2.0
$\gamma_n\ (cm/V)^{1/2}\ (\pm 0.5\times10^{-4})$	1.8×10^{-3}	2.8×10^{-4}	-
$\gamma_p\ (cm/V)^{1/2}\ (\pm 0.5\times10^{-4}, 10^{-6})$	3.1×10^{-4}	5.4×10^{-6}	-
$\Delta\ (meV)\ (\pm3)$	29	24	20
$N_n\ (cm^{-3})\ (\pm 0.5\times10^{18})$	7.1×10^{18}	4.8×10^{18}	3.2×10^{18}
$N_p\ (cm^{-3})\ (\pm 0.2\times10^{18})$	2.8×10^{18}	4.9×10^{17}	2.7×10^{18}
$B_nN_n\ (s^{-1})\ (\pm 1\times10^{11})$	5.1×10^{11}	7.5×10^{11}	2.6×10^{11}
$B_pN_p\ (s^{-1})\ (\pm 3\times10^{10})$	3.9×10^{10}	6.5×10^{10}	9.5×10^{11}
$B_{n_fp_t}\ (cm^3s^{-1})\ (\pm 5\times10^{-4})$	1.4×10^{-3}	1.8×10^{-4}	4.8×10^{-3}
$B_{p_fn_t}\ (cm^3s^{-1})\ (\pm 3\times10^{-7})$	2.1×10^{-5}	3.1×10^{-7}	1.6×10^{-7}
$k_R\ (s^{-1})\ (\pm 2\times10^{6})$	2.6×10^{7}	5.3×10^{6}	7.6×10^{7}

Table 3.1: Parameter values extracted from experimental data for ADT-TES-F devices prepared in various ways, using a simulation with a system of Eqs.(2.15-2.26). Parameter descriptions are given in the text. Listed uncertainties indicate the range of values found in different individual devices.

and charge carrier densities in these samples that resulted in the photocurrent transients in Figure 3.6 at an applied electric field of 40 kV/cm is shown in Figure 3.7. The spin cast film exhibited higher photocurrent values as compared to those in drop cast films at a given applied electric field despite a considerably lower film thickness (and thus, reduced optical absorption and cross-section of the current flow). We thus expect to see significantly higher charge photogeneration efficiency and hole mobility in the spin cast films, a result supported by previous TFT work on ADT-TES-F films spin cast onto PFBT-treated substrates with Au electrodes.[98;99] Indeed, our simulations revealed that higher photocurrents in spin cast thin films can be partially attributed to an increase in hole mobility (μ_{p0} in Table 1) and to a significant increase in the charge photogeneration efficiency (Figure 3.5), especially that of the FE pathway (Figure 3.5(a)). The larger zero-field hole mobility value (μ_{p0} in Table 2.1),

smaller Poole-Frenkel mobility electric field dependence factor (γ_p in Table 3.1), lower trap density (N_p in Table 3.1), and lower average trap depth (Δ in Table 3.1) for the spin cast film are consistent with lower disorder due to larger crystallite sizes in this film, as compared to those in the drop cast sample, as seen from the optical images in the insets of Fige 3.6.

A comparison of the charge photogeneration efficiencies via SSC (ξ_{SSC}) and FE dissociation pathways ($\xi_{FE} * \eta_{FE}$, where $\eta_{FE} = k_{diss,FE}/\left(k_{diss,FE} + k_{r,FE}\right)$ is the efficiency of FE dissociation) is shown in Figure 3.5. Both ξ_{SSC} and $\xi_{FE} * \eta_{FE}$ were higher in the spin cast film; however, the most pronounced difference between the drop cast and spin cast films was in the efficiency of the FE formation ξ_{FE}, which was significantly larger in the spin cast film (e.g. 79% in the spin cast film, as compared to 20% in the drop cast film, at 40 kV/cm, Figure 3.9). Additionally, the simulations revealed that the FE dynamics differed significantly between the drop cast and spin cast films (X in Figure 3.7), as the lifetime of the FE in the spin cast film ($46 - 67\ ns$, depending on the electric field) was 3-4 times longer than that in the drop cast film.[21] This suggests that recombination of the charge-generating FE in ADT-TES-F films occurs largely at the grain boundaries; it is less efficient in our spin cast film due to its larger crystallite sizes as compared to those in a drop cast film. This is in contrast to the PL-emitting ADT-TES-F exciton, which exhibits a considerably shorter PL lifetime in spin cast films[100] as compared to drop cast films,[13;79] and properties of which are related to exciton delocalization within the crystallite.[81]

The total amount of charge generated at ns time scales, given by $\xi_{SSC} + \xi_{FE} * \eta_{FE}$, was higher by a factor of $\sim$3–4, depending on the electric field, in the spin cast film. As discussed above, this is mostly due to the differences in the FE formation efficiency, whereas the efficiency of FE dissociation, η_{FE}, was comparable in the spin cast and drop cast samples.

A schematic representation of the distribution of photoexcitation among various relaxation pathways is shown in Figure 3.9.

The initial decay of the photocurrent (Figure 3.6) in the spin cast sample was much slower than that in the drop cast sample. Our simulation results indicate that this difference is primarily due to the different charge trapping and recombination characteristics of the two films (Figure 3.7). The free hole-trapped electron trap-assisted recombination rate $B_{p_f n_t}$ is particularly important.[21] The considerably lower value of $B_{p_f n_t}$ in the spin cast film indicates that holes are less likely to encounter trapped electrons, and less likely to recombine if they do encounter each other, as compared to that in the drop cast film. This suggests that a large number of trap states in ADT-TES-F films form on grain boundaries, which are considerably reduced by the PFBT treatment of the substrate with Au electrodes combined with the spin cast deposition method.[98] This manifests in the reduced trap densities $N_{p(n)}$ and the trap-assisted recombination rates $B_{p_f n_t}(B_{n_f p_t})$, as well as shallower traps (Δ in Table 1) in the spin cast film as compared to the drop cast film. This process competes with the higher hole mobility causing carriers to encounter traps more often, as evidenced by the values of bulk trapping rates $B_n N_n$ and $B_p N_p$ shown in Table 3.1. The overall effect is an increased speed of initial charge trapping and slower relaxation of the free and trapped charge densities in spin cast films (Figure 3.7).

3.3.2 Intensity Dependence

One of the tests of robustness for a model describing photocurrent dynamics is the model's ability to predict the dependence of charge carrier dynamics on various external parameters

such as electric field, light intensity, and temperature. Having successfully fit multiple voltages, I now turned my focus to the origin of light intensity-dependent TPC and, in particular, to the contributions of charge carrier density-dependent recombination (such as bimolecular recombination) and mobility to the TPC amplitude and dynamics. The dependence of mobility on charge carrier concentration (defined as the ratio of free charge carrier and total hopping site densities)[51] has primarily been explored in field-effect transistors, where the carrier concentration can be controlled by varying the gate voltage. However, the field-effect mobility is heavily influenced by charge trapping and metal-organic interface effects, which obscure the direct effect of carrier concentration on charge transport. Carrier concentration dependence in low-mobility ($\mu < 10^{-3} cm^2/Vs$) polymers with hopping charge transport has been extensively studied theoretically.[51] A review of several numerical models found that the carrier density dependence of mobility could be parametrized by a simple exponential.[51] These models utilize a Miller-Abrahamss hopping rate and a Gaussian density of states (DOS), the applicability of which to materials with higher mobilities ($\mu > 1\ cm^2/Vs$) such as organic single crystals, is still under debate[48;52;53;57;58] and is explored here. In addition, the Wojcik-Tachiya correction to the Onsager-Braun exciton dissociation model was used (see Ch. 2.3.1).

The simulated photocurrents obtained for the thin film and single crystal devices using Eq. 2.13 and the parameter values reported in Table 3.1 are presented in Figure 3.8. Table 3.1 presents results from a fit of single crystal TPC at 20 kV/cm and 5 $\mu J/cm^2$. The single crystal devices exhibited considerably higher peak photocurrent densities and slower initial decay dynamics as compared to those in thin film samples (Figure 3.6). The ultrafast SSC charge generation pathway (characterized by ξ_{SSC}) was significantly more efficient in single crystals

than in films, consistent with previous work showing a strong dependence of SSC efficiency on film crystallinity.[15] In contrast, the FE dissociation-based contribution to charge generation ($\xi_{FE}\eta_{FE}$) was similar in these two systems, consistent with the previous observation that the FE contribution to charge generation in bulk heterojunctions with the ADT-TES-F donor largely originates from the intra-grain ADT-TES-F regions.[15] The rate of the initial photocurrent decay depends on charge carrier recombination and trapping properties; for example, faster initial decay in ADT-TES-F/PCBM blends as compared to pristine ADT-TES-F films has previously[15] been attributed to bimolecular recombination. A considerably slower initial decay rate in single crystal devices as compared to thin films (Figure 3.6) is a combination of reduced trap densities (Np and Nn), shallower traps (Δ), and reduced free hole-trapped electron recombination ($B_{p_f n_t}$) in the single crystal (Table 3.1). Also observed in the single crystal are increased FE recombination (k_R) and free electron-trapped hole recombination ($B_{n_f p_t}$) rates as compared to the thin film.

Having successfully found a basis fit for the single crystal samples, I proceeed to compare TPC fits using h_1 and h_2 density dependence functions from Eqs. 2.13 & 2.14 at multiple incident intensities. Exemplar results are shown in Figure 3.8. Although both h_1 and h_2 approaches could reproduce the data reasonably well at particular light intensities (e.g. Figure 3.8a), neither h_1 nor h_2 fully captured the TPC dynamics over the entire light intensity range studied (Figure 3.8b-d), which corresponded to carrier concentrations of $10^{-5} - 10^{-4}$ carriers/site. Figures 3.8c & d show TPCs integrated over a 20 ns time period and TPC peak amplitudes, respectively, obtained from experimental data (circles) and numerically simulated TPCs using h_1 (squares) and h_2 (diamonds). The h_1 approach slightly overestimated the TPC amplitude throughout the entire intensity range and overestimated the extracted

charge at low intensities. The h_2 approach predicted a stronger intensity dependence of the TPC amplitude than the one observed experimentally, but matched the change in the extracted charge with intensity better than h_1 throughout the entire intensity range. This indicates that light intensity dependence of the TPC dynamics at sub-ns time scales (reflected in that of the TPC amplitude) is mostly determined by charge carrier density-dependent recombination (bimolecular and/or trap-assisted), in which mobility does not depend on carrier concentration. However, at longer time scales (reflected in the integrated TPC), and at low intensities ($< 10\mu J/cm^2$), additional intensity-dependent contributions may become important. This includes carrier density-dependent charge carrier mobility, for which the simulations using the h_2 approach predicted about a $\sim$12% increase in overall mobility over the range of light intensities used in our experiments (Figure 3.8d, inset).[51]

3.4 D/A composites

The model that takes into account only the SSC and FE channels of carrier photogeneration produced good fits for pristine ADT-TES-F photocurrents, but it was unable to accurately replicate the more complicated photocurrent dynamics of drop cast composite films. The insets of Figure 3.11 show the best results of fitting the photocurrent at the electric fields of $60kV/cm$ and $40kV/cm$ in the ADT-TES-F/Pn-TIPS-F8 (A) and ADT-TES-F/PCBM (B) composites, with the models that include FE dissociation-only (dash-dotted line, pathway 2 in Figure 2.2) and both the SSC and FE dissociation pathways (dashed line, pathways 1 and 2, respectively, in Figure 2.2). In addition, there was little consistency in the fits across the studied electric field range, and our multiple-electric-field fitting process was unable

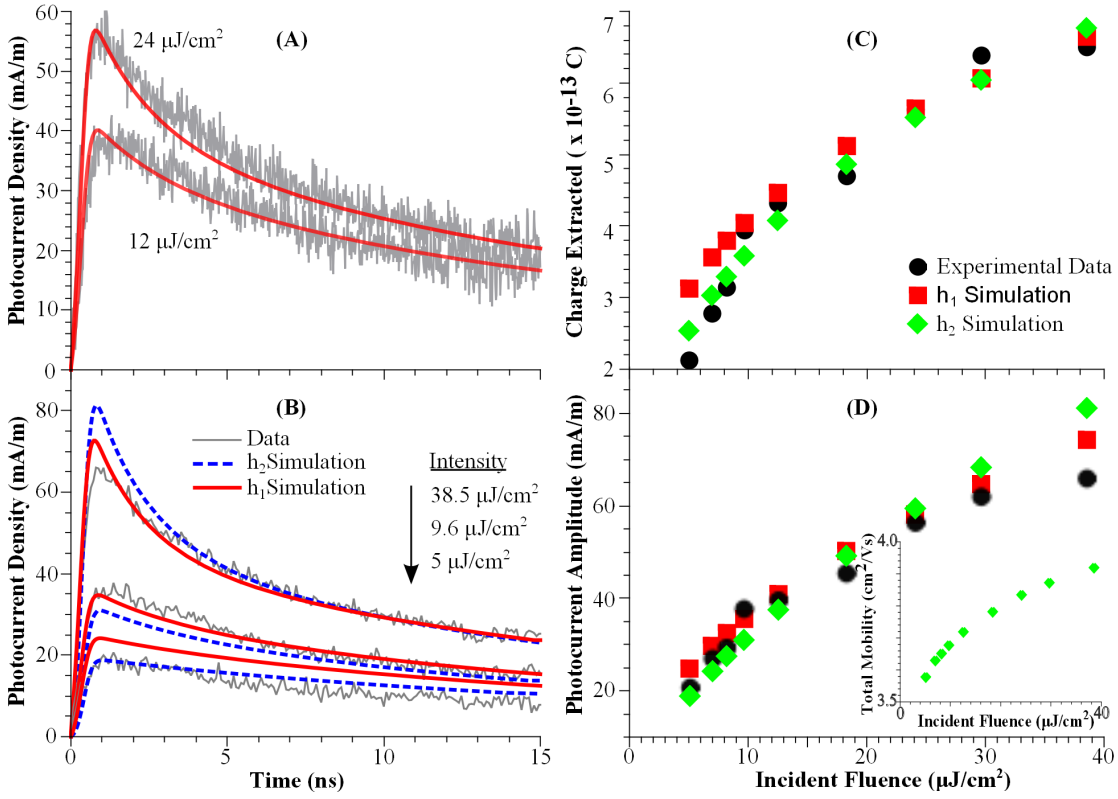

Figure 3.8: Results from intensity dependence simulations. (A) TPC data along iwth simulations using h_1 for two light intensities. (B) TPC data and simulations using h_1 and h_2 for miltiple intensities. (C) Integrated TPC photocurrent values and (D) TPC amplitude for experiment and simulations using h_1 and h_2. Inset: Sum of mobilities $(\mu_n + \mu_p)$ calculated using h_2 for multiple intensities.

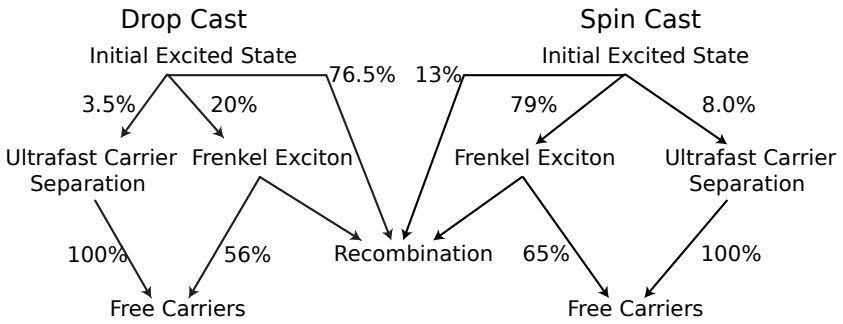

Figure 3.9: Flowcharts showing distribution of photoexcitation among various relaxation pathways in drop cast and spin cast films. The values of each pathway efficiency are exemplars from the 40 kV/cm fits multiplied by 100%.

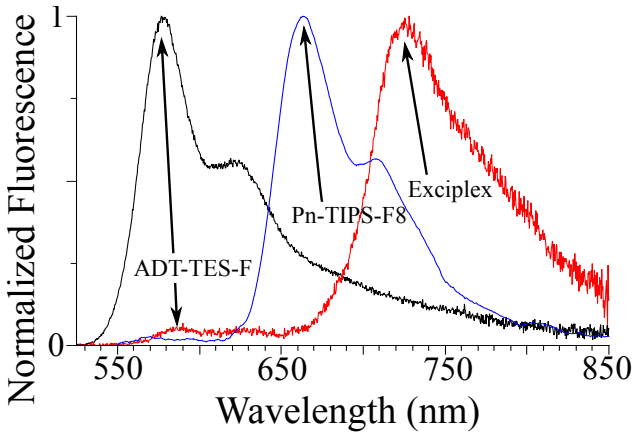

Figure 3.10: Normalized fluoresence for pristine ADT-TES-F (black), pristine Pn-TIPS-F8 (blue), and ADT-TES-F + 30 wt% Pn-TIPS-F8 (red) films. Note the clear exciplex peak at ∼725 nm and the extreme quenching of the donor fluorescence in the blended film.

to replicate the correct electric field dependence of the transients. Previous work in my group[79] identified a possibility of charge generation via CT exciton dissociation in several D/A composites with the ADT-TES-F donor, with a CT exciton that may or may not be detectable by PL measurements, depending on the acceptor. For example, in the ADT-TES-F/Pn-TIPS-F8 D/A composite, an exciplex that formed between the donor HOMO and the acceptor LUMO was detected by the PL emission (Figure 3.10) and was considered as a potential contributor of charge carriers via exciplex dissociation. In contrast, in the ADT-TES-F/PCBM D/A composite, no exciplex emission was detected; however, based on the photocurrent dynamics and partial quenching of the ADT-TES-F donor PL, it was inferred that there might exist dark CT states that form between the ADT-TES-F donor and PCBM acceptor, which could contribute to charge carrier generation. The existence of this state is also consistent with work in polymer/PCBM blends.[1]

3.4.1 Drop Cast Films

Based on these considerations, to accurately reproduce the photocurrent dynamics in composite films, I added the CT vartion of Eq. 2.19 and the CT terms for Eqs 2.15 & 2.17 to the set of equations used, representing the charge generation pathway 4 in Figure 2.2, which proceeds via CT exciton dissociation. To describe CT exciton dissociation, we used the Onsager-Braun model, similar to that of the FE dissociation, but with a different initial pair separation a_{CT} and recombination rate $k_{r,CT}$. Thus, in D/A composites there are three competing channels of charge photogeneration: the fast SSC pathway, FE dissociation, and CT exciton dissociation (pathways 1, 2, and 4, respectively, in Figure 2.2), with the relative

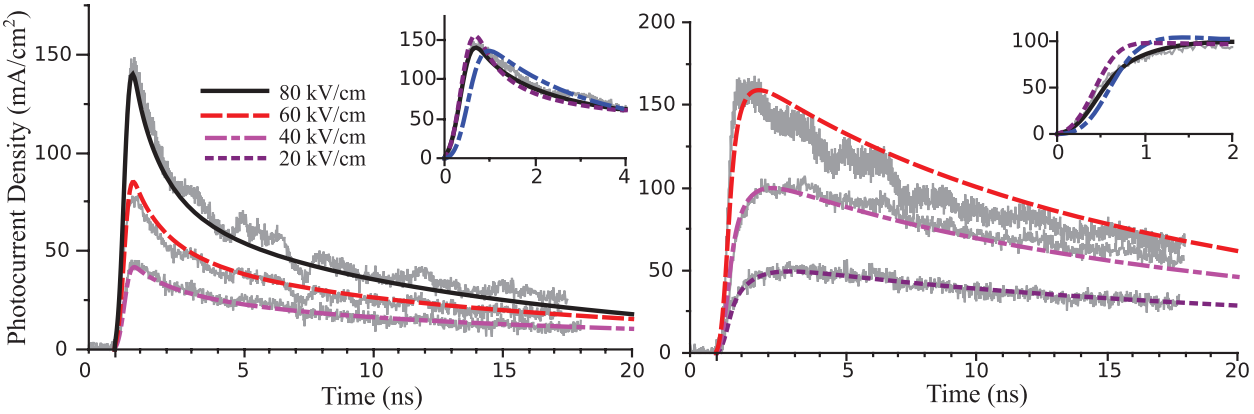

Figure 3.11: Photocurrent densities, experimentally measured at various applied electric fields, superimposed with those simulated using Eqs.(2.15-2.26) with the parameters listed in Table 2.1, for: (left) ADT-TES-F/Pn-TIPS-F8 2 wt% composite, and (right) ADT-TES-F/PCBM 2 wt% composite. Insets illustrate effects of different charge generation pathway choices and show best fits to the data obtained using: (left) 60 kV/cm and (right) 40 kV/cm: FE dissociation pathway 2 only (dash-dotted line), combined SSC and FE dissociation pathways 1 and 2, respectively (dashed line), and combined SSC, FE dissociation and CT exciton dissociation pathways 1, 2, and 4, respectively (solid line).

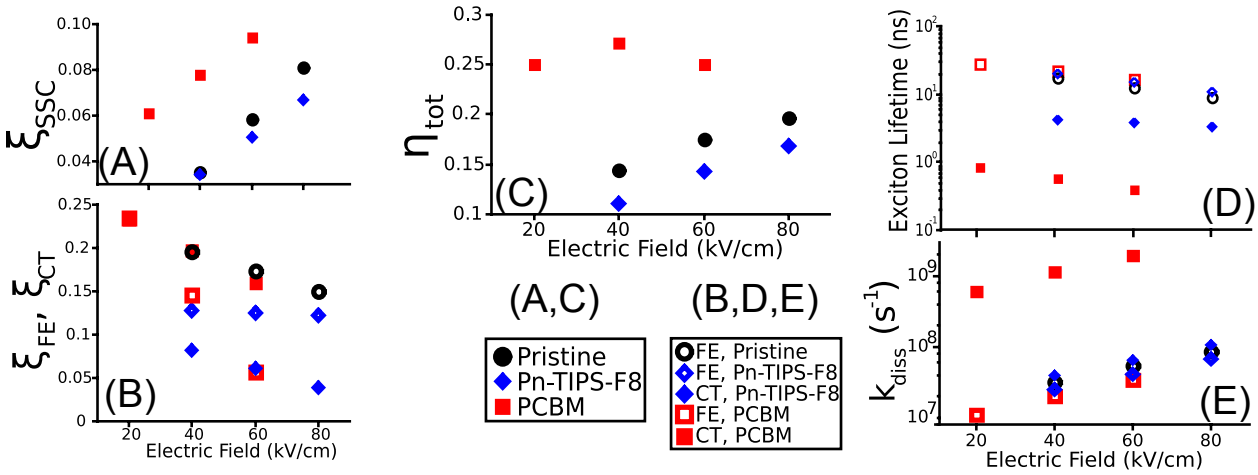

Figure 3.12: Comparison of electric field dependence of various parameters in drop cast pristine and BHJ films. (A) Fraction of absorbed photons which follow SSC pathway. (B) Fraction of absorbed photons which follow FE and CT exciton pathways. (C) Total charge generation efficiency. (D) FE and CT exciton lifetimes. (E) FE and CT exciton dissocation rates.

contribution of each pathway to the overall charge photogeneration being electric field dependent. Since the exact pathway of CT state formation is unknown,[32;81] we did not impose restrictions on the relative values of γ_{SSC}, γ_{FE}, and γ_{CT} in Eq. 2.25. Resulting fits are shown in Figure 3.11. The addition of the CT exciton dissociation improved the goodness-of-fit ratings for the fits to the data from the composite films (Figure 3.11). The fit to the data from the composite with the PCBM acceptor at an applied electric field of 60 kV/cm was lower quality than the fits to the data at lower electric fields due to the assumption of Eq. 2.25 breaking down at higher electric fields. As in pristine drop cast ADT-TES-F films, the efficiency of fast carrier generation via the SSC pathway was below 10% (Figure 3.12A) in both D/A composites under consideration.

In the composite with the Pn-TIPS-F8 acceptor, ~ 0.12 ($\sim 0.04 - 0.08$) of the absorbed

photon density N_{ph} formed the charge-generating FE (CT exciton) (Figure 3.12B). These dissociated during their lifetimes (Figure 3.12D) with the electric field dependent efficiency η_{FE} (η_{CT}), calculated using Eq. 3.1, of $0.49-0.72$ ($0.17-0.35$) in the studied range of electric fields. This yields a fraction of N_{ph} contributing to the overall charge photogeneration via the FE (CT exciton) dissociation pathway, $\xi_{FE}\eta_{FE}$ ($\xi_{CT}\eta_{CT}$), of $0.062-0.088$ ($0.014-0.015$). The contribution of the CT dissociation to charge carrier generation in this composite, given by $\xi_{CT}\eta_{CT}/\eta_{tot}$, is the lowest of the three contributing pathways at 8-12%, which is consistent with our previous observation of strong PL emission from the ADT-TES-F/Pn-TIPS-F8 CT state (exciplex), indicative of a tightly bound CT state with a relatively low dissociation rate $k_{diss,CT}$ (Figure 3.12E).[79] The total fraction of the absorbed photon density which results in charge carrier photogeneration at time scales of $\sim 20\ ns$, is

$$\eta_{tot} = \xi_{SSC} + \xi_{FE}\eta_{FE} + \xi_{CT}\eta_{CT}. \tag{3.3}$$

It increases slightly, from ~ 0.11 to ~ 0.17, as the electric field increases from $40kV/cm$ to $80kV/cm$ (Figure 3.12C). The rest of the photoexcitation, given by $1-\eta_{tot}$, which amounts to $\sim 83-89\%$ of the absorbed photons, does not contribute to charge carrier photogeneration in the time domain studied.

In the composite with the PCBM acceptor, the CT exciton formed considerably more efficiently (ξ_{CT} in Figure 3.12B) and was considerably more prone to dissociation than that in the composite with the Pn-TIPS-F8 acceptor. As a result, the contribution of the CT exciton dissociation (pathway 4) into the overall charge photogeneration, $\xi_{CT}\eta_{CT}$, of $0.12-0.13$ (i.e. $12-13\%$) of the absorbed photon density was a factor of ~ 8.5 larger than in the ADT-

TES-F/Pn-TIPS-F8 composite. It also dominated over pathway 2 (charge generation via FE dissociation), especially at low electric fields, which converted only 3–7 % of the absorbed photons into charge carriers.

Table 2.1 summarizes other parameters pertaining to charge generation and transport in the studied drop cast D/A composites. In both composites, the hole and electron mobilities were reduced as compared to those in pristine ADT-TES-F films, whereas the average trap densities were increased; this result is expected given our effective medium approach to charge transport modeling in these composites with low acceptor concentration. In both composites, the effective hole trap depth was increased with respect to that in pristine ADT-TES-F films (41 and 39 meV in the composites with Pn-TIPS-F8 and PCBM, respectively), due to an increased disorder in the composite films.

Figure 3.13 summarizes the distribution of the photoexcitation among various pathways for the drop cast pristine ADT-TES-F films and ADT-TES-F/Pn-TIPS-F8 and ADT-TES-F/PCBM composites at low acceptor concentrations at the applied electric field of 40 kV/cm. In pristine ADT-TES-F films at this field, the contribution of the pathway 2 (FE dissociation) to ns time-scales charge photogeneration was a factor of ~ 3.1 larger than that of the pathway 1. This dominance of the pathway 2 progressively reduced as the electric field increased. In ADT-TES-F/Pn-TIPS-F8 composites, pathway 2 dominated over pathway 1 by a factor of $\sim$ 1.6, whereas the contribution of pathway 4 (CT exciton dissociation) to the charge generation was a factor of $\sim$ 4.5 lower than that of the pathway 2 and slightly decreased with the electric field. In contrast, in ADT-TES-F/PCBM composites, pathway 4 was the dominant factor, contributing about half of all charge carriers ($\xi_{CT}\eta_{CT}/\eta_{tot} \approx 0.49$), while the other half was distributed nearly evenly between pathways 1 and 2. The pathway 4 contribution

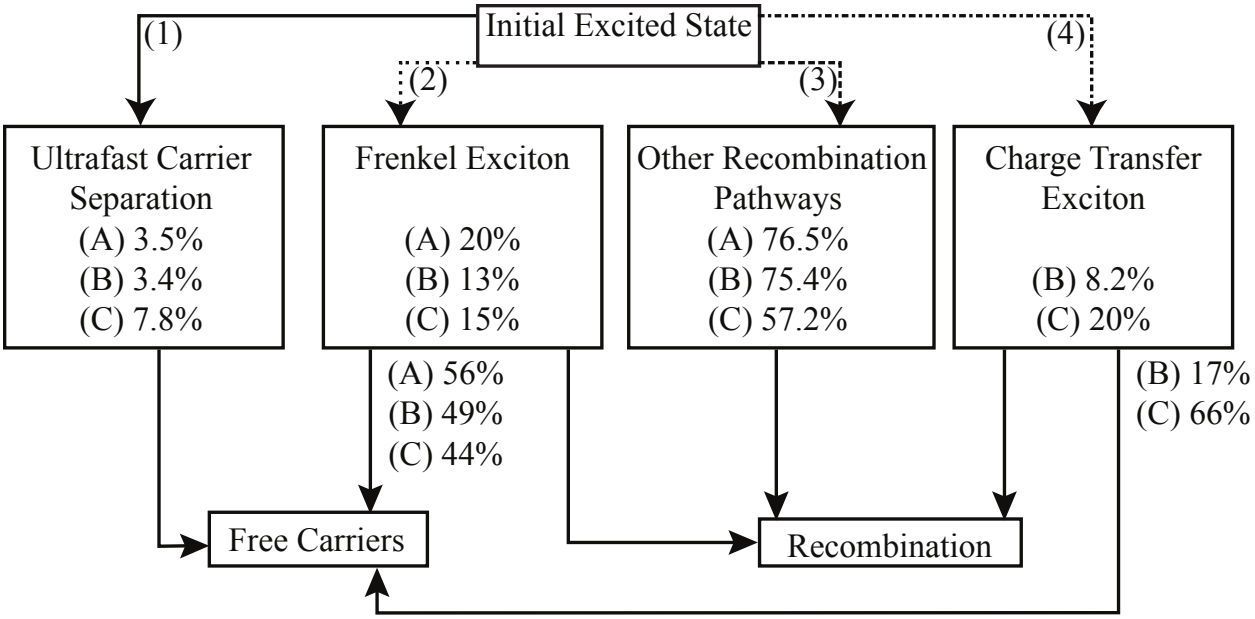

Figure 3.13: Summary of distribution of the total photoexcitation (100%) among various relaxation paths at an applied electric field of 40 kV/cm. Values are given for a pristine ADT-TES-F film (A), an ADT-TES-F/Pn-TIPS-F8 2 wt% composite film (B), and an ADT-TES-F/PCBM 2 wt% composite film (C). Values in boxes are fractions ξ from Figure3.12C multiplied by 100%, whereas values below the boxes are dissociation efficiencies $\eta_{FE,CT}$ of Eq.(3.1), also multiplied by 100%.

was weakly field dependent in the studied range, whereas the trends in relative contributions of pathways 1 and 2 followed those of pristine ADT-TES-F films. Note that in spite of electric field dependence of various parameters contributing to charge photogeneration, the total charge photogeneration efficiency in ADT-TES-F/PCBM composites (Figure 3.12C) is electric field independent in the studied range of electric fields, similar to that reported in D/A systems with polymeric donors and PCBM acceptors.[101;102]

As discussed in Ch. 1, ultrafast charge carrier photogeneration has been observed in a variety of small-molecule and polymeric organic semiconductors via ultrafast spectroscopy

methods,[32;54;103;104] Auston switch-based techniques,[76;105;106] and fast oscilloscope detection of photocurrents.[13;40;107] In most cases, the efficiency of this process is at or below $\sim 10\%$, in agreement with values of ξ_{SSC} (which dominates charge generation at fast time scales) extracted from our simulations. Many of these methods enable determination of the product of the sum of hole and electron mobilities ($\mu_{tot} = \mu_p + \mu_n$) and of the photogeneration efficiency. In our films the $\mu_{tot}\xi_{SSC}$ values (Figure 3.12C and Table 2.1) are between ~ 0.02 and $0.06\ cm^2/Vs$, in good agreement with experimental observations from similar films.[13;40;54] However, the mechanism of achieving the SSC state at ultrafast time scales in ADT films is unknown. Some possibilities are discussed in Ch. 1. The electric field dependence of the parameter ξ_{SSC} observed here is consistent with hot excitons and with some delocalization models.

The simulations revealed that a FE with lifetimes on the order of 10–20 ns (Figure 3.12D) contributes a considerable number of charge carriers at ns time-scales through pathway 2 in Figure 2.2. In the drop cast D/A composites, the FE lifetimes were similar to those in the pristine ADT-TES-F film (Figure 3.12D), which confirms that the FE state is formed on the ADT-TES-F donor. There are several possible origins of such FE states. For example, these could be dark states that are delocalized over several ADT-TES-F molecules in the ADT-TES-F H-aggregates,[81] similar to those in H-aggregates of sexithiophene films.[108] Both drop cast D/A composites tested exhibit a relatively strong PL from the relaxed ADT-TES-F excitons.[79;81] The emissive ADT-TES-F excitons at room temperature are highly mobile within disordered ADT-TES-F H-aggregates, which shortens their PL lifetimes from about 13 ns (for isolated molecules) to 1-2 ns (in films).[81] As discussed in the previous section, these excitons do not contribute to photocurrents at ns time-scales and cannot be the charge-

generating FE states of Figure 2.2.[79;81] Instead, these are the excitons that constitute most of the photoexcitation ($\sim$ 80% of absorbed photons) that does not produce charge carriers. However, since the PL lifetimes of the FE in Figure 3.12D are close to the PL lifetimes of isolated ADT-TES-F molecules,[13] the alternative assignment for the FE states observed here could be relatively immobile ADT-TES-F excitons, possibly formed at grain boundaries, which are longer lived and have more time to dissociate as compared to the highly mobile excitons that constitute the majority of the photoexcited species.[81] This is consistent with the simulations of pristine ADT-TES-F spin cast films and single crystals presented in Sec. 3.3.

The simulations established that the CT state in the ADT-TES-F/Pn-TIPS-F8 composite, contributing to charge photogeneration through pathway 4 in Figure 2.2, exhibits lifetimes of 3.4-4.5 ns (Figure 3.12D). These are close to experimentally measured PL lifetimes of the exciplex (3.8-4.6 ns, depending on the applied electric field) in this composite, which suggests that the nature of the charge-generating CT state in Figure 2.2 is the exciplex shown in Figure 3.10.[79] Indeed, low contribution of the CT states to the photocurrent in this composite is consistent with a highly emissive tightly bound exciplex, in agreement with previous experiments.[79] The CT state in the composite with the PCBM acceptor was found to exhibit considerably lower lifetimes (Figure 3.12D) than those of the ADT-TES-F FE and the CT in the composite with the Pn-TIPS-F8 acceptor. Additionally, it was more dissociative than either of these excitons (Figure 3.12E), which is consistent with a larger LUMO offset between ADT-TES-F and PCBM and larger D/A separation due to the size of the PCBM molecule as compared to Pn-TIPS-F8, both of which factors have been shown to enhance the photocurrent.[79;109]

The total amount of charge generated at ns time-scales, 0.1–0.25 of absorbed photon density (Figure 3.12C), only differs by a factor of ~ 2 in all three drop cast systems, with the highest in the composite with the PCBM acceptor followed by pristine ADT-TES-F film and finally the composite with the Pn-TIPS-F8 acceptor, consistent with my group's previous observations.[79] However, previous studies[79] also established that the amount of mobile charge over the period of 1 μs, obtained by integrating transient photocurrents over this time period, as well as photocurrents obtained under cw illumination, are considerably higher (by a factor of ∼6–10) in the composite with the PCBM acceptor as compared to pristine ADT-TES-F films. Based on our simulation results, this is due to a considerably lower rate of recombination between trapped electrons and free holes in the ADT-TES-F/PCBM composite ($B_{p_f n_t}$ in Table 2.1 and FigureS2), which results in a significantly slower decay of the photocurrent in this composite, and thus higher charge retention, as compared to that in pristine ADT-TES-F films. This could be due to trapped electrons being localized in or near the PCBM domains, where a relatively lower hole mobility reduces the rate of free holes encountering trapped electrons.

3.4.2 Spin Cast Films

For the remaining results, the Wojcik-Tachiya correction to the Onsager-Braun model[33] was used (see Ch. 2.3.1).

Having successfully fit drop cast films with small acceptor concentrations, a comprehensive investigation of the effects of acceptor concentration and acceptor type was undertaken by myself and Keshab Paudel, a post-doc in my group.[15] Pn-TIPS-F8, IF-Mes,[110] and

Parameter	ADT-TES-F	10% PCBM	10% Pn-TIPS-F8	15% IF-MES
μ_n (V/cm^2) $(\pm.07)$	0.25	0.3	0.35	0.18
μ_p (V/cm^2) $(\pm.05)$	0.87	0.85	0.87	0.73
$B_{n_t p_f}$ $(m^3 s^{-1})$ $(\pm 3 \times 10^{-7})$	2.1×10^{-6}	1.9×10^{-6}	6.7×10^{-7}	2.0×10^{-6}
$k_{diss,FE}$ (s^{-1}) $(\pm 5 \times 10^6)$	2.6×10^7	2.4×10^7	2.6×10^7	1.9×10^7
$k_{diss,CT}$ (s^{-1}) $(\pm 5 \times 10^6)$	-	5.2×10^7	1.5×10^7	4.1×10^7
η_{CT} (± 0.005)	-	0.17	0.017	0.076
τ_{FE} (ns) (± 5)	27	26	25	30
τ_{CT} (ns) (± 0.5)	-	3.4	1.1	1.9

Table 3.2: Several fit parameters for a pristine spin cast ADT-TES-F film and selected spin cast D/A films. Listed uncertainties indicate the range of values found in different individual devices.

PCBM were used as acceptors (Figure 3.2). The choice of the acceptor molecules was guided by the following considerations. Pn-TIPS-F8 and IF-Mes molecules have similar LUMO energy levels (Figure 3.2), which yield D/A LUMO energy offsets of ∼0.55 eV. (Such offsets should favor high power conversion efficiencies,[24;78] although the validity of quantitative assessments of the photoinduced charge transfer (CT) efficiency based on this characteristic has been debated in the literature.[111]) However, these two molecules exhibit considerably different solid-state packing motifs and excited state dynamics, properties known to affect CT and charge generation, thus creating different scenarios for photoexcitation relaxation pathways in D/A blends with these acceptors.[112] In particular, the Pn-TIPS-F8 exhibits 2D "brick-work" π-stacking (similar to ADT-TES-F) in the solid state, it is fluorescent, and when blended with the ADT-TES-F donor an emissive CT state (exciplex) with a lifetime of ∼4 ns forms.[79;100] In contrast, IF-Mes does not yield π-stacked structures,[110] and it is non-fluorescent due to fast non-radiative relaxation. For comparison, D/A blends with the fullerene acceptor PCBM commonly utilized in organic BHJs were also studied.

Measured photocurrent transients and simulation results are shown in Figure 3.14. Simulations revealed that ξ_{SSC} is the main parameter responsible for the trends in I_{pk} observed in Figure 3.14(b). In ADT-TES-F/PCBM films, ξ_{SSC} increased from $\xi_{SSC} = 0.036$ in pristine donor films to $\xi_{SSC} = 0.195$ in ADT-TES-F/PCBM blends at 10 wt% PCBM, followed by a decrease at higher concentrations (Figure 3.14(c)). In contrast, in composites with Pn-TIPS-F8 and IF-Mes acceptors, ξ_{SSC} gradually decreased with the acceptor concentration, a trend similar to experimental observations in Figure 3.14(b). The total contribution of FE dissociation to the photocurrent ($\xi_{FE}\eta_{FE}$ in Figure 3.14(d)) did not significantly depend on the acceptor, consistent with the FE charge generation occuring entirely inside ADT-TES-F donor domains, only slightly affected by the presence of the D/A interfaces. Unlike in drop cast blends, the CT exciton dissociation ($\xi_{CT}\eta_{CT}$ in Figure 3.14(d)) contributed a relatively small percentage of all photogenerated charge carriers in each spin cast composite tested.

The size of the initial peak is strongly dependent on the fraction of excited carriers that follow the SSC path, consistent with results reported above. The rest of the shape of the transient is formed by the interaction between trapping and recombination effects. The total amount of extracted charge is only loosely dependent on the total charge generation efficiency, η_{tot}. The increase in photocurrent in the PCBM composite films is caused primarily by an increase in the SSC charge generation, and a reduction in the detrapping rate. The reduction in detrapping rate reduces the amount of free charge being recombined, leading to a larger total photocurrent.

In almost all cases, the addition of an acceptor to ADT-TES-F caused a reduction in mobility and ultrafast charge generation (ξ_{SSC}).[79;81;100;107] The only exception is the addition of a fullerene acceptor, which led in some cases to a significant improvement in ξ_{SSC} (Figure

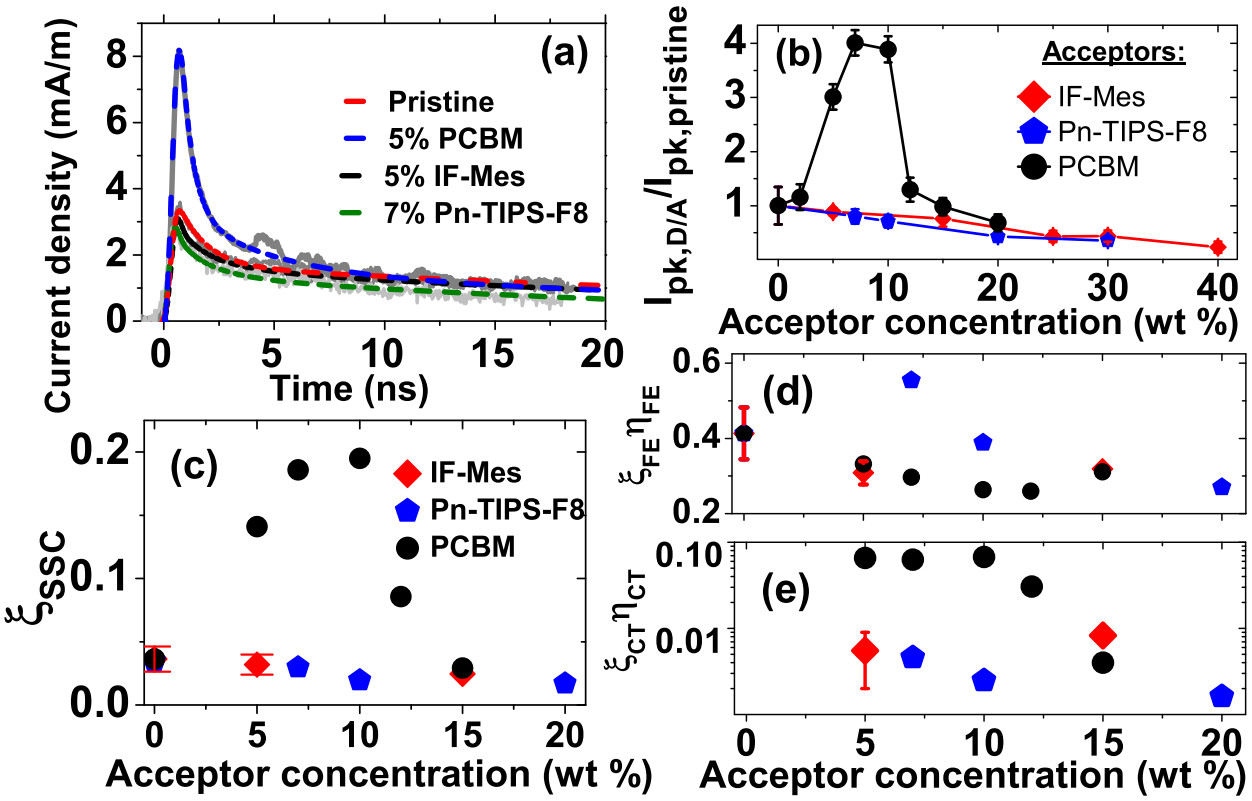

Figure 3.14: (a) Transient photocurrents measured in pristine ADT-TES-F donor and various D/A films at 50 kV/cm. Dashed and dotted colored lines represent numerically simulated photocurrents. (b) Peak photocurrent at 50 kV/cm, normalized by that in pristine ADT-TES-F films, as a function of acceptor concentration for the D/A blends with three different acceptors.(c-e)Efficiency of (c) ultrafast charge separation ξ_{SSC} and of charge photogeneration via FE (d) and CT exciton (e) dissociation extracted from numerical modeling of the measured photocurrents in various samples. The legends for (d) and (e) are omitted for clarity, but are identical to (c). Error bars are included for several concentrations to illustrate sample-to-sample variation in the fit parameters.

3.14). Clues for the cause of this behavior are provided by the XRD data shown in Figure 3.15. In all films, peaks at 5.4° (001), 16.3° (003), and 21.7° (004) were observed, confirming the crystalline nature of our films with a vertical d-spacing of 16.6 Å, characteristic of the ADT-TES-F donor (Figure 3.15(a)).[4;113] Addition of Pn-TIPS-F8 and IF-Mes acceptors led to an overall reduction in the crystallinity of ADT-TES-F donor, here quantified by using the area under the (001) peak (Figure 3.15(b)), and no formation of crystalline acceptor domains could be detected. Conversely, the addition of PCBM in concentrations of up to 10 wt% led to a dramatic enhancement of the *donor* crystallinity (Figure 3.15(b)),[114] correlated with the enhancement in I_{pk} (Figures 3.14(b) and 3.15(c)). Additionally, in samples with 7 and 10 wt% PCBM, a small peak was observed at 10.7° and 10.8°, respectively (Figure 3.15(a), inset), due to crystallization of the PCBM.[115] As the PCBM concentration further increased, the ADT-TES-F donor crystallinity, as well as I_{pk} (Figure 3.15(c)), decreased, and the peak due to PCBM crystallite formation could not be detected. These results may suggest that hole delocalization due to crystallinity of the ADT-TES-F donor is the dominant factor in ultrafast charge carrier separation in pristine ADT-TES-F films and ADT-TES-F-based D/A blends, and that the efficiency of this process can be further improved by electron delocalization in a crystalline acceptor.

One of the advantages of simulation is that individual densities can be traced through time in addition to current. Figure 3.16 shows the time evolution of transient photocurrents in ADT-TES-F/PCBM blends with various PCBM concentrations. At higher PCBM concentrations (e.g. 15 wt%), the photocurrent amplitude is lower and the initial decay is slower than that in blends with 5-10 wt% of PCBM.

Figure 3.17a shows transient photocurrent data, along with numerically simulated cur-

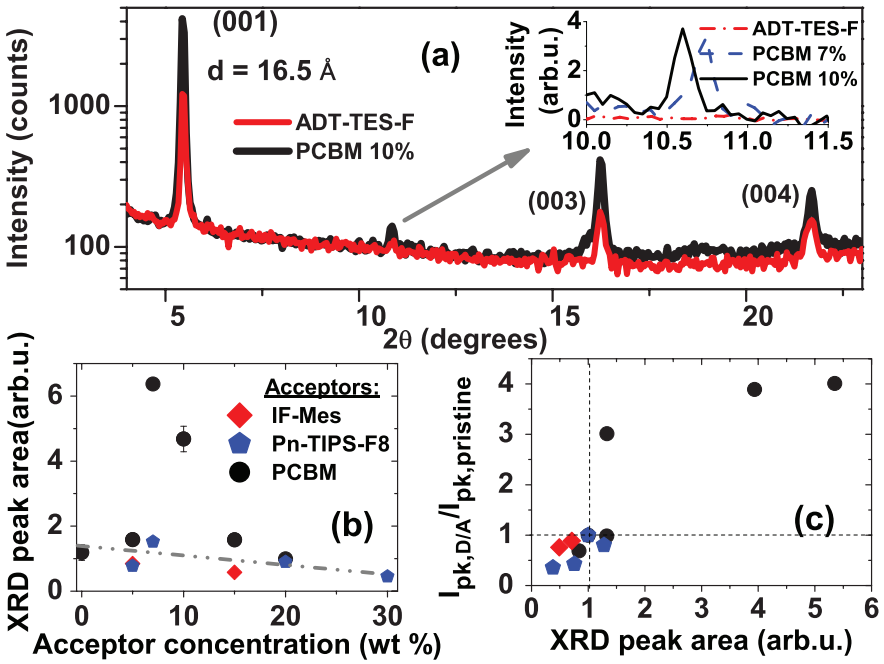

Figure 3.15: (a) XRD results for out-of-plane structures in pristine ADT-TES-F and ADT-TES-F/PCBM 10 wt% films. Inset shows a magnified view of the peak due to PCBM crystallization in D/A films with 7 wt% and 10 wt% of PCBM. Data from a pristine ADT-TES-F film in the same 2θ region are also included. (b) The (001) donor peak area obtained in different samples. The line provides a guide for the eye. (c) Peak photocurrent normalized by that in pristine ADT-TES-F films as a function of the (001) donor peak area normalized by that in pristine ADT-TES-F films for the D/A blends studied. The legend for (c) is identical to (b)

.

rents that include the SSC-only and FE dissociation-only contributions to the photocurrent in pristine ADT-TES-F films and the SSC-only, FE dissociation-only, and CT exciton dissociation-only contributions for several D/A blends. The figure demonstrates that in all samples, the SSC pathway of charge photogeneration was the dominant contribution to the transient photocurrent in the first nanosecond after excitation.

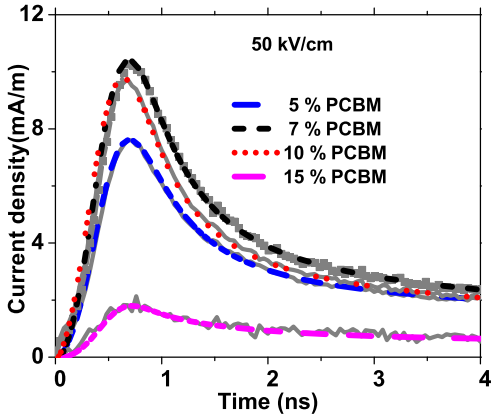

Figure 3.16: A close-up of transient photocurrents obtained in a ADT-TES-F/PCBM D/A blends with varying PCBM concentrations. Numerically simulated photocurrents (colored dashed and dotted lines) are also included.

Figure 3.17b shows a faster decay of both hole and electron density, immediately after the 470 ps pulsed excitation, due to increased bimolecular recombination in the ADT-TES-F/PCBM 5 wt% D/A blend, as compared to pristine ADT-TES-F film. This causes a considerably faster initial decay of the transient photocurrent in D/A blends with the PCBM acceptor at concentrations of up to 10 wt% (Figure 3.14(a)), as compared to that in pristine ADT-TES-F films.

3.5 Conclusions

The model described in Ch. 2 has been applied to a wide variety of samples and used to characterize the active charge generation, transport, and trapping effects. In pristine ADT-TES-F samples, increased crystallinity correlates with higher carrier mobility, increased ultrafast (ps or sub-ps) charge generation,

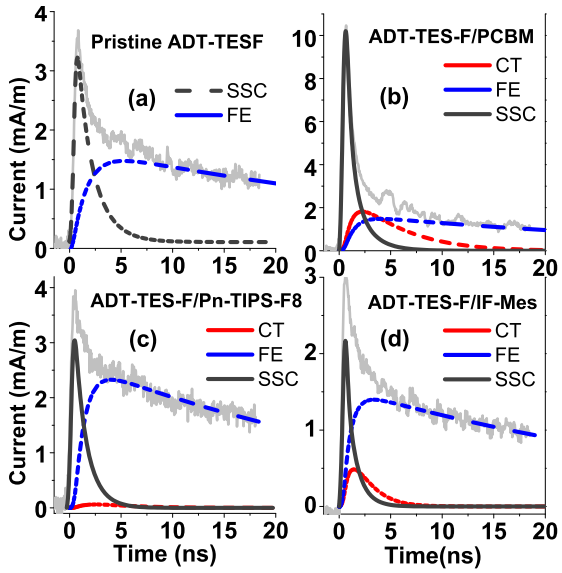

(a) Transient photocurrents obtained in (a) a pristine ADT-TES-F film, and in (b) ADT-TES-F/PCBM 10 wt%, (c) ADT-TES-F/Pn-TIPS-F8 7 wt%, and (d) ADT-TES-F/IF-Mes 5 wt% D/A blends. Numerically simulated photocurrents (colored dashed and dotted lines) illustrating separate contributions from the SSC, FE dissociation, and CT exciton dissociation charge photogeneration pathways are also included.

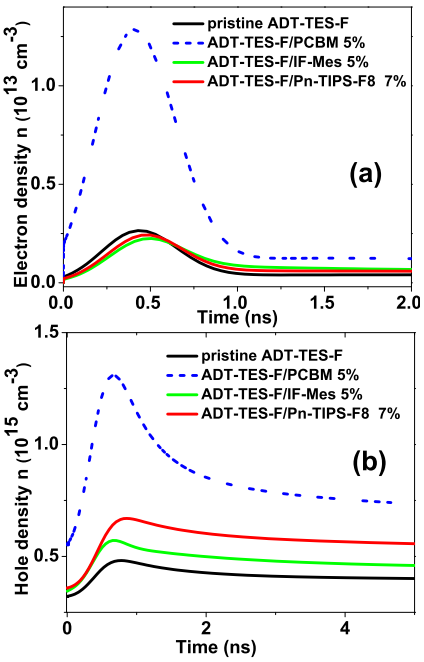

(b) Numerically simulated time evolution of hole (a) and electron (b) density upon 532 nm 470 ps excitation of a pristine ADT-TES-F film, ADT-TES-F/PCBM 5 wt%, ADT-TES-F/Pn-TIPS-F8 7 wt%, and ADT-TES-F/IF-Mes 5 wt% films. Faster carrier density decay, due to increased bimolecular recombination, is observed in the D/A blends with PCBM. A similar effect is also seen in measured transient photocurrents.

reduced geminate recombination, and reduced trapping effects. In D/A composites at all concentrations, donor crystallinity as revealed via XRD is correlated with high carrier mobility and high ultrafast charge generation efficiency (ξ_{SSC}). In D/A composites at low concentrations, charge generation due to CT excitons is an important pathway, providing $\sim 50\%$ of all charge carriers in ADT-TES-F/2% PCBM and $\sim 4-8\%$ in ADT-TES-F/2% Pn-TIPS-F8. In D/A composites at high concentrations, an increase in the acceptor concentration increases trapping and reduces ultrafast charge generation except in ADT-TES-F/PCBM samples with between 5 and 10 wt% acceptor. In those samples, an increase in PCBM concentration leads to an enhancement of charge mobility and ultrafast charge generation as well as an enhancement in ADT-TES-F crystallinity. The model has also been applied to test the effects of varying voltage and incident intensity on the transient photocurrent. Increasing voltage leads to a larger proportion of initial excitation following the ultrafast SSC path in all samples studied. The origin of intensity dependence is unclear, but I showed that multiple theories can be tested against each other using this model.

Chapter 4: Novel fungal OSMSC

4.1 Introduction

One of the drivers of research into organic semiconductors is the potential to find alternatives to silicon that are cheaper, more sustainable, and/or more environmentally friendly to produce. A virtually unexplored avenue for acheiving this is biologically-produced small molecules. In this section, I explore the potential of xylindein (Figure 4.1), a pigment secreted by the wood staining fungus *Chlorociboria aeruginosa*, as an organic semiconductor. This is prompted by the ability of my collaborator Dr. Genevieve Weber to produce large amounts of clean material by growing liquid cultures of the fungus and by the curious properties of xylindein.

The molecular structure of xylindein is shown in Figure 4.1. The core of the molecule is *peri*-xanthenoxanthene (PXX), derivatives of which have been studied for use in thin film transistors and other organic electronics.[116–118] PXX was initially investigated due to the potential for a stable π-stacked system.[116] PXX based devices displayed a high hole mobility ($0.4\ cm^2/Vs$) and excellent stability.[116] I investigated the basic optical and electronic properties of xylindein through UV-Vis absorption, fluorescence, and excitation spectroscopy, PL transients and dark and photo current measurements. I also tested several film deposition methods, trying to establish the best method.

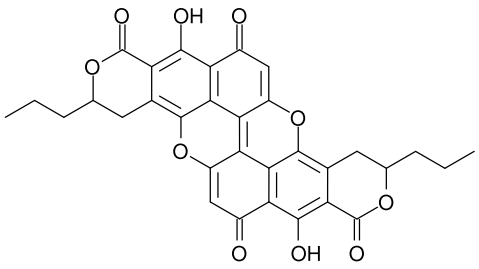

Figure 4.1: The molecular structure of xylindein

4.2 Experimental

Details of fluorescence, absorption, PL transient, and current measurements can be found in Section 3.2. Excitation spectra and some absorption spectra were taken using a Horiba fluorimeter. Some films were prepared by drop casting, using the method outlined in Section 3.2, except that the temperature of the hot plate used was widely varied widely, between room temperature and $\sim 200\ ^{\circ}C$. Other films were prepared via low pressure organic vapor deposition (LPOVD)[119], a method where the xylindein is evaporated at high temperature and carried towards a room temperature substrate by a neutral carrier gas.

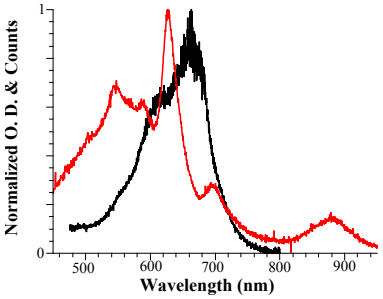

(a) Absorption (black) and PL spectra (red) of xylindein in chlorobenzene solution.

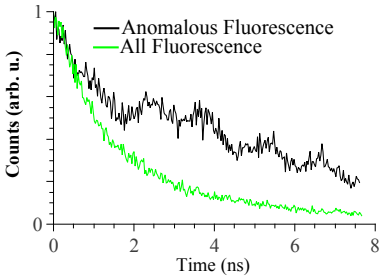

(b) Photoluminescence transients for xylindein.

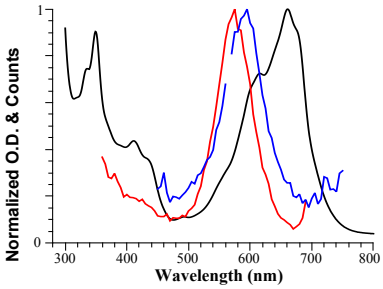

(c) Absorption (black) and excitation spectra at 700 nm (red) and 850 nm (blue) of xylinden in chlorobenzene solution.

4.3 Results

4.3.1 Optical Properties

4.3.1.1 Solution

Initial explorations were performed on xylindein extracted from liquid culture and cleaned via an HPLC process, resulting in solutions of unknown purity and concentration. Fluorescence and absorption spectra for this "unclean" xylindein are shown in Figure 4.2a. The $S_0 \rightarrow S_1$ transition can be clearly seen as the $\sim$ 660 nm absorption peak, making the fluorescence peak at $\sim$ 570 nm anomalous, apparently breaking Kasha's rule. Molecules which violate Kasha's rule are rare, but many have been documented.[17] However, there are many potential explanations for this kind of anomalous fluorescence that don't rely on breaking Kasha's rule. Steer[120] wrote a brief but comprehensive overview of the challenges in establishing fluorescence from transitions other than $S_1 \rightarrow S_0$.

As a first check, I measured the fluorescence lifetimes for different bands of xylindein

fluorescence. TPL plots for the anomalous band and all fluorescence can be found in Figure 4.2b. The nanosecond scale of the decay was the first indication that the anomalous fluorescence was not $S_2 \rightarrow S_0$ emission, as $S_2 \rightarrow S_0$ emission must be significantly faster than the $S_1 \rightarrow S_0$ fluorescence, generally under a nanosecond, in order to compete with the $S_2 \rightarrow S_1$ transition.[120] Additionally, absorbtion and excitation spectra taken using a fluorimeter (Figure 4.2c) do not match up, confirming a highly fluorescent, low concentration impurity as the source of the anomalous fluorescence.

Even after several iterations of trying different purification methods, my collaborators have not succeeded in producing xylindein absent this fluorescent impurity. Despite this, we have established an upper bound on the quantum yield of xylindein: under 0.5% in solution. Xylindein also shows clear solvatochromism, with a blue shift as solvent polarity increases.

4.3.1.2 Solid State

When drop cast, xylindein forms amorphous films, with the optical properties somewhat affected by hot plate temperature and annealing. Sample absorptions as a function of deposition temperature are shown in Figure 4.3a. Film absorption displays a small red shift from solution, with the first absorption peak moving from 690 to 710 nm. In addition, the first and second absorption peaks balance out, with the second peak about the same height as the first. This is consistent with H-aggregation.[121] As annealing time and heat increase, the absorption graph flattens out, probably indicating degradation of the xylindein. The impurity fluorescence increases significantly as annealing time and temperature increase, indicating that the impurity may be a decay product of xylindein.

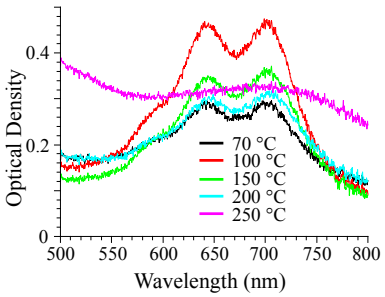

(a) Absorption of xylindein films as a function of deposition temperature

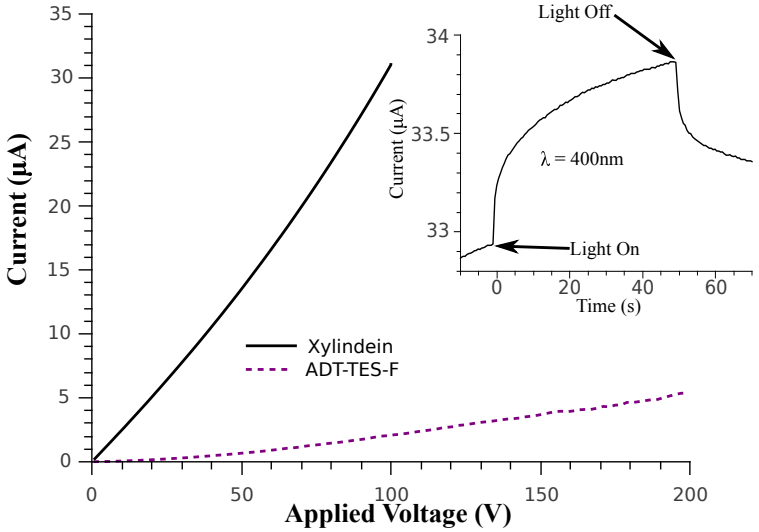

(b) A sample I-V curve for a characteristic xylindein device. Inset shows onset and fall of photocurrent.

4.3.2 Electronic Properties

Drop cast xylindein films have highly variable properties, somewhat dependent on deposition temperature. A sample IV curve of a device on Au electrodes is shown in Figure 4.3b. On Au electrodes, xylindein shows close to ohmic current, with the best films displaying larger dark current than ADT-TES-F. The photocurrent is modest at best, as can be seen in the inset for Figure 4.3b. In addition, the rise of the photocurrent is very slow, not reaching a equilibrium even after 50 seconds of CW excitation. This suggests that charge generation in the pristine material is excitonic, with a low yield and a long exciton lifetime. The decay to a higher baseline than before excitation apparent in the inset points towards a high trap density with a long trapped charge lifetime. The high dark current and low photocurrent indicates that xylindein's has potential as a transistor material. It is unlikely to be useful as

a solar cell donor, but further work is necessary to determine xylindein's viability as a solar cell acceptor or dopant.

4.4 Conclusion

While xylindein itself has issues with purification and a very low fluorescence, *Chlorociboria aeruginosa* has many related wood-eating fungi which boast a large number of different secretions. The potential for xylindein as a transistor material shows that there may be more promising undiscovered organic electro-optic materials waiting to be characterized. This work is the first time that an absorption or photoluminescence spectrum for xylindein has been published, despite its absolute structure being known since the 1960s. These unexplored molecules present a new frontier for organic material research.

Chapter 5: Conclusion

A complete understanding of charge generation and transport is essential to the future of organic electronics, and over the past five years there has been a great deal of excellent work done in this field. It has been an exciting time, with well-accepted models weakened and big unanswered questions brought closer and closer towards solution. When I began development of my model, the Onsager-Braun model was the standard model. Its position today is much shakier, with so much of the important charge generation in modern materials occuring via other, much less settled pathways. This work supports that movement, providing important context in the under-studied 1–20 ns time scale.

I developed a model which revealed multiple charge generation pathways active on the nanosecond time scale and quantified the contribution of each pathway to the transient photocurrent. It showed that the ultrafast pathway was the most direct contributor to extracted current, indicating that improving the number of charges which follow this pathway is an excellent route to improving device performance. Investigating the relationship between film structure and device performance, my coworkers and I showed that increasing crystallization leads to more efficient ultrafast carrier generation and thus better performing devices. The drop in performance which most D/A composite films show relative to pristine ADT-TES-F can be explained by this relationship. Most acceptor dopants reduce the crystallinity of the ADT-TES-F donor material, with the exception of certain proportions of PCBM, where the device performance increases due to enhanced ultrafast charge generation caused by an

increase in crystallinity.

The future of the simulation project is bright, with several promising avenues for continued development. The concentration dependence simulations can be improved by incorporating a more accurate trap assisted recombination model and testing more concentration dependent mobility models. The parameters we extract around exciton dissociation and recombination may be useful for analyzing transient photoluminescence data, adding another data set which can be simulated using a single parameter set, improving the robustness of the extracted values. Simulating the temperature dependence of TPC data is also a promising direction, allowing for testing several aspects of the model.

Even if the charge generation and transport questions are settled soon, organic electronics still face a number of challenges for industrial and commercial application. Many of the best organic materials are expensive, difficult, or environmentally unfriendly to produce. The preliminary work with xylindein presents a possible solution for those production challenges, with the fungal colonies potentially producing large amounts of material in a sustainable and environmentally friendly way. The family of wood-eating fungi which xylindein belongs to boasts a large number of different species which produce a wide variety of different organic secretions. The potential for one of these to be a high performing semiconductor material justifies future work in characterizing these materials, testing their optical and electronic properties.

APPENDICES

Appendix A: Simulation Code

All of the simulations use the same structure, with an optimization.m main file which sets the data input and NLOPT optimization parameters. The NLOPT package calls a function 'transient' stored in transient.m which returns the objective function value for a given input array. 'transient' uses a function 'odes' in odes.m with Matlab's built-in ode15s solver to solve the ODE system. The following are examples of these files, from a multi-voltage fit of an ADT-TES-F/ADT-TIPS-CN composite film. The last file is the code used to generate control plots, as described in Ch. 3.1.

A.1 Optimization.m

```
% Constructs an opt structure, an initial points vector x,and runs
% nlopt_optimize on the function defined in sgTransient.m
% x = [muN0, muP0, Bn, Bp, Bnpt, Bntp, Ea, v, Nn, Np, Gmax]
% See transient.m and ab-initio.mit.edu/wiki/index.php/Main_Page for more
% documentation
clear;
try
    matlabpool 3
catch error
    matlabpool close
    matlabpool 3
end

%Temp Results Globals
```

```
15 global xmin;
16 global fmin;
17 global ctr;
18 ctr = 0;
19 fmin = -100;
20 %Simulation Parameter globals
21 global Voltage;
22 global ObjRange;
23 global RemRange;
24 global ExParams; %Parameters from Pristine TESF fit for non-CT excitons
25 global gData;
26 global Nph;
27
28 Voltage = [150 125 100];
29 ObjRange = [59 500;62 500;59 500];
30 RemRange = [0 0;0 0;0 0];
31 ExParams = [1.17753e-09,2.56839e+07]; %a, kR from Pristine fit
32
33 AvgEnergy = [378e-6, 380e-6, 387e-6]; %Incident avg energy (W)
34 dTh = 1e-6; %Estimated thickness of current surface (m)
35 RepRate = 50e3; %Laser repetition rate (Hz)
36
37 Wavelength = 532e-9; %Laser wavelength (m)
38 SpotRad = 0.5e-3; %Approximate laser spot radius (m)
39 Abs = 1; %Optical Density of sample at wavelength (OD)
40 h = 6.626e-34; %Planck Constant (J*s)
41 c = 2.9979e8; %Speed of light in vaccuum (m/s)
42 Eph = h*c/Wavelength; %Energy of incident photon
43 Nph = AvgEnergy/(RepRate*Eph*pi*SpotRad^2*dTh) * 10^(-Abs); %Density of absorbed photons per pulse (m^-3)
44
45 filename = {'~/Post-JAP_transient_formatted_data/TIPSCN10wt/150V_532nm_378uW_0p04ns.txt'; ...
46     '~/Post-JAP_transient_formatted_data/TIPSCN10wt/125V_532nm_380uW_0p04ns.txt'; ...
47     '~/Post-JAP_transient_formatted_data/TIPSCN10wt/100V_532nm_387uW_0p04ns.txt';};
48
49 opt.verbose = 1;
```

```
50 opt.algorithm = NLOPT_LN_COBYLA;
51 opt.xtol_rel = 1e-4;
52 opt.ftol_rel = 1e-6;
53 opt.min_objective = @transient;
54 opt.lower_bounds = [0.01, 0.4, 5e-8, 6e-6, 6e-9, 1e-8, 1e-5, 1e-8, 15, 1e18, 5e17, 0.0005, 1e-5, ...
55                     .1, -9e-3, .3, -6e-3, 1.15e-9, 6e7];
56 opt.upper_bounds = [.15, .6, 5e-6, 6e-4, 7e-7, 1e-6, 1e-3, 1e-6, 35, 1e20, 5e19, 0.05, 1e-3, 0.4, ...
57                     -9e-6,0.5,-6e-5,1.35e-9,6e9];
58 opt.fc = {@botNTrapBound,@topNTrapBound,@botPTrapBound,@topPTrapBound,@fobctBound,@obBound, ...
59         @ctBound,@muBound,@muValBound,@CTltBotBound,@CTltTopBound};
60 opt.fc_tol = [1e-10, 1e-10, 1e-10, 1e-10, 1e-10, 1e-10, 1e-10, 1e-10, 1e-10, 1e-10];
61
62 x=[0.0775785, 0.48318, 2.14274e-06, 4.6758e-05, 9.23138e-08, 7.01451e-07, 0.000363696, ...
63    5.55506e-08, 29.5296, 9.45279e+18, 1.39765e+18, 0.00257603, 0.000294483, 0.16241, -0.000986171, ...
64    0.40233, -0.000744217, 1.2609e-09, 4.22378e+08];
65
66
67 %Data to compare
68 %Data should be in a .csv or .txt file formatted as '%g, %g', aka a
69 %simple {comma space} delimited format. Columns should be unheaded, with Column
70 %1 being time in ns, and Column 2 being current density in A/m
71 dTh = 1e-6; %Estimated thickness of current surface (m)
72 gData = cell(length(Voltage),1);
73 for ii = 1:length(Voltage)
74    fileID = fopen(filename{ii}, 'r');
75    gData{ii} = fscanf(fileID, '%g,%g', [2 inf])';
76    gData{ii}(:,1) = gData{ii}(:,1) * 10^-9; %Convert ns times to s times
77    gData{ii}(:,2) = gData{ii}(:,2) / dTh; %Converting A/m -> A/m^2
78 end
79
80 [xopt, fopt, retcode] = nlopt_optimize(opt,x);
81
82 plotname = {strcat('TESF + 10% TCPS, ', int2str(Voltage(1)),' Volts');...
83             strcat('TESF + 10% TCPS, ', int2str(Voltage(2)),' Volts');...
84             strcat('TESF + 10% TCPS, ', int2str(Voltage(3)),' Volts')};
```

```
85  [Rsq, Xlt, CTlt, kD, kDct] = plotTransients(xopt,plotname,filename)
86
87  FID = fopen('Results.txt','a');
88  fprintf(FID,'ExParams = [%g,%g];\n', ExParams(1), ExParams(2));
89  fprintf(FID, 'x=[%g,%g,%g,%g,%g,%g,%g,%g,%g,%g,%g,%g,%g,%g,%g,%g,%g,%g,%g,%g];\n',...
90          xopt(1), xopt(2), xopt(3), xopt(4), xopt(5), xopt(6), xopt(7), xopt(8), xopt(9), xopt(10),...
91          xopt(11), xopt(12), xopt(13), xopt(14), xopt(15), xopt(16), xopt(17), xopt(18), xopt(19));
92  fprintf(FID,strcat('V = [%g, %g, %g];\nmuN0 = %g\nmuP0 = %g\ngN = %g\ngP = %g\nBn = %g\nBp = %g',...
93                     '\nBnpt = %g\nBntp = %g\nDelta = %g\nNn = %g\nNp = %g\nNph = [%g,%g,%g]',...
94                     '\nf0 = %g\ngF = %g\nob0 = %g\ngOB = %g\na = %g\nkR = %g\nct = %g\ngCT = %g',...
95                     '\naCT = %g\nkRct = %g\neta = [%g,%g,%g]\netaCT = [%g,%g,%g]\nfval = %g',...
96                     '\nObjRange = [%g %g;%g %g;%g %g];\nRemRange = [%g %g;%g %g;%g %g];',...
97                     '\nfilename = %s\nRsq=[%g, %g, %g]\nXlt=[%g,%g,%g]\nCTlt=[%g,%g,%g]',...
98                     '\nkD=[%g,%g,%g]\nkDct=[%g,%g,%g]\n\n\n'),...
99          Voltage, xopt(1), xopt(2), xopt(3), xopt(4), xopt(5), xopt(6), xopt(7), xopt(8), xopt(9),...
100         xopt(10), xopt(11), Nph(1), Nph(2), Nph(3), xopt(12), xopt(13), xopt(14), xopt(15),...
101         ExParams(1), ExParams(2), xopt(16), xopt(17), xopt(18), xopt(19), kD./(kD+ExParams(2)),...
102         kDct./(kDct+xopt(19)), fopt, ObjRange(1, :), ObjRange(2, :), ObjRange(3, :),...
103         RemRange(1, :), RemRange(2, :), RemRange(3, :), filename{1}, Rsq, Xlt, CTlt, kD, kDct);
104
105 fclose(FID);
106
107 matlabpool close;
```

A.2 Transient.m

```
1  %transient.m. An implementation of a model for transient photocurrent,
2  %without space dependence.
3
4  function val = transient(x)
5      tic;
6
7      global fmin;
8      global xmin;
```

```
9     global ctr;
10    global Voltage;
11    global ObjRange;
12    global RemRange;
13    global ExParams;
14    global gData;
15    global Nph;
16    ctr = ctr + 1;
17
18    %Simulation Constants Constants
19    e = 1.602e-19; %Elementary Charge (C)
20    e0 = 8.854e-12; %Permittivity of free space (A^2 * s^4 * m^-3 *kg^-1)
21    eR = 3; %Relative permittivity
22    kB = 1.38065e-23; %Boltzmann constant (J / K)
23    T = 300; %Temperature, K
24    d = 25e-6; %Device size (m)
25
26    PphiB = 0.25 * 1.602e-19; %Injection Barrier for Holes in J
27    NphiB = 2.05 * 1.602e-19; %Injection Barrier for Electrons in J
28
29    tFinal = 20e-9; %Total simulation time (s)
30    dt = 10^-13; %Time step for gaussian (s)
31
32    val = 0; %Final Objective function value
33
34    %Basic Parameter Assignment
35    muN0 = x(1)*10^-4; %Base electron mobility (m^2 / (Vs))
36    muP0 = x(2)*10^-4; %Base hole mobility ( m^2 / (Vs))
37    gN = x(3); %Electron Field Mobility Dependence ( (m/V)^.5 )
38    gP = x(4); %Hole Field Mobility Dependence ( (m/V)^.5 )
39    Bn = x(5)*10^-6; %Electron trapping constant (m^3 / s)
40    Bp = x(6)*10^-6; %Hole trapping constant (m^3/s)
41    Bnpt = x(7)*10^-6; %Electron+trapped hole recombination constant (m^3/s)
42    Bntp = x(8)*10^-6; %Hole+trapped electron recombination constant (m^3/s)
43    Delta = x(9) * 10^-3 * 1.602e-19; %Hole Detrapping Rate (s^-1)
```

```
44      Nn = x(10)*10^6; %Density of electron traps (m^-3)
45      Np = x(11)*10^6; %Density of hole traps (m^-3)
46      f0 = x(12); %Percentage of hot excitons that become SSC states
47      gF = x(13); %Field dependence of f
48      ob0 = x(14); %Percent of absorbed carriers that become O-B excitons
49      gOB = x(15); %Field Dependence for ob
50      ct0 = x(16); %Percent of absorbed carriers that become CT excitons
51      gCT = x(17); %Field Dependence for ct
52      a = ExParams(1); %Initial spatial separation of O-B excitons
53      kR = ExParams(2); %Recombination rate of O-B excitons
54      aCT = x(18); %Initial spatial separation of CT excitons
55      kRCT = x(19); %Recombination rate of CT excitons
56
57
58      Volt = Voltage;
59      myObjRange = ObjRange;
60      myRemRange = RemRange;
61      Data = gData;
62      NphLocal = Nph;
63      parfor(mm = 1:length(Voltage))
64
65          V = Volt(mm);
66          E = V/d;
67
68          dtData = abs(Data{mm}(1,1) - Data{mm}(2,1));
69          zeroPos = abs(Data{mm}(1,1) / dtData) + 1;
70          zeroPos = cast(zeroPos,'uint64');
71          JDark = Data{mm}(zeroPos,2);
72
73          muN = muN0 * exp(gN*sqrt(E));
74          muP = muP0 * exp(gP*sqrt(E));
75          f = f0+V*gF;
76          ob = ob0+V*gOB;
77          ct = ct0+V*gCT;
78          Bpt = Np*Bp*exp(-Delta/(kB*T));
```

```
79
80      %Scaling Block, see Theory pg 56 for details
81      N0 = JDark / (e*E*(muP + muN*exp((PphiB-NphiB)/(kB*T)))); % m^-3, the initial hole density
82      Diff = 1e-4; %m^2/s
83      Vkt = kB*T/e; % V
84      Ld = sqrt(e0*eR*kB*T/(e^2*N0)); % m
85      t0 = Ld^2 / Diff; % s
86      J0 = e*Diff*N0/Ld; % A/m^2
87
88      JDarkSc = JDark / J0;
89
90      tFinalSc = tFinal / t0;
91
92      ESc = E * Ld / Vkt;
93
94      NphSc = NphLocal(mm) / N0;
95      muNSc = muN * Vkt / Diff;
96      muPSc = muP * Vkt / Diff;
97      BnSc = Bn * N0 * t0;
98      BpSc = Bp * N0 * t0;
99      BnptSc = Bnpt * N0 * t0;
100     BntpSc = Bntp * N0 * t0;
101     NnSc = Nn / N0;
102     NpSc = Np / N0;
103     BptSc = Bpt * t0;
104     %End Scaling Block
105
106     %Constructing Gaussian Beam Profile, 500ps pulse
107     %Final result is # of excitons created per sec
108     %Need to divide by dt for units and normalize total area of gaussian
109     tLit = 5e3; %tLit * dt = Full Width Half Max of Gaussian pulse
110     tGfinal = tFinal / dt;
111     FWHM = tLit * dt;
112     sig = FWHM / (2*sqrt(2*log(2)));
113     FWTM = 2*sqrt(2*log(10))*sig;
```

```
114         tGauss = 0:dt:(tGfinal*dt);
115         beamProfile = gaussmf(tGauss,[sig (FWIM / 2)]);
116         tGaussSc = tGauss/t0;
117         Gvec = NphSc*beamProfile/trapz(tGaussSc,beamProfile);
118
119         %Calc of dissociation rates
120         %Langevin recombination rate scaled for ODEs (scale: N0 * t0)
121         g = e*(muN+muP)/(e0*eR) * t0*N0;
122         %Langevin recombination rate scaled for kD calcs ( scale: 1/(Ld*Diff) )
123         gSc = e*(muN + muP)/(e0*eR) * (1/(Ld*Diff));
124
125         Eb = e^2 / (4*pi*e0*eR*a);  %Coulombic Exiton Binding Energy (J)
126         EbCT = e^2 / (4*pi*e0*eR*aCT);
127
128         b = e^3 * E / (8*pi*e0*eR*kB^2*T^2);
129         bessel = besselj(1,2*sqrt(-2*b));
130         bCT = e^3 * E / (8*pi*e0*eR*kB^2*T^2);
131         besselCT = besselj(1,2*sqrt(-2*b));
132
133         kDSc = real(gSc .* Ld^3 .* exp(-Eb/(kB*T)) .* bessel ./ (4*pi*a^3*sqrt(-2*b)));
134         kCTd = real(gSc .* Ld^3 .* exp(-EbCT/(kB*T)) .* besselCT ./ (4*pi*aCT^3*sqrt(-2*bCT)));
135
136         kRSc = kR*t0;
137         kCTr = kRCT*t0;
138
139         %Initial Conditions
140         %See Theory notebook pg 40-41 for explanation
141
142         n0 = JDarkSc / (ESc * (muNSc + muPSc*exp((NphiB-PphiB)/(kB*T))));
143         p0 = 1;
144         nt0 = BnSc*NnSc*n0 / (BnSc*n0 + BntpSc*p0);
145         pt0 = BpSc*NpSc*p0 / (BpSc*p0 + BnptSc*n0 + BptSc);
146         X0 = 0;
147         CT0 = 0;
148
```

```
149         Y0 = [n0; nt0; p0; pt0; X0; CT0];
150
151         options = odeset('NonNegative',[1 2 3 4 5]);
152         [t, Y] = ode15s(@(t, y)odes(t, y, tGaussSc, Gvec, g, BnSc, BpSc, BnptSc, BntpSc, BptSc, f,...
153                                     NnSc, NpSc, ob, kDSc, kRSc, ct, kCTd, kCTr),...
154                         [0 tFinalSc], Y0, options);
155
156         t = t *t0;
157         J = ESc*(muNSc*Y(:,1)+muPSc*Y(:,3)) * J0; %A/m^2
158
159        %Final calculation of objective function value
160         if(myRemRange(mm,1) < myObjRange(mm,1))
161             JComp = zeros(1,myObjRange(mm,2) - myObjRange(mm,1));
162             for jj = myObjRange(mm,1):myObjRange(mm,2)
163                 JComp(jj-myObjRange(mm,1)+1) = interp1(t,J,Data{mm}(jj,1));
164             end
165
166             DataComp = Data{mm}((myObjRange(mm,1)):(myObjRange(mm,2)),2)';
167
168            %val = val + sum( (JCompSc - DataCompSc).^2 );
169             SSerr = sum( ( JComp - DataComp ).^2 );
170             yBar = sum(DataComp)./length(DataComp);
171             SStot = sum( (DataComp - yBar).^2);
172             Rsq = 1-(SSerr/SStot);
173
174         else
175             JComp = zeros(1,myObjRange(mm,2) - myObjRange(mm,1) ...
176                             - (myRemRange(mm,2) - myRemRange(mm,1)));
177             for kk = myObjRange(mm,1):myRemRange(mm,1)
178                 JComp(kk-myObjRange(mm,1)+1) = interp1(t,J,Data{mm}(kk,1));
179             end
180             for jj = myRemRange(mm,2):myObjRange(mm,2)
181                 JComp(myRemRange(mm,1)-myObjRange(mm,1)+1 + jj-myRemRange(mm,2)+1) = ...
182                     interp1(t,J,Data{mm}(jj,1));
183             end
```

```
184
185             DataComp = [Data{mm}(myObjRange(mm,1):myRemRange(mm,1),2)',...
186                         Data{mm}(myRemRange(mm,2):myObjRange(mm,2),2)'];
187
188             SSerr = sum( ( JComp - DataComp ).^2 );
189             yBar = sum(DataComp)./length(DataComp);
190             SStot = sum( (DataComp - yBar).^2);
191             Rsq = 1-(SSerr/SStot);
192         end
193         val = val + abs(1-Rsq);
194     end
195
196     if(ctr == 1)
197         fmin = val;
198         xmin = x;
199     elseif (val < fmin)
200         fmin = val;
201         xmin = x;
202     end
203
204     if(isnan(val))
205         FID = fopen('error.txt','a');
206         fprintf(FID,'ExParams = [%g,%g];\n', ExParams(1), ExParams(2));
207         fprintf(FID,'x=[%g,%g,%g,%g,%g,%g,%g,%g,%g,%g,%g,%g,%g,%g,%g,%g,%g,%g,%g,%g];\n',...
208                 x(1), x(2), x(3), x(4), x(5), x(6), x(7), x(8), x(9), x(10), x(11), x(12), x(13),...
209                 x(14), x(15), x(16), x(17), x(18), x(19));
210         fclose(FID);
211         throw(MException('transient:InvalidVal','Transient Function Value is NaN'));
212     end
213
214     if(ctr == 100 || ctr == 500 || ctr == 1000 || ctr == 5000 || mod(ctr,10000) == 0)
215         FID = fopen ('Temp_Results.txt', 'a');
216         fprintf(FID,'ExParams = [%g,%g];\n', ExParams(1), ExParams(2));
217         fprintf(FID,'x=[%g,%g,%g,%g,%g,%g,%g,%g,%g,%g,%g,%g,%g,%g,%g,%g,%g,%g,%g,%g];\n',...
218                 xmin(1), xmin(2), xmin(3), xmin(4), xmin(5), xmin(6), xmin(7), xmin(8), xmin(9),...
```

```
219                 xmin(10), xmin(11), xmin(12), xmin(13), xmin(14), xmin(15), xmin(16), xmin(17),...
220                 xmin(18), xmin(19));
221         fprintf(FID,strcat('V = [%g %g %g]\nmuN0 = %g\nmuP0 = %g\ngN = %g\ngP = %g\nBn = %g',...
222                             '\nBp = %g\nBnpt = %g\nBntp = %g\nBpt = %g\nNn = %g\nNp = %g\nNph = %g',...
223                             '\nf0 = %g\ngF = %g\nob0 = %g\ngOB = %g\na = %g\nkR = %g\nct0 = %g',...
224                             '\ngCT = %g\naCT = %g\nkRct = %g\nfmin = %g',...
225                             '\nObjRange = [%g %g; %g %g; %g %g];',...
226                             '\nRemRange = [%g %g;%g %g;%g %g];\n\n\n'),...
227                 Voltage, xmin(1), xmin(2), xmin(3), xmin(4), xmin(5), xmin(6), xmin(7), xmin(8),...
228                 xmin(9), Nph, xmin(10), xmin(11), xmin(12), xmin(13), xmin(14), xmin(15),...
229                 ExParams(1), ExParams(2), xmin(16), xmin(17), xmin(18), xmin(19), fmin,...
230                 myObjRange(1,:), myObjRange(2,:), myObjRange(3,:), myRemRange(1,:),...
231                 myRemRange(2,:), myRemRange(3,:));
232         fclose(FID);
233     end
234
235     toc
236 end
```

A.3 Odes.m

```
1  function dy = odes(t,y,Gtvec, Gvec, g, Bn, Bp, Bnpt, Bntp, Bpt, f, Nn, Np, ob, kD, kR, ct, kCTd, kCTR)
2  %ODES fxn for solving UCSD thesis ODE equations using ode15s(), with CT
3  %(OB) and O-B excitons added
4  %Inputs/outputs:
5  %  t: Current time value
6  %  y(1), dy(1): free electron density
7  %  y(2), dy(2): trapped electron density
8  %  y(3), dy(3): free hole density
9  %  y(4), dy(4): trapped hole density
10 %  y(5), dy(5): exciton density
11 %  The remainder of the inputs must be set in an anonymous function prior
12 %  to calling the ode solver
13 %  Gtvec: time vector used to generate Gvec. Used for interpolation of G.
```

```
%  Gvec: vector of generation term. Used for interpolation of G.
%  g: Langevin recombination; Bn, Bp: electron/hole trapping rates
%  Bnpt, Bntp: trap assisted recombination rates; tp: hole detrapping rate
%  kD: O–B exciton dissociation rate;  kR: O–B exciton recombination rate
%  Nn, Np: trap densities for electrons/holes;
%  ob: % hot excitons -> O–B excitons; f: % hot excitons -> SSC
%  ct: % hot excitons -> CT excitons; kCTd: CT exciton diss rate
%  kCTr: CT exciton rec rate
G = interp1(Gtvec,Gvec,t);
dy = zeros(4,1); %column vector needed by built in ODE fxns
dy(1) = -g*y(1)*y(3) - Bn*(Nn - y(2))*y(1) - Bnpt*y(1)*y(4) + f*G + kD*y(5) + kCTd*y(6);
dy(2) = Bn*(Nn - y(2))*y(1) - Bntp*y(2)*y(3);
dy(3) = -g*y(1)*y(3) - Bp*(Np - y(4))*y(3) + y(4) * Bpt - Bntp*y(2)*y(3) + f*G + kD*y(5) + kCTd*y(6);
dy(4) = Bp*(Np - y(4))*y(3) - y(4) * Bpt - Bnpt*y(1)*y(4);
dy(5) = G*ob - kR*y(5) - kD*y(5);
dy(6) = G*ct - kCTd*y(6) - kCTR*y(6);
end
```

A.4 Controls.m

```
%controls.m
%An implementation of a model for transient photocurrent,
%without space dependence, with a "hot exciton" model (Theory pg 60)
%–CT adds a separate "Charge Transfer" exciton state, but takes the
%Pristine ob, a & eta as set, so no extra fit parameters
%This file iterates through input parameters, testing multiple values
%in order to test dependence of simulation on each parameter
clear

Voltage = [150, 100, 50];
myObjRange = [129 996;127 992;139 996];
myRemRange = [0 0;0 0;0 0];

%a & kR from pristine TESF fit
```

```
15 ExParams = [1.17753e-09,2.56839e+07];
16
17 e = 1.602e-19; %Elementary Charge (C)
18 e0 = 8.854e-12; %Permittivity of free space (A^2 * s^4 * m^-3 *kg^-1)
19 eR = 3; %Relative permittivity
20 kB = 1.38065e-23; %Boltzmann constant (J / K)
21 T = 300; %Temperature, K
22 d = 25e-6; %Device size (m)
23 dCh = 2.15e-2; %Device channel width (m)
24 dTh = 1e-6; %Estimated thickness of current surface (m)
25
26
27 %Data to compare
28 %Data should be in a .csv or .txt file formatted as '%g, %g\n', aka a
29 %simple {comma space} delimited format. Columns should be unheaded, with Column
30 %1 being time in ns, and Column 2 being current density in A/m
31
32 %filename = strcat('~/Desktop/TESF_formatted_data/Pristine_formatted/Nov172011_', int2str(Voltage),...
33 %                  'V_formatted.txt');
34 %filename = strcat('~/Desktop/TESF_formatted_data/Pristine_formatted/Aug252011_', int2str(Voltage),...
35 %                  'V_formatted.txt');
36 %filename = strcat('~/Desktop/TESF_formatted_data/ND_formatted/TESF_2pc_ND_', int2str(Voltage),...
37 %                  'V.txt');
38 %filename = strcat('~/Desktop/TESF_formatted_data/PCBM_formatted/TESF_2pc_PCBM_', int2str(Voltage),...
39 %                  'V.txt');
40 %filename = strcat('~/Desktop/TESF_formatted_data/TIPS_formatted/TESF_2pc_TIPS_s1_', int2str(Voltage),...
41 %                  'V.txt');
42 %filename = strcat('~/Desktop/TESF_formatted_data/TIPS_formatted/TESF_2pc_TIPS_s2_', int2str(Voltage),...
43 %                  'V.txt');
44
45 % filename = [strcat('~/Desktop/TESF_formatted_data/TC_formatted/TESF_2pc_TCHS_', int2str(Voltage(1)),...
46 %                    'V.txt'); ...
47 %             strcat('~/Desktop/TESF_formatted_data/TC_formatted/TESF_2pc_TCHS_', int2str(Voltage(2)),...
48 %                    'V.txt'); ...
49 %             strcat('~/Desktop/TESF_formatted_data/TC_formatted/TESF_2pc_TCHS_', int2str(Voltage(3)),...
```

```
%                   'V.txt'); ...
%             strcat('~/Desktop/TESF_formatted_data/TC_formatted/TESF_2pc_TCHS_0', int2str(Voltage(4)),...
%                   'V.txt')];

% filename = {strcat('~/Desktop/TESF_formatted_data/ND_formatted/TESF_2pc_ND_', int2str(Voltage(1)),...
%                    'V.txt'), ...
%             strcat('~/Desktop/TESF_formatted_data/ND_formatted/TESF_2pc_ND_', int2str(Voltage(2)),...
%                    'V.txt'), ...
%             strcat('~/Desktop/TESF_formatted_data/ND_formatted/TESF_2pc_ND_0', int2str(Voltage(3)),...
%                    'V.txt')};

filename = {strcat('~/Desktop/TESF_formatted_data/PCBM_formatted/TESF_2pc_PCBM_', int2str(Voltage(1)),...
                   'V.txt'), ...
            strcat('~/Desktop/TESF_formatted_data/PCBM_formatted/TESF_2pc_PCBM_', int2str(Voltage(2)),...
                   'V.txt'), ...
            strcat('~/Desktop/TESF_formatted_data/PCBM_formatted/TESF_2pc_PCBM_0', int2str(Voltage(3)),...
                   'V.txt')};

% filename = {strcat('~/Desktop/TESF_formatted_data/TIPS_formatted/TESF_2pc_TIPS_s2_',...
%             int2str(Voltage(1)), 'V.txt'),...
%             strcat('~/Desktop/TESF_formatted_data/TIPS_formatted/TESF_2pc_TIPS_s2_',...
%                    int2str(Voltage(2)),'V.txt'), ...
%             strcat('~/Desktop/TESF_formatted_data/TIPS_formatted/TESF_2pc_TIPS_s2_',...
%                    int2str(Voltage(3)),'V.txt')};

Data = cell(length(Voltage),1);
for nn=1:length(Voltage)
    fileID = fopen(filename{nn}, 'r');
    Data{nn} = fscanf(fileID , '%g,_%g', [2 inf]);
    Data{nn} = Data{nn}';
    Data{nn}(:,1) = Data{nn}(:,1) * 10^-9;  %Convert ns times to s times
    Data{nn}(:,2) = Data{nn}(:,2) /dTh;
    fclose(fileID);
end
```

```
85  plotname = {strcat('TESF + 2% PCBM, ', int2str(Voltage(1)),' Volts'),...
86              strcat('TESF + 2% PCBM, ', int2str(Voltage(2)),' Volts'),...
87              strcat('TESF + 2% PCBM, ', int2str(Voltage(3)),' Volts')};
88
89  %Injection barriers
90  PphiB = 0.25 * 1.602e-19; %in J
91  NphiB = 2.05 * 1.602e-19; %in J
92
93  %Current Parameter being varied given by pNum
94  xBase=[0.0248069,0.359629,0.000381258,9.08365e-05,8.91805e-09,5.50412e-08,0.00404134,8.18692e-07,...
95         39.0573,8.68709e+19,3.82221e+18,0.0800081,0.000599941,0.584155,-0.00321471,0.48775,...
96         -0.00133112,1.76633e-09,5.94479e+08];
97  numVars = 19;
98
99  Nph = 1.5102e11*10^4 / dTh; %Number density of absorbed photons per pulse (m^-3)
100
101 a = ExParams(1); %Initial spatial separation of O-B excitons
102 kR = ExParams(2); %Recombination rate of O-B excitons
103
104 tFinal = 20e-9; %Total simulation time (s)
105 dt = 10^-13; %Time step for gaussian (s)
106
107
108 Rsq = cell(numVars,1);
109 Xlt = cell(numVars,1);
110 CTlt = cell(numVars,1);
111 kDUS = cell(numVars,1);
112 kDctUS = cell(numVars,1);
113
114 muNSt = cell(numVars,1);
115 muPSt = cell(numVars,1);
116 fSt = cell(numVars,1);
117 obSt = cell(numVars,1);
118 ctSt = cell(numVars,1);
119
```

```
for ll = 8:8
    vb = xBase(ll);
    vary = [vb*.1,vb*.5,vb,vb*2,vb*10];
    nIt = length(vary);
    legstr = '''Data1'',''Data2'',''Data3'',';
    plotstr = 'Data{1}(:,1),Data{1}(:,2),Data{2}(:,1),Data{2}(:,2),Data{3}(:,1),Data{3}(:,2),';
    %plotstr = '';
    plotstrNorm = '';

    switch(ll)
        case 1
            varStr = 'muN varied';
        case 2
            varStr = 'muP varied';
        case 3
            varStr = 'gN varied';
        case 4
            varStr = 'gP varied';
        case 5
            varStr = 'Bn varied';
        case 6
            varStr = 'Bp varied';
        case 7
            varStr = 'Bnpt varied';
        case 8
            varStr = 'Bntp varied';
        case 9
            varStr = 'Delta varied';
        case 10
            varStr = 'Nn varied';
        case 11
            varStr = 'Np varied';
        case 12
            varStr = 'f0 varied';
        case 13
```

```
155             varStr = 'gF varied';
156         case 14
157             varStr = 'ob0 varied';
158         case 15
159             varStr = 'gOB varied';
160         case 16
161             varStr = 'ct0 varied';
162         case 17
163             varStr = 'gCT varied';
164         case 18
165             varStr = 'aCT varied';
166         case 19
167             varStr = 'kRct varied';
168     end
169
170     Jstore = cell(nIt,1);
171     JstoreNorm = cell(nIt,1);
172     denStore = cell(nIt,1);
173
174     Rsq{ll} = zeros(nIt,length(Voltage));
175     Xlt{ll} = zeros(nIt,length(Voltage));
176     CTlt{ll} = zeros(nIt,length(Voltage));
177     kDUS{ll} = zeros(nIt,length(Voltage));
178     kDctUS{ll} = zeros(nIt,length(Voltage));
179
180     muNSt{ll} = zeros(nIt,length(Voltage));
181     muPSt{ll} = zeros(nIt,length(Voltage));
182     fSt{ll} = zeros(nIt,length(Voltage));
183     obSt{ll} = zeros(nIt,length(Voltage));
184     ctSt{ll} = zeros(nIt,length(Voltage));
185
186     val = zeros(length(vary),1); %Final Objective function value
187
188     FID = fopen('Results.txt','a');
189     fprintf(FID,'%s\n',varStr);
```

```
190     fclose(FID);
191     for nn = 1:nIt
192         switch mod(nn,7)
193             case 0
194                 plCol = 'r';
195             case 1
196                 plCol = 'g';
197             case 2
198                 plCol = 'b';
199             case 3
200                 plCol = 'c';
201             case 4
202                 plCol = 'm';
203             case 5
204                 plCol = 'y';
205             case 6
206                 plCol = 'k';
207         end
208         tic
209 
210         if(ll < 20)
211             x = xBase;
212             x(ll) = vary(nn);
213         end
214 
215         FID = fopen('Results.txt','a');
216         fprintf(FID,'Test Value = %10.5g\t',x(ll));
217         fclose(FID);
218 
219         for mm=1:length(Voltage)
220 
221             %Basic Parameter Assignment
222             muN0 = x(1)*10^-4; %Base electron mobility (m^2 / (Vs))
223             muP0 = x(2)*10^-4; %Base hole mobility ( m^2 / (Vs))
224             gN = x(3); %Electron Field Mobility Dependence ( (m/V)^.5 )
```

```
225 gP = x(4); %Hole Field Mobility Dependence ( (m/V)^.5 )
226 Bn = x(5)*10^-6; %Electron trapping constant (m^3 / s)
227 Bp = x(6)*10^-6; %Hole trapping constant (m^3/s)
228 Bnpt = x(7)*10^-6; %Electron+trapped hole recombination constant (m^3/s)
229 Bntp = x(8)*10^-6; %Hole+trapped electron recombination constant (m^3/s)
230 Delta = x(9) * 10^-3 * e; %Hole Trap Depth (J)
231 Nn = x(10)*10^6; %Density of electron traps (m^-3)
232 Np = x(11)*10^6; %Density of hole traps (m^-3)
233 f0 = x(12); %Percentage of hot excitons that become SSC states
234 gF = x(13); %Field dependence of f
235 ob0 = x(14); %Percent of absorbed carriers that become O-B excitons
236 gOB = x(15); %Field Dependence for ob
237 ct0 = x(16); %Percent of absorbed carriers that become CT excitons
238 gCT = x(17); %Field Dependence for ct
239 aCT = x(18); %Initial spatial separation of CT excitons
240 kRCT = x(19); %Recombination rate of CT excitons
241
242
243 V = Voltage(mm);
244 E = V / d;
245
246 muN = muN0 * exp(gN*sqrt(E));
247 muP = muP0 * exp(gP*sqrt(E));
248
249 f = f0+V*gF;
250 ob = ob0+V*gOB;
251 ct = ct0+V*gCT;
252
253 Bpt = Np*Bp*exp(-Delta/(kB*T));
254
255 dtData = abs(Data{mm}(1,1) - Data{mm}(2,1));
256 zeroPos = abs(Data{mm}(1,1) / dtData) + 1;
257 zeroPos = cast(zeroPos,'uint64');
258 JDark = Data{mm}(zeroPos,2);
259
```

```
260 %Scaling Block, see Theory pg 56 for details
261 N0 = JDark / (e*E*(muP + muN*exp((PphiB-NphiB)/(kB*T)))); % m^-3, the initial hole density
262 Diff = 1e-4; %m^2/s
263 Vkt = kB*T/e; % V
264 Ld = sqrt(e0*eR*kB*T/(e^2*N0)); % m
265 t0 = Ld^2 / Diff; % s
266 J0 = e*Diff*N0/Ld; % A/m^2
267
268 JDarkSc = JDark / J0;
269
270 dSc = d/Ld;
271 tFinalSc = tFinal / t0;
272 dtSc = dt / t0;
273
274 VSc = V / Vkt;
275 ESc = E * Ld / Vkt;
276
277 NphSc = Nph / N0;
278 muNSc = muN * Vkt / Diff;
279 muPSc = muP * Vkt / Diff;
280 BnSc = Bn * N0 * t0;
281 BpSc = Bp * N0 * t0;
282 BnptSc = Bnpt * N0 * t0;
283 BntpSc = Bntp * N0 * t0;
284 NnSc = Nn / N0;
285 NpSc = Np / N0;
286 BptSc = Bpt * t0;
287 %End Scaling Block
288
289 %Constructing Gaussian Beam Profile, 500ps pulse
290 %Final result is # of excitons created per sec
291 %Need to divide by dt for units and normalize total area of gaussian
292 tLit = 5e3; %tLit * dt = Full Width Half Max of Gaussian pulse
293 tGfinal = tFinal / dt;
294 FWHM = tLit * dt;
```

```
295 sig = FWHM / (2*sqrt(2*log(2)));
296 FWIM = 2*sqrt(2*log(10))*sig;
297 tGauss = 0:dt:(tGfinal*dt);
298 beamProfile = gaussmf(tGauss,[sig (FWIM / 2)]);
299 tGaussSc = tGauss/t0;
300 Gvec = NphSc*beamProfile/trapz(tGaussSc,beamProfile);
301
302 %Calc of dissociation rates
303 %Langevin recombination rate scaled for ODEs (scale: N0 * t0)
304 g = e*(muN+muP)/(e0*eR) * t0*N0;
305 %Langevin recombination rate scaled for kD calcs ( scale: 1/(Ld*Diff) )
306 gSc = e*(muN + muP)/(e0*eR) * (1/(Ld*Diff));
307
308 Eb = e^2 / (4*pi*e0*eR*a);  %Coulombic Exiton Binding Energy (J)
309 EbCT = e^2 / (4*pi*e0*eR*aCT);
310
311 b = e^3 * E / (8*pi*e0*eR*kB^2*T^2);
312 bessel = besselj(1,2*sqrt(-2*b));
313 bCT = e^3 * E / (8*pi*e0*eR*kB^2*T^2);
314 besselCT = besselj(1,2*sqrt(-2*b));
315
316 kDSc = real(gSc .* Ld^3 .* exp(-Eb/(kB*T)) .* bessel ./ (4*pi*a^3*sqrt(-2*b)));
317 kCTd = real(gSc .* Ld^3 .* exp(-EbCT/(kB*T)) .* besselCT ./ (4*pi*aCT^3*sqrt(-2*bCT)));
318
319 kRSc = kR*t0;
320 kCTr = kRCT*t0;
321
322 %Initial Conditions
323 %See Theory notebook pg 40-41 & 60 for explanation
324
325 n0 = JDarkSc / (ESc * (muNSc + muPSc*exp((NphiB-PphiB)/(kB*T))));
326 p0 = 1;
327 nt0 = BnSc*NnSc*n0 / (BnSc*n0 + BntpSc*p0);
328 pt0 = BpSc*NpSc*p0 / (BpSc*p0 + BnptSc*n0 + BptSc);
329 X0 = 0;
```

```
330         CT0 = 0;
331
332         Y0 = [n0; nt0; p0; pt0; X0; CT0];
333
334         options = odeset('Stats','off','NonNegative',[1 2 3 4 5 6]);
335         [t, Y] = ode15s(@(t, y)odes(t, y, tGaussSc, Gvec, g, BnSc, BpSc, BnptSc, BntpSc, BptSc,...
336                                     f, NnSc, NpSc, ob,kDSc,kRSc,ct,kCTd,kCTr),...
337                         [0 tFinalSc], Y0, options);
338
339         t = t *t0;
340         J = ESc*(muNSc*Y(:,1)+muPSc*Y(:,3)) * J0; %A/m^2
341         JNorm = J - min(J);
342         JNorm = JNorm / max(JNorm);
343
344         Jstore{nn,mm} = [t J];
345         JstoreNorm{nn,mm} = [t JNorm];
346         denStore{nn,mm} = [t Y*N0];
347         plotstr = strcat(plotstr, 'Jstore{', int2str(nn), ',', int2str(mm), '}(:,1),Jstore{',...
348                          int2str(nn), ',', int2str(mm), '}(:,2),''-', plCol, '''');
349         plotstrNorm = strcat(plotstrNorm, 'JstoreNorm{', int2str(nn), ',', int2str(mm),...
350                              '}(:,1),JstoreNorm{', int2str(nn), ',', int2str(mm),...
351                              '}(:,2),''-', plCol, '''');
352         legstr = strcat(legstr, '''', num2str(x(ll), '%.4e'), '''');
353         if (nn < nIt || mm < length(Voltage))
354            legstr = strcat(legstr,',');
355            plotstr = strcat(plotstr,',');
356            plotstrNorm = strcat(plotstrNorm,',');
357         else
358            legstr = strcat(legstr,');');
359            plotstr = strcat(plotstr,');');
360            plotstrNorm = strcat(plotstrNorm,');');
361         end
362
363         %Final calculation of objective function value
364         if(myRemRange(mm,1) < myObjRange(mm,1))
```

```
365             JComp = zeros(1,myObjRange(mm,2) - myObjRange(mm,1));
366             for jj = myObjRange(mm,1):myObjRange(mm,2)
367                 JComp(jj-myObjRange(mm,1)+1) = interp1(t,J,Data{mm}(jj,1));
368             end
369             DataComp = Data{mm}((myObjRange(mm,1)):(myObjRange(mm,2)),2)';
370
371             %val = val + sum( (JCompSc - DataCompSc).^2 );
372             SSerr = sum( ( JComp - DataComp ).^2 );
373             yBar = sum(DataComp)./length(DataComp);
374             SStot = sum( (DataComp - yBar).^2);
375             Rsq{ll}(nn,mm) = 1-(SSerr/SStot);
376
377         else
378             JComp = zeros(1, myObjRange(mm,2) - myObjRange(mm,1)...
379                             - (myRemRange(mm,2) - myRemRange(mm,1)));
380             for kk = myObjRange(mm,1):myRemRange(mm,1)
381                 JComp(kk-myObjRange(mm,1)+1) = interp1(t,J,Data{mm}(kk,1));
382             end
383             for jj = myRemRange(mm,2):myObjRange(mm,2)
384                 ind = myRemRange(mm, 1) - myObjRange(mm, 1) + 1 + jj - myRemRange(mm, 2) + 1;
385                 JComp(ind) = interp1(t,J,Data{mm}(jj,1));
386             end
387
388             DataComp = [Data{mm}(myObjRange(mm,1):myRemRange(mm,1),2)',...
389                         Data{mm}(myRemRange(mm,2):myObjRange(mm,2),2)'];
390
391
392             %val = val + sum( (JCompSc - DataCompSc).^2 );
393             SSerr = sum( ( JComp - DataComp ).^2 );
394             yBar = sum(DataComp)./length(DataComp);
395             SStot = sum( (DataComp - yBar).^2);
396             Rsq{ll}(nn,mm) = 1-(SSerr/SStot);
397         end
398         val(nn) = val(nn) + abs(1-Rsq{ll}(nn,mm));
399
```

```
400             kDUS{ll}(nn,mm) = kDSc/t0;
401             kDctUS{ll}(nn,mm) = kCTd/t0;
402             Xlt{ll}(nn,mm) = t0/(kDSc + kRSc);
403             CTlt{ll}(nn,mm) = t0/(kCTd + kCTr);
404         end
405         muNSt{ll}(nn,:) = muN0*exp(gN*sqrt(Voltage/d));
406         muPSt{ll}(nn,:) = muP0*exp(gP*sqrt(Voltage/d));
407         fSt{ll}(nn,:) = f0*Voltage.^gF;
408         obSt{ll}(nn,:) = ob0*Voltage.^gOB;
409         ctSt{ll}(nn,:) = ct0*Voltage.^gCT;
410 
411         FID = fopen('Results.txt','a');
412 %         writeString = strcat('Function Value = %g\n',...
413 %                              '%13.5g%13.5g%13.5g%13.5g\tVoltage\n',...
414 %                              '%13.5g%13.5g%13.5g%13.5g\tRsq\n',...
415 %                              '%13.5g%13.5g%13.5g%13.5g\tXlt\n',...
416 %                              '%13.5g%13.5g%13.5g%13.5g\tCTlt\n',...
417 %                              '%13.5g%13.5g%13.5g%13.5g\tkDUS\n',...
418 %                              '%13.5g%13.5g%13.5g%13.5g\tkDctUS\n',...
419 %                              '%13.5g%13.5g%13.5g%13.5g\tmuN\n',...
420 %                              '%13.5g%13.5g%13.5g%13.5g\tmuP\n',...
421 %                              '%13.5g%13.5g%13.5g%13.5g\tf\n',...
422 %                              '%13.5g%13.5g%13.5g%13.5g\tob\n',...
423 %                              '%13.5g%13.5g%13.5g%13.5g\tct\n\n');
424         writeString = strcat('Function Value = %g\n',...
425                              '%13.5g%13.5g%13.5g\tVoltage\n',...
426                              '%13.5g%13.5g%13.5g\tRsq\n',...
427                              '%13.5g%13.5g%13.5g\tXlt\n',...
428                              '%13.5g%13.5g%13.5g\tCTlt\n',...
429                              '%13.5g%13.5g%13.5g\tkDUS\n',...
430                              '%13.5g%13.5g%13.5g\tkDctUS\n',...
431                              '%13.5g%13.5g%13.5g\tmuN\n',...
432                              '%13.5g%13.5g%13.5g\tmuP\n',...
433                              '%13.5g%13.5g%13.5g\tf\n',...
434                              '%13.5g%13.5g%13.5g\tob\n',...
```

```
435                             '%13.5g%13.5g%13.5g\tct\n\n');
436         fprintf(FID, writeString, val(nn), Voltage, Rsq{ll}(nn, :), Xlt{ll}(nn, :), CTlt{ll}(nn, :),...
437                 kDUS{ll}(nn, :), kDctUS{ll}(nn, :), muNSt{ll}(nn, :), muPSt{ll}(nn, :),...
438                 fSt{ll}(nn, :), obSt{ll}(nn, :), ctSt{ll}(nn, :));
439         fclose(FID);
440         toc
441     end
442     figure;
443     eval(['plot(', plotstr]);
444     eval(['l = legend(' legstr]);
445     set(l,'fontsize',16);
446     xlim([-5e-10,5e-9]);
447     xlabel('Time (s)','fontsize',16);
448     ylabel('Current Density (A/m^3)','fontsize',16);
449     title(varStr,'fontsize',16);
450 
451     figure;
452     eval(['plot(', plotstrNorm]);
453     eval(['l = legend(' legstr]);
454     set(l,'fontsize',16);
455     xlim([-5e-10,1e-8]);
456     xlabel('Time (s)','fontsize',16);
457     ylabel('Current Density (A/m^3)','fontsize',16);
458     title(varStr,'fontsize',16);
459 
460 
461 end
```

Bibliography

[1] A. J. Heeger. "25th anniversary article: Bulk heterojunction solar cells: Understanding the mechanism of operation." *Advanced Materials*, 26:10, 2014. doi:10.1002/adma.201304373.

[2] R. Coehoorn & P. A. Bobbert. "Effects of Gaussian disorder on charge carrier transport and recombination in organic semiconductors." *Physica Status Solidi (a)*, 209:2354, 2012. doi:10.1002/pssa.201228387.

[3] C. Dimitrakopoulos & P. Malenfant. "Organic Thin Film Transistors for Large Area Electronics." *Advanced Materials*, 14:99, 2002. doi:10.1002/1521-4095(20020116)14:2⟨99::AID-ADMA99⟩3.0.CO;2-9.

[4] S. K. Park, D. A. Mourey, S. Subramanian, J. E. Anthony, & T. N. Jackson. "High-mobility spin-cast organic thin film transistors." *Applied Physics Letters*, 93:043301, 2008. doi:10.1063/1.2952769.

[5] D. Natali & M. Caironi. "Charge injection in solution-processed organic field-effect transistors: physics, models and characterization methods." *Advanced Materials*, 24:1357, 2012. doi:10.1002/adma.201104206.

[6] M. Lloyd, J. Anthony, & G. Malliaras. "Photovoltaics from soluble small molecules." *Materials Today*, 10:34, 2007.

[7] R. J. Kline, S. D. Hudson, X. Zhang, D. J. Gundlach, A. J. Moad, O. D. Jurchescu, T. N. Jackson, S. Subramanian, J. E. Anthony, M. F. Toney, & L. J. Richter. "Controlling the microstructure of solution-processable small molecules in thin-film transistors through substrate chemistry." *Chemistry of Materials*, 23:1194, 2011. doi: 10.1021/cm102834m.

[8] J. E. Anthony. "Small-molecule, nonfullerene acceptors for polymer bulk heterojunction organic photovoltaics." *Chemistry of Materials*, 23:583, 2011. doi:10.1021/cm1023019.

[9] A. J. Heeger. "Semiconducting polymers: the third generation." *Chemical Society Reviews*, 39:2354, 2010. doi:10.1039/b914956m.

[10] M. T. Lloyd, J. E. Anthony, & G. G. Malliaras. "Photovoltaics from soluble small molecules." *Materials Today*, 10:34, 2007. doi:10.1016/S1369-7021(07)70277-8.

[11] Y. Lin, Y. Li, & X. Zhan. "Small molecule semiconductors for high-efficiency organic photovoltaics." *Chemical Society Reviews*, 41:4245, 2012. doi:10.1039/c2cs15313k.

[12] W. Brütting. "Introduction to the physics of organic semiconductors." In "Physics of Organic Semiconductors," Wiley-VCH, 2005.

[13] A. D. Platt, J. Day, S. Subramanian, J. E. Anthony, & O. Ostroverkhova. "Optical, fluorescent, and (photo)conductive properties of high-performance functionalized pentacene and anthradithiophene derivatives." *Journal of Physical Chemistry C*, 113:14006, 2009. doi:10.1021/jp904021p.

[14] O. Jurchescu, D. Mourey, S. Subramanian, S. Parkin, B. Vogel, J. Anthony, T. Jackson, & D. Gundlach. "Effects of polymorphism on charge transport in organic semiconductors." *Physical Review B*, 80:085201, 2009. doi:10.1103/PhysRevB.80.085201.

[15] K. Paudel, B. Johnson, M. Thieme, M. M. Haley, M. M. Payne, J. E. Anthony, & O. Ostroverkhova. "Enhanced charge photogeneration promoted by crystallinity in small-molecule donor-acceptor bulk heterojunctions." *Applied Physics Letters*, 105:043301, 2014. doi:10.1063/1.4891758.

[16] B. Valeur. *Molecular Fluorescence: Principles and Applications*. Wiley-VCH, 2002.

[17] T. Itoh. "Fluorescence and phosphorescence from higher excited states of organic molecules." *Chemical reviews*, 112:4541, 2012. doi:10.1021/cr200166m.

[18] M. Kasha. "Characterization of electronic transitions in complex molecules." *Discussions of the Faraday Society*, 9:14, 1950. doi:10.1039/df9500900014.

[19] J. Lakowicz. *Principles of Fluorescence Spectroscopy, 3rd Edition*. Springer, 2006.

[20] V. I. Arkhipov & H. Bässler. "Exciton energy relaxation and dissociation in pristine and doped conjugated polymers." In W. Brütting, editor, "Physics of Organic Semiconductors," WILEY-VCH Verlag GmbH & Co. KGaA, 2005.

[21] B. Johnson, M. Kendrick, & O. Ostroverkhova. "Charge carrier dynamics in organic semiconductors and their donor-acceptor composites: Numerical modeling of time-resolved photocurrent." *Journal of Applied Physics*, 114:094508, 2013.

[22] R. Batt, C. Braun, & J. Hornig. "Electric-field and temperature dependence of photoconductivity." *Journal of Chemical Physics*, 49:1967, 1968. doi:10.1063/1.1670336.

[23] R. R. Chance. "Intrinsic photoconduction in anthracene single crystals: Electric field dependence of hole and electron quantum yields." *The Journal of Chemical Physics*, 59:2269, 1973. doi:10.1063/1.1680331.

[24] T. Clarke & J. Durrant. "Charge photogeneration in organic solar cells." *Chemical Reviews*, 110:6736, 2010. doi:10.1021/cr900271s.

[25] L. Onsager. "Initial recombination of ions." *Physical Review*, 54:554, 1938.

[26] C. Braun. "Electric field assisted dissociation of charge transfer states as a mechanism of photocarrier production." *Journal of Chemical Physics*, 80:4157, 1984.

[27] A. Lipnik. *Sov. Phys. Solid State*, 6:823, 1964.

[28] M. Fuoss & F. Accascina. *Electrolytic Conductance*. Interscience, 1959.

[29] L. Onsager. "Deviations from Ohm's Law in Weak Electrolytes." *The Journal of Chemical Physics*, 2:599, 1934. doi:10.1063/1.1749541.

[30] J. Noolandi & K. M. Hong. "Theory of photogeneration and fluorescence quenching." *The Journal of Chemical Physics*, 70:3230, 1979. doi:10.1063/1.437912.

[31] V. Arkhipov, E. Emelianova, & H. Bässler. "Hot exciton dissociation in a conjugated polymer." *Physical Review Letters*, 82:1321, 1999. doi:10.1103/PhysRevLett.82.1321.

[32] L. G. Kaake, J. J. Jasieniak, R. C. Bakus, G. C. Welch, D. Moses, G. C. Bazan, & A. J. Heeger. "Photoinduced charge generation in a molecular bulk heterojunction material." *Journal of the American Chemical Society*, 134:19828, 2012. doi:10.1021/ja308949m.

[33] M. Wojcik & M. Tachiya. "Accuracies of the empirical theories of the escape probability based on Eigen model and Braun model compared with the exact extension of Onsager theory." *Journal of Chemical Physics*, 130:104107, 2009. doi:10.1063/1.3082005.

[34] K. Falkowski, W. Stampor, P. Grygiel, & W. Tomaszewicz. "Sano-tachiya-noolandi-hong versus onsager modelling of charge photogeneration in organic solids." *Chemical Physics*, 392:122, 2012. doi:10.1016/j.chemphys.2011.10.032.

[35] S. D. Baranovskii, M. Wiemer, A. V. Nenashev, F. Jansson, & F. Gebhard. "Calculating the Efficiency of Exciton Dissociation at the Interface between a Conjugated Polymer and an Electron Acceptor." *The Journal of Physical Chemistry Letters*, 3:1214, 2012. doi:10.1021/jz300123k.

[36] M. Chandross, S. Mazumdar, S. Jeglinski, X. Wei, Z. V. Vardeny, E. W. Kwock, & T. M. Miller. "Excitons in poly(*para*-phenylenevinylene)." *Physical Review B*, 50:14702, 1994. doi:10.1103/PhysRevB.50.14702.

[37] S. Barth, H. Bässler, H. Rost, & H. H. Hörhold. "Extrinsic and intrinsic DC photoconductivity in a conjugated polymer." *Physical Review B*, 56:3844, 1997. doi:10.1103/PhysRevB.56.3844.

[38] V. Arkhipov, E. Emelianova, S. Barth, & H. Bässler. "Ultrafast on-chain dissociation of hot excitons in conjugated polymers." *Physical Review B*, 61:8207, 2000.

[39] G. Grancini, M. Maiuri, D. Fazzi, A. Petrozza, H.-J. Egelhaaf, D. Brida, G. Cerullo, & G. Lanzani. "Hot exciton dissociation in polymer solar cells." *Nature Materials*, 12:29, 2012. doi:10.1038/nmat3502.

[40] J. Day, S. Subramanian, J. E. Anthony, Z. Lu, R. J. Twieg, & O. Ostroverkhova. "Photoconductivity in organic thin films: From picoseconds to seconds after excitation." *Journal of Applied Physics*, 103:123715, 2008. doi:10.1063/1.2946453.

[41] C. J. Brabec, G. Zerza, G. Cerullo, S. De Silvestri, S. Luzzati, J. C. Hummelen, & S. Sariciftci. "Tracing photoinduced electron transfer process in conjugated polymer/-fullerene bulk heterojunctions in real time." *Chemical Physics Letters*, 340:232, 2001. doi:10.1016/S0009-2614(01)00431-6.

[42] D. G. Cooke, F. C. Krebs, & P. U. Jepsen. "Direct observation of sub-100 fs mobile charge generation in a polymer-fullerene film." *Physical Review Letters*, 108:056603, 2012. doi:10.1103/PhysRevLett.108.056603.

[43] S. H. Park, A. Roy, S. Beaupré, S. Cho, N. Coates, J. S. Moon, D. Moses, M. Leclerc, K. Lee, S. Beaupre, & A. J. Heeger. "Bulk heterojunction solar cells with internal quantum efficiency approaching 100%." *Nature Photonics*, 3:297, 2009. doi:10.1117/12.825836.

[44] A. Petersen, A. Ojala, T. Kirchartz, T. Wagner, F. Wrthner, & U. Rau. "Field-dependent exciton dissociation in organic heterojunction solar cells." *Physical Review B*, 85:245208, 2012. doi:10.1103/PhysRevB.85.245208.

[45] A. V. Nenashev, S. D. Baranovskii, M. Wiemer, F. Jansson, R. Österbacka, A. V. Dvurechenskii, & F. Gebhard. "Theory of exciton dissociation at the interface between a conjugated polymer and an electron acceptor." *Physical Review B*, 84:035210, 2011. doi:10.1103/PhysRevB.84.035210.

[46] C. Deibel, T. Strobel, & V. Dyakonov. "Origin of the Efficient Polaron-Pair Dissociation in Polymer-Fullerene Blends." *Physical Review Letters*, 103:1, 2009. doi: 10.1103/PhysRevLett.103.036402.

[47] S. M. Sze & K. K. Ng. *Physics of Semiconductor Devices, 3rd Edition.* Wiley, 2007.

[48] H. Sirringhaus, T. Sakanoue, & J.-F. Chang. "Charge-transport physics of high-mobility molecular semiconductors." *Physica Status Solidi (B)*, 249:1655, 2012. doi: 10.1002/pssb.201248143.

[49] J. Chelikowsky & M. Cohen. "Electronic structure of silicon." *Physical Review B*, 10:5095, 1974.

[50] V. Arkhipov & P. Heremans. "Weak-field carrier hopping in disordered organic semiconductors: the effects of deep traps and partly filled density-of-states distribution." *Journal of Physics: Condensed Matter*, 9899, 2002.

[51] R. Coehoorn, W. Pasveer, P. Bobbert, & M. Michels. "Charge-carrier concentration dependence of the hopping mobility in organic materials with Gaussian disorder." *Physical Review B*, 72:155206, 2005. doi:10.1103/PhysRevB.72.155206.

[52] J. Cottaar, L. Koster, R. Coehoorn, & P. Bobbert. "Scaling Theory for Percolative

Charge Transport in Disordered Molecular Semiconductors." *Physical Review Letters*, 107:136601, 2011. doi:10.1103/PhysRevLett.107.136601.

[53] A. Troisi. "Dynamic disorder in molecular semiconductors: charge transport in two dimensions." *Journal of Chemical Physics*, 134:034702, 2011. doi:10.1063/1.3524314.

[54] O. Ostroverkhova, D. Cooke, S. Shcherbyna, R. Egerton, F. Hegmann, R. Tykwinski, & J. Anthony. "Bandlike transport in pentacene and functionalized pentacene thin films revealed by subpicosecond transient photoconductivity measurements." *Physical Review B*, 71:035204, 2005. doi:10.1103/PhysRevB.71.035204.

[55] V. Podzorov, E. Menard, J. A. Rogers, & M. E. Gershenson. "Hall effect in the accumulation layers on the surface of organic semiconductors." *Physical Review Letters*, 95:226601, 2005. doi:10.1103/PhysRevLett.95.226601.

[56] M. E. Gershenson, V. Podzorov, & A. F. Morpurgo. "Colloquium: Electronic transport in single-crystal organic transistors." *Reviews of Modern Physics*, 78:973, 2006. doi: 10.1103/RevModPhys.78.973.

[57] Y. C. Cheng, R. J. Silbey, D. A. da Silva Filho, J. P. Calbert, J. Cornil, & J. L. Brédas. "Three-dimensional band structure and bandlike mobility in oligoacene single crystals: A theoretical investigation." *Journal of Chemical Physics*, 118:3764, 2003. doi:10.1063/1.1539090.

[58] H. A. v Laarhoven, C. F. J. Flipse, M. Koeberg, M. Bonn, E. Hendry, G. Orlandi, O. D. Jurchescu, T. T. M. Palstra, & A. Troisi. "On the mechanism of charge transport in pentacene." *Journal of Chemical Physics*, 129:044704, 2008. doi:10.1063/1.2955462.

[59] T. Sakanoue & H. Sirringhaus. "Band-like temperature dependence of mobility in a solution-processed organic semiconductor." *Nature materials*, 9:736, 2010. doi:10.1038/nmat2825.

[60] A. Troisi & G. Orlandi. "Charge-Transport Regime of Crystalline Organic Semiconductors: Diffusion Limited by Thermal Off-Diagonal Electronic Disorder." *Physical Review Letters*, 96:086601, 2006. doi:10.1103/PhysRevLett.96.086601.

[61] Y. Yao. "Spin-boson theory for charge photogeneration in organic molecules: Role of quantum coherence." *Physical Review B*, 91:1, 2015. doi:10.1103/PhysRevB.91.045421.

[62] S. Ciuchi & S. Fratini. "Electronic transport and quantum localization effects in organic semiconductors." *Physical Review B*, 86:245201, 2012. doi:10.1103/PhysRevB.86.245201.

[63] G. Nan, X. Yang, L. Wang, Z. Shuai, & Y. Zhao. "Nuclear tunneling effects of charge transport in rubrene, tetracene, and pentacene." *Physical Review B*, 79:115203, 2009. doi:10.1103/PhysRevB.79.115203.

[64] W. L. Kalb, S. Haas, C. Krellner, T. Mathis, & B. Batlogg. "Trap density of states in small-molecule organic semiconductors: A quantitative comparison of thin-film transistors with single crystals." *Physical Review B*, 81:1, 2010. doi:10.1103/PhysRevB.81.155315.

[65] S. Gorgolis, A. Giannopoulou, & P. Kounavis. "Charge carriers' trapping states in pentacene films studied by modulated photocurrent." *Journal of Applied Physics*, 113, 2013. doi:10.1063/1.4795807.

[66] A. Miller & E. Abrahams. "Impurity conduction at low concentrations." *Physical Review*, 120:745, 1960.

[67] R. Schmechel & H. von Seggern. "Electronic traps in organic transport layers." In "Physics of Organic Semiconductors," Wiley-VCH, 2005.

[68] O. D. Jurchescu, J. Baas, & T. T. M. Palstra. "Effect of impurities on the mobility of single crystal pentacene." *Applied Physics Letters*, 84:3061, 2004. doi:10.1063/1.1704874.

[69] M. J. Jaquith, J. E. Anthony, & J. A. Marohn. "Long-lived charge traps in functionalized pentacene and anthradithiophene studied by time-resolved electric force microscopy." *Journal of Materials Chemistry*, 19:6116, 2009. doi:10.1039/b902880c.

[70] G. Lakhwani, A. Rao, & R. H. Friend. "Bimolecular recombination in organic photovoltaics." *Annual Review of Physical Chemistry*, 65:557, 2014. doi:10.1146/annurev-physchem-040513-103615.

[71] P. Langevin. "Recombinaison et mobilites des ions dans les gaz." *Annales de chimie et de physique*, 28:433, 2013.

[72] M. Hilczer & M. Tachiya. "Unified Theory of Geminate and Bulk Electron Hole Recombination in Organic Solar Cells." *The Journal of Physical Chemistry C*, p. 6808, 2010.

[73] I. Hwang, C. R. McNeill, & N. C. Greenham. "Drift-diffusion modeling of photocurrent transients in bulk heterojunction solar cells." *Journal of Applied Physics*, 106:094506, 2009. doi:10.1063/1.3247547.

[74] L. Kulikovsky, D. Neher, E. Mecher, K. Meerholz, H.-H. Hörhold, & O. Ostroverkhova. "Photocurrent dynamics in a poly(phenylene vinylene)-based photorefractive composite." *Physical Review B*, 69:125216, 2004. doi:10.1103/PhysRevB.69.125216.

[75] O. Ostroverkhova & K. D. Singer. "Space-charge dynamics in photorefractive polymers." *Journal of Applied Physics*, 92:1727, 2002. doi:10.1063/1.1491279.

[76] C. Soci, D. Moses, Q.-H. Xu, & A. Heeger. "Charge-carrier relaxation dynamics in highly ordered poly(p-phenylene vinylene): Effects of carrier bimolecular recombination and trapping." *Physical Review B*, 72:245204, 2005. doi:10.1103/PhysRevB.72.245204.

[77] J. Day, A. D. Platt, S. Subramanian, J. E. Anthony, & O. Ostroverkhova. "Influence of organic semiconductor-metal interfaces on the photoresponse of functionalized anthradithiophene thin films." *Journal of Applied Physics*, 105:103703, 2009. doi:10.1063/1.3129693.

[78] J. D. Servaites, B. M. Savoie, J. B. Brink, T. J. Marks, & M. A. Ratner. "Modeling geminate pair dissociation in organic solar cells: high power conversion efficiencies achieved with moderate optical bandgaps." *Energy & Environmental Science*, 5:8343, 2012. doi:10.1039/c2ee21376a.

[79] M. J. Kendrick, A. Neunzert, M. M. Payne, B. Purushothaman, B. D. Rose, J. E. Anthony, M. M. Haley, & O. Ostroverkhova. "Formation of the donor-acceptor charge-transfer exciton and its contribution to charge photogeneration and recombination in small-molecule bulk heterojunctions." *Journal of Physical Chemistry C*, 116:18108, 2012. doi:10.1021/jp305913s.

[80] W. E. B. Shepherd, A. D. Platt, M. J. Kendrick, M. A. Loth, J. E. Anthony, & O. Ostroverkhova. "Energy transfer and exciplex formation and their impact on exciton and charge carrier dynamics in organic films." *Journal of Physical Chemistry Letters*, 2:362, 2011. doi:10.1021/jz101698q.

[81] A. Platt, M. Kendrick, M. Loth, J. Anthony, & O. Ostroverkhova. "Temperature dependence of exciton and charge carrier dynamics in organic thin films." *Physical Review B*, 84:235209, 2011. doi:10.1103/PhysRevB.84.235209.

[82] Y. Yao, W. Yang, & Y. Zhao. "Exciton dissociation in the presence of phonons: A reduced hierarchy equations of motion approach." *Journal of Chemical Physics*, 140, 2014. doi:10.1063/1.4867418.

[83] M. C. Heiber & A. Dhinojwala. "Dynamic monte carlo modeling of exciton dissociation in organic donor-acceptor solar cells." *Journal of Chemical Physics*, 137:014903, 2012. doi:10.1063/1.4731698.

[84] W. Tress, K. Leo, & M. Riede. "Optimum mobility, contact properties, and open-circuit voltage of organic solar cells: A drift-diffusion simulation study." *Physical Review B*, 85:155201, 2012. doi:10.1103/PhysRevB.85.155201.

[85] J. Kalinowski, W. Stampor, & P. G. Di Marco. "Electromodulation of fluorescence in a crystalline organic photoconductor (thionaphthenindole)." *Journal of Chemical Physics*, 96:4136, 1992. doi:10.1063/1.461869.

[86] D. Wehenkel, L. Koster, M. Wienk, & R. Janssen. "Influence of injected charge carriers

on photocurrents in polymer solar cells." *Physical Review B*, 85:1, 2012. doi:10.1103/PhysRevB.85.125203.

[87] G. Malliaras & J. Scott. "The roles of injection and mobility in organic light emitting diodes." *Journal of Applied Physics*, 83:1, 1998.

[88] S. Lacic & O. Inganas. "Modeling electrical transport in blend heterojunction organic solar cells." *Journal of Applied Physics*, 97:124901, 2005. doi:10.1063/1.1931038.

[89] M. A. Lampert. "Simplified theory of space-charge-limited currents in an insulator with traps." *Physical Review*, 103:1648, 1956.

[90] C. K. Renshaw, J. D. Zimmerman, B. E. Lassiter, & S. R. Forrest. "Photoconductivity in donor-acceptor heterojunction organic photovoltaics." *Physical Review B*, 86:085324, 2012. doi:10.1103/PhysRevB.86.085324.

[91] S. G. Johnson. The NLOPT non-linear optimization package, version 2.3, 2012, see `www.ab-initio.mit.edu/nlopt`.

[92] T. Runarsson & X. Yao. "Search biases in constrained evolutionary optimization." *IEEE Trans. Syst., Man, Cybern. C: Appl. Rev.*, 35:233, 2005.

[93] M. J. D. Powell. "A direct search optimization method that models the objective and constraint functions by linear interpolation." In S. Gomex & J.-P. Hennart, editors, "Advances in Optimization and Numerical Analysis," p. 51. Kluwer Academic, Dordrecht, 1994.

[94] O. D. Jurchescu, S. Subramanian, R. J. Kline, S. D. Hudson, J. E. Anthony, T. N. Jackson, & D. J. Gundlach. "Organic single-crystal field-effect transistors of a soluble anthradithiophene." *Chemistry of Materials*, 20:6733, 2008. doi:10.1021/cm8021165.

[95] O. Kwon, V. Coropceanu, N. E. Gruhn, J. C. Durivage, J. G. Laquindanum, H. E. Katz, J. Cornil, & J. L. Bredas. "Characterization of the molecular parameters determining charge transport in anthradithiophene." *Journal of Chemical Physics*, 120:8186, 2004. doi:10.1063/1.1689636.

[96] D. Scharfetter & H. Gummel. "Large-signal analysis of a silicon read diode oscillator." *IEEE Transactions on Electron Devices*, 16:64, 1969.

[97] A. De Mari. "An accurate numerical steady-state one-dimensional solution of the P-N junction." *Solid-State Electronics*, 11:33, 1968. doi:10.1016/0038-1101(68)90137-8.

[98] J. W. Ward, M. A. Loth, R. J. Kline, M. Coll, C. Ocal, J. E. Anthony, & O. D. Jurchescu. "Tailored interfaces for self-patterning organic thin-film transistors." *Journal of Materials Chemistry.*, 22:19047, 2012. doi:10.1039/c2jm33974a.

[99] D. J. Gundlach, J. E. Royer, S. K. Park, S. Subramanian, O. D. Jurchescu, B. H. Hamadani, A. J. Moad, R. J. Kline, L. C. Teague, O. Kirillov, C. A. Richter, J. G. Kushmerick, L. J. Richter, S. R. Parkin, T. N. Jackson, & J. E. Anthony. "Contact-induced crystallinity for high-performance soluble acene-based transistors and circuits." *Nature Materials*, 7:216, 2008. doi:10.1038/nmat2122.

[100] K. Paudel, B. Johnson, A. Neunzert, M. Thieme, B. Purushothaman, M. M. Payne, & J. E. Anthony. "Small-Molecule Bulk Heterojunctions: Distinguishing Between Effects

of Energy Offsets and Molecular Packing on Optoelectronic Properties." *The Journal of Physical Chemistry C*, 117:24752, 2013.

[101] J. Kniepert, M. Schubert, J. C. Blakesley, & D. Neher. "Photogeneration and recombination in P3HT/PCBM solar cells probed by time-delayed collection field experiments." *Journal of Physical Chemistry Letters*, 2:700, 2011. doi:10.1021/jz200155b.

[102] F. C. Jamieson, T. Agostinelli, H. Azimi, J. Nelson, & J. R. Durrant. "Field-independent charge photogeneration in PCPDTBT/PC_70BM solar cells." *Journal of Physical Chemistry Letters.*, 1:3306, 2010. doi:10.1021/jz1013517.

[103] P. Miranda, D. Moses, & A. Heeger. "Ultrafast photogeneration of charged polarons in conjugated polymers." *Physical Review B*, 64:081201, 2001. doi:10.1103/PhysRevB.64.081201.

[104] O. Ostroverkhova, D. G. Cooke, F. A. Hegmann, R. R. Tykwinski, S. R. Parkin, & J. E. Anthony. "Anisotropy of transient photoconductivity in functionalized pentacene single crystals." *Applied Physics Letters*, 89:192113, 2006. doi:10.1063/1.2387135.

[105] H. Liang, W. Cao, M. Du, Y. Kim, W. Herman, & C. Lee. "Ultrafast photoconductivity in bamh-ppv polymer thin-films." *Chemical Physics Letters*, 419:292, 2006. doi:10.1016/j.cplett.2005.11.071.

[106] D. Moses, C. Soci, X. Chi, & A. Ramirez. "Mechanism of carrier photogeneration and carrier transport in molecular crystal tetracene." *Physical Review Letters*, 97:067401, 2006. doi:10.1103/PhysRevLett.97.067401.

[107] J. Day, A. D. Platt, O. Ostroverkhova, S. Subramanian, & J. E. Anthony. "Organic semiconductor composites: Influence of additives on the transient photocurrent." *Applied Physics Letters*, 94:013306, 2009. doi:10.1063/1.3062850.

[108] J.-F. Glowe, M. Perrin, D. Beljonne, S. C. Hayes, F. Gardebien, & C. Silva. "Charge-transfer excitons in strongly coupled organic semiconductors." *Physical Review B*, 81:041201, 2010. doi:10.1103/PhysRevB.81.041201.

[109] O. Ostroverkhova. "Photophysical and photoconductive properties of novel organic semiconductors." In F. Cicoira & C. Santato, editors, "Organic Electronics: Emerging Concepts and Technologies," Wiley-VCH, 2013.

[110] A. Fix, P. Deal, C. Vonnegut, B. Rose, L. Zakharov, & M. M. Haley. "Indeno[2,1-c]fluorene: A New Electron-Accepting Scaffold for Organic Electronics." *Organic Letters*, 15:1362, 2013. doi:10.1021/ol400318z.

[111] X. Y. Zhu. "How to draw energy level diagrams in excitonic solar cells." *Journal of Physical Chemistry Letters*, 5:2283, 2014. doi:10.1021/jz5008438.

[112] S. Subramanian, K. P. Sung, S. R. Parkin, V. Podzorov, T. N. Jackson, & J. E. Anthony. "Chromophore fluorination enhances crystallization and stability of soluble anthradithiophene semiconductors." *Journal of the American Chemical Society*, 130:2706, 2008. doi:10.1021/ja073235k.

[113] Y. S. Chung, N. Shin, J. Kang, Y. Jo, V. M. Prabhu, S. K. Satija, R. J. Kline, D. M. DeLongchamp, M. F. Toney, M. A. Loth, B. Purushothaman, J. E. Anthony, & D. Y. Yoon. "Zone-refinement effect in small molecule-polymer blend semiconductors for

organic thin-film transistors." *Journal of the American Chemical Society*, 133:412, 2011. doi:10.1021/ja108772q.

[114] A. Sharenko, M. Kuik, M. F. Toney, & T.-Q. Nguyen. "Crystallization-Induced Phase Separation in Solution-Processed Small Molecule Bulk Heterojunction Organic Solar Cells." *Advanced Functional Materials*, 24:3543, 2014. doi:10.1002/adfm.201304100.

[115] B. Bernardo, D. Cheyns, B. Verreet, R. D. Schaller, B. P. Rand, & N. C. Giebink. "Delocalization and dielectric screening of charge transfer states in organic photovoltaic cells." *Nature Communications*, 5:3245, 2014. doi:10.1038/ncomms4245.

[116] N. Kobayashi, M. Sasaki, & K. Nomoto. "Stable peri-xanthenoxanthene thin-film transistors with efficient carrier injection." *Chemistry of Materials*, 21:552, 2009.

[117] L. Wang, G. Duan, Y. Ji, & H. Zhang. "Electronic and Charge Transport Properties of peri-Xanthenoxanthene: The Effects of Heteroatoms and Phenyl Substitutions." *The Journal of Physical Chemistry C*, 116:22679, 2012.

[118] N. Lv, M. Xie, W. Gu, H. Ruan, S. Qiu, C. Zhou, & Z. Cui. "Synthesis, Properties, and Structures of Functionalized peri-Xanthenoxanthene." *Organic Letters*, 15:2382, 2013. doi:10.1021/ol400790d.

[119] M. Shtein, H. F. Gossenberger, J. B. Benziger, & S. R. Forrest. "Material transport regimes and mechanisms for growth of molecular organic thin films using low-pressure organic vapor phase deposition." *Journal of Applied Physics*, 89:1470, 2001. doi: 10.1063/1.1332419.

[120] R. P. Steer. "Concerning correct and incorrect assignments of Soret (S2-S0) fluorescence in porphyrinoids: a short critical review." *Photochemical & Photobiological Sciences*, 13:1117, 2014.

[121] W. E. B. Shepherd, A. D. Platt, D. Hofer, O. Ostroverkhova, M. Loth, & J. E. Anthony. "Aggregate formation and its effect on (opto)electronic properties of guest-host organic semiconductors." *Applied Physics Letters*, 97:163303, 2010. doi:10.1063/1.3505493.